# Development of Ultrathin Niobium Nitride and Niobium Titanium Nitride Films for THz Hot-Electron Bolometers

**Inaugural-Dissertation**

zur

Erlangung des Doktorgrades

der Mathematisch-Naturwissenschaftlichen Fakultät

der Universität zu Köln

vorgelegt von

**Sven Holger Bedorf**

aus Köln

Köln 2005

# Abstract

The GREAT (German Receiver for Astronomy at Terahertz Frequencies) aboard of SOFIA (Stratospheric Observatory for Infrared Astronomy) requires superconducting hot-electron bolometer (HEB) as heterodyne mixers for 1.9 THz and 2.7 THz. Within this research work, ultrathin ($<$ 5 nm) niobium titanium nitride (NbTiN) and niobium nitride (NbN) films have been developed and successfully implemented in the mixers for GREAT.

The main focus of this work is the development of ultrathin NbN and NbTiN films. A reproducible and reliable deposition process for ultrathin NbN and NbTiN films for the use in phonon-cooled HEB devices was established. The ultrathin films were deposited on silicon (Si) substrates and on 2 µm $Si_3N_4$ membranes by DC reactive magnetron sputtering. A method for the precise control of the nitrogen partial pressure by monitoring the target voltage has been introduced to deposit high quality, ultrathin NbN (3-4 nm, $T_c$=8.5 K) and NbTiN (4-5 nm, $T_c$=8 K) films. Substrate heating of at least 600°C during the deposition is essential for the fabrication of ultrathin NbN and NbTiN films on Si substrates and $Si_3N_4$ membranes.

The fabrication process required for HEB devices to be used in a quasi-optical mixer was developed. The ultrathin film was patterned by electron beam lithography (EBL), resulting in bolometer devices that measure areas of about 0.4 µm $\times$ 4 µm.

The nature of the contact determines the interface transparency between the bolometer and the contact structure. Different cleaning processes have been performed and the influence on the contact resistance have been instigated. A better interface transparency gives less RF losses and could improve the HEB sensitivity and local oscillator (LO) requirement. A better control of the interface transparency also leads to a better reproducibility in values of the normal state resistance of the HEB devices.

Heterodyne measurements were performed at 0.8 THz and 1.6 THz. For the NbTiN HEB devices, the double sideband (DSB) receiver noise temperature at 0.8 THz was found to be 2500 K for at 1.2 GHz IF. The main problem with HEB mixers is the limitation in the IF bandwidth. The measured noise bandwidth was about 1.5 GHz. The DSB receiver noise temperature at 1.6 THz LO frequency measured at Chalmers University, Sweden, was found to be 1600 K at 1.5 GHz IF. This result shows that the noise of these

NbTiN HEB devices is comparable with the NbN HEB mixers fabricated at the Chalmers University.

For the NbN HEB devices the DSB receiver noise temperature $T_{rec}$ was 1344 K at 0.8 THz with an absorbed LO power of 55 nW, estimated using the isothermal method. This receiver noise temperature is higher than the state-of-the-art receiver noise temperature at this frequency. This is possibly due to the losses in the optics. It was not possible to determine the noise bandwidth of this device, because the noise temperature did not increase by the factor of two in the bandwidth of the isolator. But the noise bandwidth is estimated to be about than 1.8 GHz.

Although the true bandwidth of the NbTiN and NbN HEB devices could only be measured with an appropriate IF system, the combination of these results show that NbTiN is possibly inferior in bandwidth to NbN used for the HEB fabrication.

# Zusammenfassung

Für die beiden Frequenzkanäle (1.9 THz und 2.7 THz) des GREAT-Empfängers (German Receiver for Astronomy at Terahertz Frequencies) auf SOFIA (Stratospheric Observatory for Infrared Astronomy) werden supraleitende Hot-Electron-Bolometer (HEB) als Heterodynmischer benötigt. Im Rahmen dieser Arbeit wurden ultradünne ($<$ 5nm) Niob-Titan-Nitrid (NbTiN)- und Niob-Nitrid (NbN)- Filme entwickelt. Diese Filme wurden erfolgreich für die Fabrikation der GREAT-Mischer verwendet.

Der Schwerpunkt dieser Arbeit liegt auf der Entwicklung ultradünner NbN- und NbTiN-Filme. Es wurde ein verlässlicher und reproduzierbarer Fabrikationsprozess für ultradünne NbN- und NbTiN-Filme zur Verwendung in phononengekühlten HEB-Bauteilen entwickelt. Die ultradünnen Filme wurden durch reaktives Kathodenzerstäuben auf Silizium (Si)-Substraten und 2 μm dicken $Si_3N_4$-Membranen hergestellt. Zur genauen Kontrolle des Stickstoff ($N_2$)-Partialdruckes wurde die Kathodenspannung überwacht, um hochqualitative, ultradünne NbN- (3-4 nm, $T_c$=8.5 K) und NbTiN- (4-5 nm, $T_c$=8.0 K) Filme abzuscheiden. Das Aufheizen des Substrates auf 600°C während des Zerstäubungsvorgangs ist notwendig, um ultradünne NbN- und NbTiN-Filme auf Si-Substraten und auf $Si_3N_4$ Membranen herzustellen.

Weiterhin wurde ein Fabrikationsprozess zur Herstellung von HEB-Bauteilen, die für den Einbau in quasi-optische Mischer benutzt werden können, entwickelt. Die ultradünnen Filme wurden mittels Elektronenstrahllithographie (EBL) strukturiert, da die Bauteilgröße ungefähr 0.4 μm $\times$ 4 μm betrug.

Die Beschaffenheit des Kontaktes beeinflusst die Grenzflächentransparenz zwischen dem Bolometer und der Kontaktstruktur. Unterschiedliche Reinigungsprozesse wurden durchgeführt und deren Einfluss auf den Kontaktwiderstand untersucht. Eine bessere Grenzflächentransparenz führt zu weniger RF-Verlusten, könnte möglicherweise die HEB-Empfindlichkeit verbessern und den Lokaloszillator-(LO) Bedarf verringern. Eine bessere Kontrolle der Grenzflächentransparenz sorgt ebenfalls für eine bessere Reproduzierbarkeit in Bezug auf den normalleitenden Widerstand des HEBs.

Es wurden heterodyne Messungen bei 0.8 und 1.6 THz durchgeführt. Dabei wurde bei einer Lokaloszillatorfrequenz von 0.8 THz und einer Zwischenfrequenz von 1,2 GHz eine mini-

male Doppel-Seitenband (DSB)-Empfängerrauschtemperatur von 2500 K gemessen. Das Hauptproblem von HEB-Mischern ist die stark limitierte Zwischenfrequenzbandbreite. Die gemessene Rauschbandbreite betrug 1,5 GHz. Die Rauschtemperaturmessungen wurden in der Chalmers Universität in Schweden durchgeführt, die Rauschtemperatur betrug 1600 K bei einer Zwischenfrequenz von 1,5 GHz. Dieses Ergebnis zeigt, dass die NbTiN-HEB-Mischer eine vergleichbare Rauschtemperatur haben wie die NbN-HEB-Mischer, welche an der Chalmers Universität hergestellt werden.

Die NbN-HEB-Mischer zeigten eine DSB-Empfängerrauschtemperatur von 1344 K bei einer Lokaloszillatorfrequenz von 0.8 THz. Die absorbierte LO-Leistung wurde mit der isothermen Methode bestimmt und betrug 55 nW. Die gemessene Rauschtemperatur ist etwas höher als die eines HEB-Mischers nach dem heutigen Stand der Technik bei dieser Frequenz. Wahrscheinlich resultiert diese Differenz aus Verlusten in der Optik. Es war nicht möglich, die Rauschbandbreite dieses HEB-Mischers zu bestimmen, da die Rauschtemperatur nicht innerhalb der Isolatorbandbreite um den Faktor zwei anstieg. Eine Abschätzung der Rauschbandbreide ergibt etwa 1.8 GHz.

Obwohl die eigentliche Bandbreite der NbN- und NbTiN-HEB-Mischer nur mit einem geeigneten Zwischenfrequenzmesssystem bestimmt werden kann, kann man aus den Ergebnissen dieser Arbeit ableiten, dass NbTiN als HEB-Material, in Bezug auf die Bandbreite, weniger geeignet ist als NbN.

# Table of Contents

# Chapter 1

# Introduction

## 1.1 THz Astronomy

Submillimeter wave astronomy provides information to study star formation, the interstellar medium, active galaxies, the sun and the planets and the spectrum of the microwave background radiation. A part of the submillimeter wave range is called THz frequency range. Strictly speaking the THz range covers the frequency range from 1 to 3 THz (100-300 µm wavelength), and in a broadest sense the frequency range from 0.5 to 6 THz (50-600 µm wavelength).

The basic problem of the THz astronomy is the poor transmission of the earth's atmosphere. The earth's atmosphere is largely not transparent for radiation between 30 and 300 µm wavelength. This absorption is mostly due to water vapor in the troposphere and other molecules in the atmosphere like Ozone and Oxygen. The formation of water vapor takes place in the troposphere and decreases abruptly in the stratosphere. This restricts ground based THz observations to some narrow atmospheric windows which can be observed at some distinct high altitude places at very good weather conditions (like Mauna Kea, Hawaii 4200 m or the Atacama desert, Chile about 5000 m).

Examples for ground based THz astronomy facilities are:

- the NANTEN2 Observatory, located in the Atacama desert (Chile), which is a collaboration between research institutes in Japan (Nagoya and Osaka University), South Korea (Seoul National University), and Germany (KOSMA, Radio Astronomisches Institut Universität Bonn). The NANTEN2 Observatory is equipped with a 4 m telescope and a receiver for

115, 230 and 345 GHz from the Nagoya University and the Sub-Mm Array Receiver for Two frequencies (SMART) for the frequency range of 460-880 GHz provided by KOSMA.

- the Atacama Pathfinder Experiment (APEX) which is a 12m telescope currently established at Llano de Chajnantor in Chile's Atacama desert.

- the KOSMA 3m submillimeter telescope on the Gornergrat near Zermatt (Swiss) which is operated by the I. Physikalisches Institut, Universität zu Köln and the Radioastronomisches Institut, University of Bonn.

- SMTO (Submillimeter Telescope Observatory) on Mt. Graham in Arizona equipped with a 10 m telescope.

- CSO (Caltech Submillimeter Observatory) on Mauna Kea, Hawaii with a 10 m diameter telescope.

- AST/RO (Antarctic Submillimeter Telescope and Remote Observatory) at the South Pole equipped with a 1.7 m telescope

The height of the troposphere is about 10-17 km depending on the season and the geographical position. The use of submillimeter telescopes on board of airplanes or balloons makes it possible to perform THz observations at a height of about 15 km. At the height of 14 km almost 85 % of the THz frequency range can be observed [1]. The rotational and vibrational transitions of gas molecules in the stratosphere still block parts of the THz radiation in a height of 15 km.

The first airborne observation was performed on board of a Lear-Jet by using a 30 cm telescope dish in 1969. The KAO (Kuiper Airborne Observatory) was a military airplane equipped with a 91 cm telescope operating from 1974-1996. Currently, SOFIA (Stratospheric Observatory for Infrared Astronomy) is being developed. SOFIA is a Boing 747SP equipped with a 2.7 m telescope and will be more sensitive than the KAO due to its larger telescope and modern sensitive detectors. The first flight of SOFIA will be in 2006. The development of the detector, which is described in this thesis, was done to provide a mixer for the instrument GREAT (German Receiver for Astronomy at Terahertz Frequencies) onboard of SOFIA.

GREAT is a modular dual-channel heterodyne instrument for high-resolution spectroscopy a joint project with the Max-Planck-Institut für Radioastronomie (MPifR) and the DLR-Institut für Weltraumsensorik & Planetenerkundung (DLR Berlin). KOSMA provided the superconducting mixer element for the low frequency band 1.6-1.9 THz (158-187 µm). The frequency range of 1.6-1.9 THz covers, beside other molecular lines, the important atomic transition line of ionized carbon (CII) which is an important cooling line of the interstellar medium (ISM). GREAT has also a mid-frequency band at 2.6 THz to observe the deuterated hydrogen molecule (HD), for which KOSMA provides the mixer element as well, and the high-frequency channel at 4.7 THz provided by DLR Berlin.

It is only possible to perform THz observations without the negative impact of the earth's atmosphere by using satellite based telescopes. Examples for space telescopes are the 57 cm telescope on IRAS (Infrared Astronomical Satellite) operated for almost one year in 1983, the ISO (Infrared Space Observatory) which was operational between 1995 and 1998, and the SWAS (Submillimeter Wave Astronomy Satellite) operating in 1999. Currently, the Herschel Space Observatory is under development.

## 1.2   Detector Technology

Beside the poor transmission of the earth's atmosphere for THz radiation, the detector technology for THz is a great challenge. In the THz frequency range, the detector technology of the Infrared radiation (IR) and the standard radio frequency range can not be used. The use of bolometers as heterodyne mixers is a possible solution.

Detectors for the THz frequency range can be divided into direct detectors and heterodyne detectors. The difference between the two categories are discussed in section 2.4. The detector developed in this thesis is a hot-electron bolometer (HEB) which is used as a mixing element in a heterodyne receiver. A heterodyne detector provides both the phase and the intensity of the incoming radiation. Using a direct detector, the spectral information has to be obtained by using a filter in front of the detector and it does not provide phase information. In a heterodyne receiver the signal is mixed with a local oscillator (LO) and down-converted to an inter-

mediate frequency (IF) at a few GHz. In the GHz frequency range conventional low noise amplifiers and filters are available. From the IF signal it is possible to characterize the signal radiation with very high spectral resolution.

A non-linearity in the current voltage (I-V) characteristics of the mixing element is used to down-convert the signal to the IF frequency. Different devices can be used to serve as a mixer.

Schottky-diodes have been the only available technology for the detection of THz radiation for a long time. They do not require cooling to cryogenic temperatures and cover a wide frequency range up to several THz. The main disadvantages are the poor sensitivity and the high LO power requirement. The LO is still a critical element for heterodyne detection in the THz frequency range. Solid state sources often do not provide enough power for the heterodyne operation in the THz range but are under development right now. The only strong THz sources are far infrared (FIR) lasers, which are very bulky and are not tunable in frequency. Recently, a new kind of THz source was developed based on a quantum cascade laser (QCL). QCLs are very powerful and very compact.

Superconductor-insulator-superconductor (SIS) tunnel junctions are extremely sensitive heterodyne mixers and have been widely used for frequencies below 1 THz. The upper frequency limit of these devices is determined by the gap frequency of the superconductor defined by $f_{gap} = \Delta/h$ with $\Delta$ the superconducting gap energy and $h$ the Planck's constant. Drastic losses above the gap frequency of the superconductor (about 700 GHz for niobium) occur inside the superconducting tuning circuit which is used to match the impedance of the SIS device to the antenna impedance. Using superconductors (like NbN or NbTiN) having a higher gap frequency than Nb has increased the upper frequency limit of SIS mixers to about 1.2 THz. The main advantage of SIS mixers is the wide IF bandwidth provided by this type of mixer.

HEB mixers do not have an upper frequency limit and provide a very high sensitivity ($T_{rec} < 2000$ K) and require very low LO power ($< 1$ μW). Although the IF bandwidth of HEB mixers is rather limited compared to Schottky and SIS mixers, HEB mixers are the most competitive devices for heterodyne detection in the THz range.

# 1.3 Thesis Overview

The aim of the research presented in this thesis was to develop phonon-cooled HEB mixers for THz frequencies. At the beginning of this research the bolometer development at KOSMA was focused on diffusion cooled HEBs. In diffusion cooled HEBs the energy of the electron subsystem is removed by out-diffusion of hot electrons into the normal conducting pads. This kind of HEB devices was preferred due to predicted large IF bandwidth of up to 8 GHz. But it turned out that the diffusion cooled HEBs are much more sensitive to changes in the bias conditions compared to phonon-cooled HEBs. This makes diffusion cooled HEBs unsuitable for the operation at a telescope.

In the phonon-cooled HEB devices the hot electrons loose their energy to the lattice and then to the substrate. For this type of HEBs ultrathin films from a material with a short electron-phonon interaction time are necessary. Candidates for the superconductor are ultrathin niobium nitride (NbN) and niobium titanium nitride (NbTiN) films. State-of-the-art phonon-cooled HEBs were fabricated from ultrathin NbN films within this work. At the beginning of this work the use of NbTiN as superconductor for HEBs indicated a substantial improvement of the noise and gain characteristics.

To achieve the maximum possible IF bandwidth, the superconducting films have to be as thin as possible while still having a high critical temperature. This work started with the development of ultrathin ($<$ 5 nm) NbTiN films. Based on these films, phonon-cooled HEB devices have been fabricated and heterodyne measurements were performed. One of the NbTiN HEBs is now integrated into the GREAT receiver in flight configuration. Concerning the sensitivity NbTiN HEBs are comparable to NbN HEBs, but the NbTiN HEB devices showed a lower IF bandwidth.

Almost all groups working on phonon-cooled NbN HEBs are using NbN films fabricated by the Moscow Pedagogical State University. In this research work ultrathin (3-4 nm) NbN films have been developed as an alternate source for NbN HEBs. Based on the NbN films, phonon-cooled HEB devices have been fabricated and heterodyne measurements have been performed. The main focus of this work has been on developing a reproducible and reliable deposition process for ultrathin NbN and NbTiN films for the HEB fabrication. These films are the fundamental requirement for phonon-cooled HEB devices fabricated for the GREAT receiver.

Beside the ultrathin film development, the device fabrication and the experimental studies of HEB devices for quasi-optical mixers were performed and described for NbN and NbTiN in this theses. The quality of the interface between the bolometer microbridge and the contact pads are responsible for RF and IF losses inside the device and improve the HEB sensitivity [2]. Therefore, special emphasis is placed on the process which determines the nature of the contacts. A fabrication process is developed to produce a optimal interface transparency.

This thesis closes with a summary and a conclusion of the ultrathin film deposition, the HEB fabrication and the measurement results of the fabricated HEB devices.

# Chapter 2

# Principle of Hot-Electron Bolometer Operation

## 2.1 Introduction

A bolometer (from Greek, *bole*: beam, radiation; *metreo*: measure) is a radiant-heat detector invented by Samuel P. Langley in 1881 [3]. This instrument measures small changes in temperature based on the fact that the electrical resistance of a metal changes with the amount of incident radiation. Langleys bolometer was a fine platinum wire detector. Langleys main scientific interest was the use of this detector to study the solar irradiance far into its infrared region [3]. As the temperature of the bolometer changes with the energy due to incident radiation this kind of detector is called a thermal detector.

The first useful for application bolometer was a bolometer made of carbon, which was invented 1959 by Boyle [4]. Modern bolometers are made of semiconductors or superconductors to increase the sensitivity of the detector.

Theoretically, bolometers can be used to detect radiation of any wavelength, because they are sensitive to any form of energy. For most frequency ranges they are not used in practice because there are better, more sensitive methods of detection.

For the millimeter-wave and infrared, bolometers are sensitive thermal detectors used for astronomical observations and laboratory spectroscopy [5]. Bolometers are also used in high-energy physics as particle detector.

For the use as an astronomical detector, the bolometer is used

in a cryogenic environment to obtain the highest sensitivity.

## 2.2  Basics of Bolometers

The thermal model of a bolometer is shown in Figure 2.1. A bolometer typically consists of an absorbing element having a heat capacity $C$ which converts the incident electromagnetic radiation to heat. The absorbing element is attached to a reservoir at temperature $T_0$ through a small thermal conductance $G$.

If the absorber and the thermometer are separate, the bolometer is called a *composite design*.

If the absorbing element is a heat dependent resistor, high sensitivity can be achieved if a superconductor is used. The change in the electrical resistance with temperature is very rapid near the critical temperature of the superconductor. This property makes superconducting films a good choice for a sensitive bolometer. The superconducting film is thermally coupled to a cold reservoir. The absorption of radiation causes a change of resistance. When biased with a constant current, a voltage change proportional to the radiation input power can be measured.

$P$ is the absorbed power which causes an increase of the device temperature until a balance is reached between the absorbed power and the loss to the cold-reservoir. The ratio

$$\tau = \frac{C}{G} \tag{2.1}$$

is called the bolometer *time constant*. It is the time it takes for the temperature to rise to the steady state value. It indicates the time the bolometer needs to respond to a change in the absorbed power. Later on we will see that the time constant $\tau$ of the bolometer determines the maximum intermediate frequency (IF), if the bolometer is used as a heterodyne mixer.

If the radiation is removed, the temperature of the device relaxes to the temperature of the cold-reservoir with the same time constant.

A quality factor of a bolometer is the voltage responsivity $S$. When the incident power $P$ changes by an amount $\Delta P$, the temperature $T$ changes by $\Delta T$, which results in a rise in electrical resistance $\Delta R$. This rise corresponds to a change in voltage across the bolometer resistance, if the bolometer is current biased ($I_{bias}$).
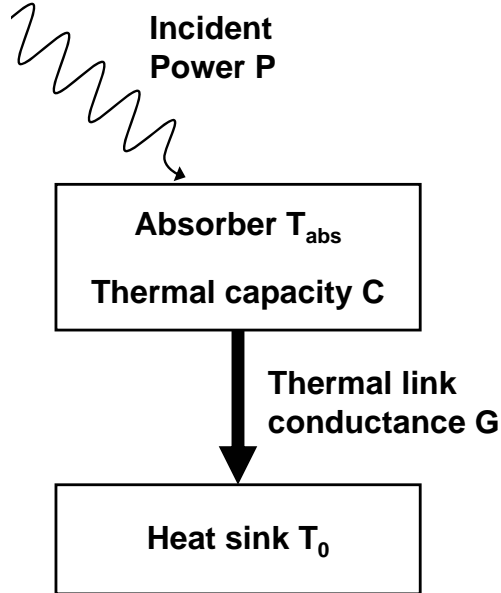
**Figure 2.1:** Thermal model of the basic bolometer operation

The bolometer temperature as a function of time is the solution of the classical heat transfer equation [5]:

$$C\frac{dT}{dt} = P(t) - G(T - T_0) \qquad (2.2)$$

Assuming the absorbed power is changing periodically in time, $P(T) = P_0 + \Delta P cos(\omega t)$, the amplitude $\Delta T$ of the corresponding temperature modulation is

$$\Delta T = \frac{\Delta P}{G\sqrt{1 + \omega^2\tau^2}} \qquad (2.3)$$

The voltage *responsivity S* is defined as the change in voltage across the bolometer resistance per Watt of absorbed signal power. It indicates how efficient a power change is converted into an electrical signal.

$$S = \frac{\Delta V}{\Delta P} \qquad (2.4)$$

using $\Delta V = I_{bias}\Delta R$ and $\Delta P$ given in Equation (2.3) gives

9

$$S = I_{\text{bias}} \frac{\Delta R}{\Delta T} \frac{1}{G \sqrt{1 + \omega^2 \tau^2}} \tag{2.5}$$

It is desired to operate a bolometer in a mode which provides a high responsivity and a short thermal time constant. At frequencies $\omega$ which are small compared to the time constant ($\omega\tau \ll 1$), the responsivity $S$ will be determined by thermal conductance $S \propto \frac{1}{G}$.

At frequencies $\omega$ which are higher, so that $\omega\tau \gg 1$, the responsivity $S$ will be proportional to $S \propto \frac{1}{C\omega}$.

From Equation (2.1) and Equation (2.5) it follows that increasing $G$ to get a small $\tau$ automatically leads to a smaller responsivity $S$.

Superconductors demonstrate a very strong dependence of resistivity with temperature in the transition region between the superconducting and the normal conducting state. This makes superconductors a good material for bolometers.

The resistance of a superconducting film as a function of temperature is shown in figure 2.2. At temperatures higher than the critical temperature $T_c$, the bolometer is normal conducting, this is the normal state region of the bolometer. Over a narrow temperature range $\Delta T_c$ just around $T_c$, the resistance value decreases rapidly, but not infinitely rapidly. This is the resistive state of the bolometer. In this temperature region the bolometer shows normal and superconducting zones simultaneously. For temperatures far below $T_c$ the whole bolometer becomes superconducting and the resistance value remains zero.

In order to achieve the highest sensitivity of the bolometer the device is cooled to the superconducting state and is then electrically biased into the transition region between the normal and superconducting states, the resistive state, where the superconductor will gradually become normal (see Figure 2.2). By biasing a bolometer around this steep transition, extremely sensitive, low-noise heterodyne mixers and direct detectors can be achieved.

Figure 2.2 also shows the current voltage (I-V) characteristics of a HEB at a bath temperature of 4.2 K. For low voltages the HEB is superconducting. The current increases until it reaches a maximum value ($I_c$). Then the current decreases for increasing voltage values and a region with a negative differential resistance exists. This is the resistive state. For higher voltages the HEB becomes normal conducting. This is the normal state region.

Because the bolometer operates at the transition temperature of the superconducting material, these bolometers are called
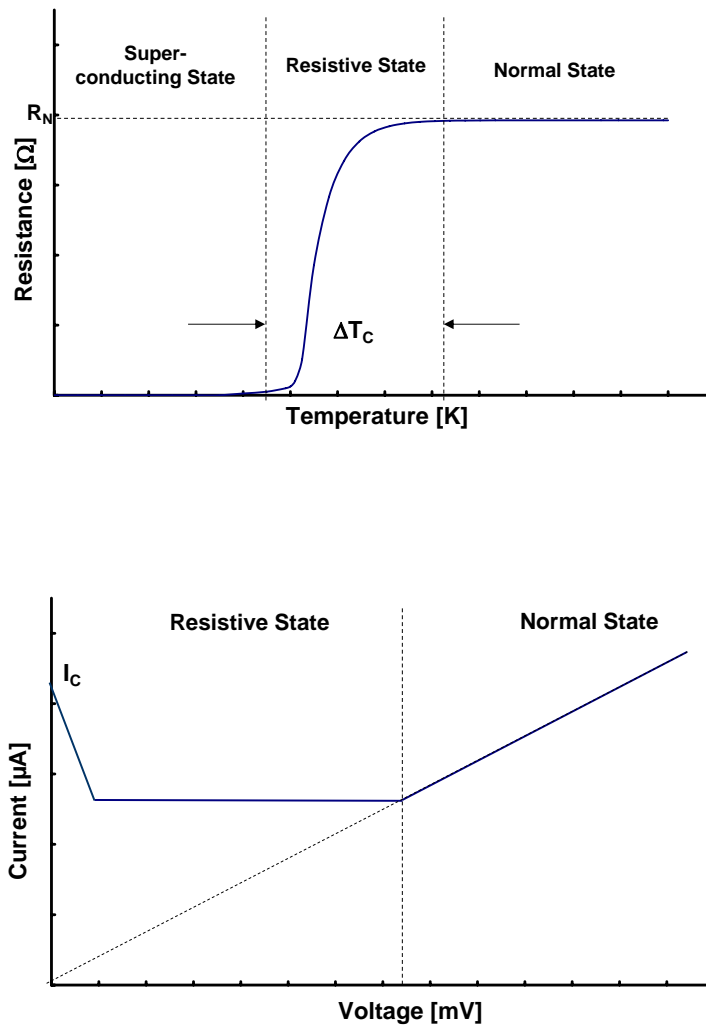
**Figure 2.2:** Ideal resistance versus temperature (R-T) and ideal current versus voltage (I-V) diagram of a supercon-ducting bolometer

11

transition-edge detectors if they are used for direct detection.

# 2.3 Hot-Electron Bolometers

The energy of submillimeter- and millimeter radiation is very small ($< 1$ meV). An approach for a bolometer operating in this frequency range is: The hot-electron bolometer (HEB).

The hot-electron phenomenon has become very helpful to understand many phenomena in modern semiconductors and super-conductors.

The term *hot-electron* specifies a non-equilibrium ensemble of high-energy electrons. Usually an external energy is applied to a system of carriers (e.g. by external radiation) having a higher input power than the rate of energy loss by the system to the lattice. So the electrons heat-up and the velocity distribution differs from the equilibrium Maxwell form [6]. In other words, the term *hot-electrons* describes electrons which are not in thermal equilibrium with the lattice.

In metals the heating of electrons does not change the electron mobility and therefore it does not affect the resistance value [7]. The hot electron approach is very productive for semiconductors, where the mobility of electrons depends on their effective temperature [8].

In superconductors the non-equilibrium electron heating process can be described in the following way:

The process of the hot electron phenomenon is illustrated in figure 2.3. An incident photon is absorbed by a Cooper pair. Due to the large coherence length[1] only one of the electrons of the Cooper pair absorbs the photon. The Cooper pair breaks apart and one highly excited electron with energy close to the incident photon energy and one low-energy quasiparticle are created. Next the quasiparticle loses its energy via electron-electron scattering and creates a secondary excited electron.

The above process continues until the electron-phonon interaction process takes place. This happens when the electron subsystem emits Debye phonons. This electron-phonon interaction excites additional electrons and breaks other Cooper pairs. The quasiparticles and the phonons can be described by thermal, normal-state distribution functions, where the electron and phonon effective temperatures ($T_e$ and $T_p$) are established instantly and uni-

---

[1]coherence length: the physical size of a cooper pair - representing the shortest distance over which superconductivity can be established in a material.
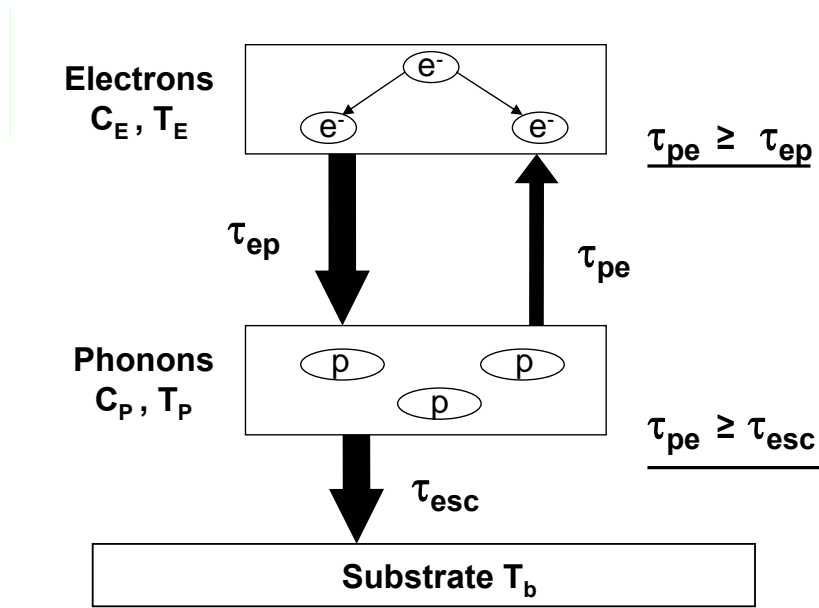
**Figure 2.3:** Thermalization scheme showing the hot electron phenomenon [9], where $T_e$ is the electron effective temperature, $T_p$ is the phonon effective temperature, $\tau_{ep}$ is the electron energy relaxation time via electron-phonon interaction, $\tau_{esc}$ is the time of the phonons to escape into the substrate, $C_e$ and $C_p$ are the electron and phonon specific heats and $T_b$ is the ambient substrate temperature.

formly throughout the whole system.

## 2.4  Coherent and Incoherent Detectors

There are two different techniques to detect the power of submillimeter and far-infrared wavelengths. One way is to detect the radiation directly or after shifting the incoming radiation to a lower frequency band and then amplify and detect the power of the radiation. The first method is a direct detection which is also called an incoherent detection. It creates charged carriers or converts the incoming energy to heat proportional to the flux of the incoming photons.

The method of shifting the incoming radiation to a lower frequency is called heterodyne principle or coherent detection. The

detector determines the phase and the intensity of the incoming radiation. The principle of a heterodyne receiver is described in section 2.5.

Bolometers can be used as coherent or incoherent detectors, but are more commonly used for direct detectors. Coherent detection is the best choice for high resolution spectroscopy. Heterodyne receivers provide a very high resolution ($R = 10^4$ - $10^7$), while direct detection instruments provide a lower resolution ($R < 10^4$). The spectral information is very important for astronomical observations and the high spectral resolution is necessary for resolving spectral lines of galactic objects [10].

In a coherent receiver the phase information is preserved, therefore the incoming wavefront detected by different heterodyne receivers can be reconstructed. This makes interferometry between distant heterodyne receivers possible.

The disadvantage of a bolometer used as a coherent detector is the narrow spectral bandwidth of a few GHz, which can be much higher for incoherent detectors. The setup of heterodyne receivers is much more complex, therefore large array detectors (a few 100 pixels) are almost not possible. Coherent detectors have a fundamental noise limit as shown below, while incoherent detectors do not have a fundamental noise limit.

The preserved phase information of a coherent detector provides a fundamental limit of its sensitivity. This can be explained by using the Heisenberg uncertainty relation $\Delta E \Delta t \geqslant h/2\pi$ in a semi-classical way. For $n$ photons with the phase $\phi$, the uncertainty relation is

$$\Delta n \Delta \phi \geqslant \frac{1}{2} \tag{2.6}$$

$\Delta \phi \leqslant 1/2$ is necessary for a phase coherence, therefore $\Delta n$ must be at least 1 to satisfy the uncertainty relation. This introduces a limitation of the sensitivity in a coherent receiver which is known as the *quantum limit*. The minimum output noise power of a coherent receiver is $h\nu$ per unit bandwidth or as an equivalent noise temperature $T_{quantum} = h\nu/k$ [11].

Direct detectors do not have a fundamental limit of the sensitivity. A direct detector does not produce any noise power unless photons are absorbed [10].

15

## 2.5 Heterodyne Receivers

In a heterodyne receiver a locally generated frequency is *mixed* with a signal frequency to produce a signal at a much lower frequency. This frequency conversion is done by a mixer element. The locally generated frequency and the signal frequency are added together to produce a beat frequency, the difference between the signal and the locally generated frequency.

A block diagram of a heterodyne detection system is illustrated in Figure 2.4. The local oscillator at a frequency $\omega_{LO}$ and a weaker signal at frequency $\omega_S$ are mixed to give an output of the intermediate frequency (IF) $\omega_{IF} =\mid \omega_S - \omega_{LO} \mid$.
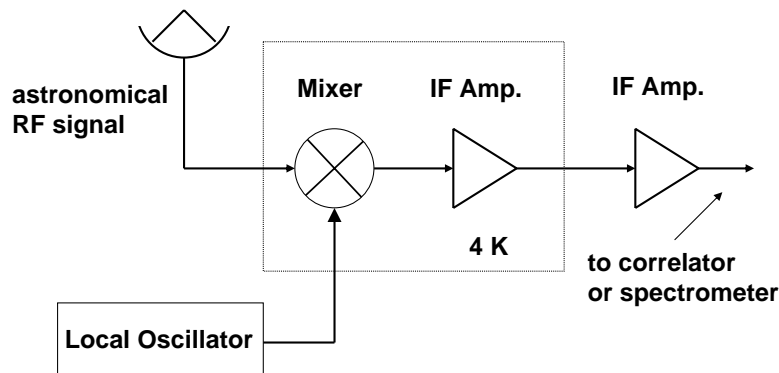


**Figure 2.4:** Blockdiagram of a heterodyne receiver

A non-linear element must be used to mix the two signals. To illustrate how this conversion is generated the simple case of a square law detector is considered. The square law detector is a nonlinear device because the I-V dependence has an exponential form which can approximated locally to a square law:

$$I(t) \sim V^2(t) \text{ when } V \geqslant 0 \qquad (2.7)$$

where $I(t)$ is the current, $V(t)$ is the voltage.

Applying an input voltage, consisting of a weak signal voltage $V_s \cos(\omega_S t)$ and a strong local oscillator voltage $V_{LO} \cos(\omega_{LO} t)$ to

16

the square law detector leads to:

$$
\begin{aligned}
I(t) \ &= \ \left[ V_S \cos(\omega_S t) + V_{LO} \cos(\omega_{LO} t) \right]^2 \\
&= \ \frac{1}{2} \left[ V_{LO}^2 + V_S^2 + V_S^2 \cos(2\omega_s t) + V_{LO}^2 \cos(2\omega_{LO} t) \right. \\
&\quad \left. + V_{LO} V_S \cos(\omega_S - \omega_{LO})t + V_{LO} V_S \cos(\omega_S + \omega_{LO})t \right] \quad (2.8)
\end{aligned}
$$

The diode current $I(t)$ consists of two frequency independent terms, terms at higher frequencies $2\omega_S$, $2\omega_{LO}$ $\omega_s + \omega_{LO}$ and one term at $\omega_S - \omega_{LO}$ which is the intermediate frequency (IF).

Since the cosines-function is symmetrical, it is not possible to determine if $\omega_S > \omega_{LO}$ or $\omega_{LO} > \omega_S$. The IF $\omega_{IF}$ can be produced from a combination of inputs at $\omega_{LO} + \omega_{IF}$ or $\omega_{LO} - \omega_{IF}$. There are two frequency bands, placed on each side of the LO frequency. The frequency band higher than the LO frequency is called the signal band, while the lower band is called the image band. This connection is shown in figure 2.5
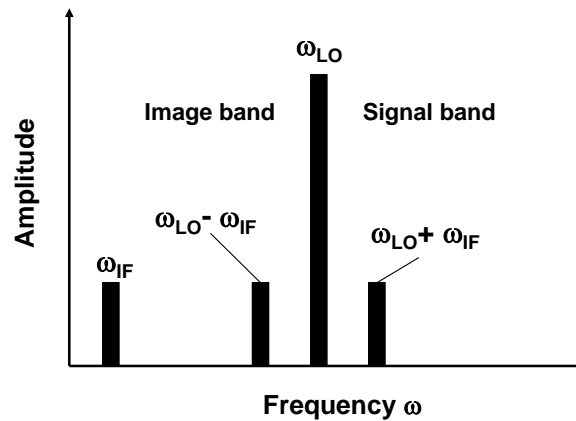


**Figure 2.5:** Illustration of the down-conversion and different side bands in a heterodyne receiver

A receiver which is sensitive to both sidebands is called double sideband (DSB) receiver, while a receiver which is sensitive to only one sideband is called single sideband (SSB) receiver.

The DSB receiver can operate in two different observing modes. For the observation of a broad band continuum source, the broad

continuum source covers both sidebands, this is the DSB operation mode. The additional signal power in the image band improves the sensitivity. For the observation of a narrow band spectral line contained within one sideband, the noise from the unwanted image band is added to the signal. This is the SSB operation mode of a DSB receiver. The noise temperature used to determine the sensitivity of the receiver usually is a DSB noise temperature. It is also possible to derive a SSB noise temperature for a DSB receiver:

$$T_{rec,SSB} = T_{rec,DSB}\left(1 + \frac{G_{image}}{G_{signal}}\right) \tag{2.9}$$

with $G_{image}$ the gain of the image sideband and $G_{signal}$ the gain of the signal sideband. For a DSB HEB receiver the $G_{image} \approx G_{signal}$, therefore

$$T_{rec,SSB} = 2\,T_{rec,DSB} \tag{2.10}$$

## 2.5.1 Heterodyne Mixing using HEBs

The HEB can be used as a heterodyne mixer. The incident radiation and the local oscillator (LO) radiation excite a voltage across the bolometer which can be written as:

$$V(t) = V_{LO}cos(\omega_{LO}t) + V_{S}cos(\omega_{S}t) \tag{2.11}$$

where $V_{LO}$ is the voltage induced by the local oscillator with the frequency $\omega_{LO}$ and $V_S$ is the voltage induced by the incident radiation signal with the frequency $\omega_S$. The dissipated power of the bolometer is:

$$
\begin{aligned}
P(t) \;=\;& \frac{V^2(t)}{R} = \frac{1}{R}\left[V_{LO}\,cos(\omega_{LO}t) + V_S\,cos(\omega_S t)\right]^2 \\
=\;& \frac{1}{R}\left[V_{LO}^2\frac{1+cos(2\,\omega_{LO}t)}{2} + V_S^2\frac{1+cos(\omega_S t)}{2}\right. \\
& \left. + 2V_{LO}V_S\frac{cos(\omega_{LO}+\omega_S)t + cos(\omega_{LO}-\omega_S)t}{2}\right] \\
=\;& P_{LO} + P_S + P_{LO}\,cos(2\omega_{LO}t) + P_S\,cos(2\omega_S t) \\
& + 2\sqrt{P_{LO}P_S}\,cos(\omega_{LO}+\omega_S)t \\
& + 2\sqrt{P_{LO}P_S}\,cos(\omega_{LO}-\omega_S)t \tag{2.12}
\end{aligned}
$$

using the average absorbed signal power $P_S = \frac{V_S^2}{2R}$ and the average absorbed LO power $P_{LO} = \frac{V_{LO}^2}{2R}$.

Since the average values of $2\omega_S$, $2\omega_{LO}$ and $\omega_{LO} + \omega_S$ are zero, they are not detected. Using $\omega_{IF} = |\omega_{LO} - \omega_S|$ the dissipated power of the bolometer can be written as:

$$P(t) = P_{LO} + P_S + 2\sqrt{P_{LO}P_S}\cos(\omega_{IF}t) \qquad (2.13)$$

The output power consists of a $\omega_{IF}$ term similar to the difference frequency of the electronic diode. Thus, a HEB can be used as a heterodyne mixer, if it is fast enough to follow the IF.

## 2.5.2 Phonon- and Diffusion cooled HEBs

The basic device configuration of a HEB device is shown in Figure 2.6. The key point is that the bolometer region consists of a superconducting thin-film microbridge (about 400-800 nm long) attached to two thick normal conducting contact pads at the end of the thin film strip. These contact pads lead to the antenna structure.
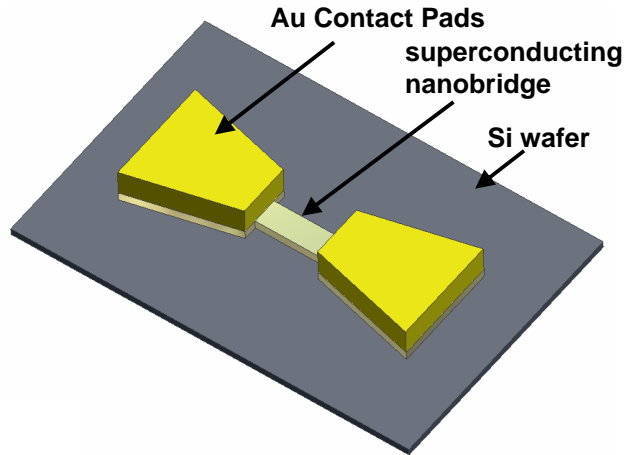


**Figure 2.6:** Schematic view of a hot-electron bolometer

There are two types of HEB mixers that have different cooling mechanism for the hot electrons: diffusion-cooled [12] and lattice- or phonon-cooled [13] devices.

In the diffusion-cooled HEBs, the hot electrons lose the excess energy through diffusing to the contact pads of the device. In addition to the diffusion of the hot electrons through the cooling pads, the hot electrons can transfer energy to phonons, which than carry the energy to the substrate. The film material and dimensions are chosen that way, to dominate a certain cooling mechanism.

A diffusion-cooled HEB mixer was first demonstrated at high frequencies with Niobium (Nb) as the material for the superconducting bridge [14]. To allow the diffusion cooling mechanism to be the dominant part in the cooling system, many materials (Nb, Ta, Al etc.) can be used as long as the device is short enough. The suitable length of the bridge should be shorter than the thermal diffusion length which is defined by

$$L_{th} = \sqrt{D\tau_{ep}} \qquad (2.14)$$

where $\tau_{ep}$ is the electron energy relaxation time via electron-phonon interaction and $D$ is the diffusion constant which is material dependent [15]. The typical length of a diffusion cooled HEB with a 10 nm thick Nb film is 0.1-0.3 $\mu$m [16].

Compared to the diffusion-cooled HEBs the phonon or lattice-cooled HEBs lose the energy of the hot electrons through phonon coupling to the underlying lattice. Phonon-cooled HEB mixers are typically fabricated from NbN films on either silicon or MgO substrates. NbN has a lower diffusion constant than Nb. The MgO substrate has the advantage that the phonon transmission probability is higher than for NbN on silicon [17].

Two parameters that are particular important for HEB mixers are the IF gain bandwidth and the IF noise bandwidth, because they determine the threshold for the minimum signal level that can be reliably detected. The IF gain bandwidth is defined as the IF frequency at which the conversion efficiency of the mixer drops by 3 dB from its low IF value. The noise bandwidth is the frequency at which the mixer input noise doubles compared to its zero frequency. Usually phonon-cooled HEB mixers achieve an IF gain bandwidth of a few GHz, whereas the noise bandwidth can be higher.

The most important parameters for a high intermediate frequency (IF) are the electron energy relaxation time via electron-phonon interaction $\tau_{ep}$ which becomes shorter if the superconducting film is thinner and the time of the phonon escape into the sub-

strate $\tau_{es}$ which depends on the acoustic coupling between the thin film and the substrate.

The NbN film of a current state-of-the-art phonon-cooled HEB is approximately 3.5 nm thick. Such HEBs have shown an IF gain bandwidth of 3.5 GHz (NbN on silicon) [18]. It was found that diffusion cooled Nb bolometers have a gain bandwidth to over 6 GHz [15].

One way to increase the IF bandwidth of a phonon-cooled HEB mixer is the use of a substrate material which is better acoustically coupled to the thin film. The use of a 3.5 nm ultrathin NbN film on Magnesium (II) Oxide (MgO) showed an IF gain bandwidth of 4.8 GHz [19].

A further increase of the IF bandwidth can be achieved by decreasing the film thickness. NbN films thinner than about 3 nm lose their superconductivity and become inhomogeneous.

It is difficult to compare the published bandwidth data, because the measured bandwidth depends strongly on the bias regime.

The first NbN phonon-cooled bolometric mixer for 1.04 THz used for radio astronomy was installed at the Submillimeter Telescope Observatory on Mount Graham, Arizona. Near 1.037 THz, the receiver noise temperature was 1600 K [20]. This was the first ground based observation at frequencies above 1 THz.

The main advantages of the phonon-cooled HEB mixers compared to the diffusion cooled HEBs is their stability. Phonon-cooled HEBs show a much weaker sensitivity to changes in the bias conditions.

## 2.5.3 Performance of Phonon-Cooled HEBs

The gain of a receiver system is the ratio of the signal output power to signal input power of the system. In heterodyne mixing the input signal is converted to a lower frequency by the mixing action, therefore the gain of a mixer is called conversion gain:

$$G = \frac{P_{IF}}{P_s} \tag{2.15}$$

with $P_{IF}$ the IF power and $P_s$ the signal power.

In heterodyne mixing, special emphasis goes to the IF bandwidth. The IF frequency at which the conversion efficiency of the mixer drops by 3 dB from its low IF value is called the IF gain bandwidth. The other bandwidth which is important for a HEB mixer

is the IF noise bandwidth, the frequency at which the mixer noise doubles compared to its zero frequency value.

The maximum IF gain bandwidth which can be achieved by a HEB mixer is defined by:

$$f_{\text{IFgain}} = \frac{1}{2\pi\tau_\theta} \tag{2.16}$$

with $\tau_\theta$ thermal time constant. The thermal time constant is a function

$$\tau_\theta \propto \tau_{ep}, \frac{C_e}{C_p}, \tau_{es} \tag{2.17}$$

of $\tau_{ep}$, the electron relaxation time via electron-phonon interaction:

$$\tau_{ep} = \frac{1}{T_c^{1.6}} \tag{2.18}$$

$\frac{C_e}{C_p}$, the ratio of the quasiparticle and phonon specific heats and $\tau_{es}$, the phonon escape time [19]. The phonon escape time $\tau_{es}$ is proportional to the film thickness d and inverse proportional to the acoustic transparency $\alpha$:

$$\tau_{es} \propto \frac{d}{\alpha} \tag{2.19}$$

The film strip, the bolometer is made of, should be very thin and should have a good acoustic transparency $\alpha$ and a high critical temperature, and it is important that $\tau_{es} << \tau_{pe}$, so that the phonons can escape to the substrate before they interact with electrons again.

## 2.6 HEB Models

HEB mixers are used in high-sensitivity instruments but there is still no satisfying theoretical model which describes the microscopic physical mechanisms that determines the behavior of a HEB in heterodyne mixing operation. The most common models that describe the interaction between the phonon subsystem, the Cooper pair subsystem and the quasiparticle (electrons from broken Cooper pairs) subsystem are described in the following sections.

## 2.6.1 Standard Model

This model was the first effort to develop a theoretical model which explains the operation of a HEB.

The standard model is also called the lumped element model because the bolometer is treated as a lumped element and assumes that the electrical properties like the electron specific heat and the thermal conductivity between the electrons and the substrate are constant along the microbridge. Also the RF power and the DC power applied to the bolometer create the same resistance change in the microbridge.

The LO power and the DC power raises the electron temperature close to the middle of the superconducting transition temperature. The much weaker RF signal power causes a further change of the temperature and therefore a further change in the resistance. If the HEB is biased by a constant current, an output voltage at the intermediate frequency is generated [12].

The heat balance equation can be written as [21]:

$$C_e V \frac{\partial T_e}{\partial t} + P_{e-s}(T_e, T_b) = I_0 V_0 + P(t) \tag{2.20}$$

where $T_e$ is the electron temperature, $T_b$ is the bath temperature, $V$ is the volume of the bolometer, $U_0$ and $I_0$ are the voltage and the current across the bolometer and $P(t)$ is the incident radiation power.

If the out-diffusion of phonons into the substrate is very fast, the power flow from electrons to the substrate can be written as [22]:

$$P_{e-s}(T_e, T_b) = A V (T_e^n - T_b^n) \tag{2.21}$$

where $A$ and $n$ are material-dependent constants. Since the RF and the DC power have the same effect on the electron temperature and the resistance of the bolometer, one can say:

$$C_0 = C_{dc} = C_{rf} = \frac{\partial R}{\partial P} \tag{2.22}$$

Based on this assumption the absorbed power can be estimated by using the isothermal technique which is described in section 7.5.6.

Using this model it is possible to determine characteristic properties of a HEB, like the electron specific heat. It is also possible to determine mixing properties like the gain or the absorbed LO power.

23

The behavior of the HEB depends on the measured R-T curve. To measure the R-T curve the temperature of the entire HEB is changed and the change in resistance is a result of the heating of the entire bridge. But in an heterodyne experiment the HEB is operated at a temperature of 4.2 K, therefore the R-T curve does not fully describe the behavior of the microbridge during a heterodyne operation.

### 2.6.2 Hotspot Mixing in Hot-Electron Bolometers

The main disadvantage of the previous described model is that it neglects diffusion of electrons and that the effective temperature remains uniform within the whole device.

The hotspot mixing model is based on the fact that a DC current creates a local hotspot in a superconducting microbridge which is maintained by self-heating [23]. The electron and phonon temperature inside this hotspot is higher than the critical temperature of the superconductor, being the reason for the resistive state.

The basic concept of the hotspot mixing model depends on the fact that the DC power and the RF power of the LO and the signal generate a hotspot inside the microbridge of the HEB. The length of the hotspot and therefore the resistance oscillates with the heating power at the intermediate frequency [24].

The heat balance equation of a HEB with applied LO power can be written as:

$$-K\frac{d^2T}{dx^2} + \frac{c_e}{\tau_{e-ph}}(T - T_b) = j^2\rho + P_{LO} \text{ (inside the hotspot)} \qquad (2.23)$$

and

$$-K\frac{d^2T}{dx^2} + \frac{c_e}{\tau_{e-ph}}(T - T_b) = P_{LO} \text{ (outside the hotspot)} \qquad (2.24)$$

where $K$ is the thermal conductivity, $T$ is the electron temperature, $c_e$ is the electronic heat capacity, $\tau_{e-ph}$ is the electron-phonon interaction time, $\rho$ is the normal state resistivity and $p_{LO}$ is the LO power per unit volume [24].

## 2.7 Summary

Bolometers are very sensitive thermal detectors. Superconductors are used to increase the sensitivity of the bolometer, since super-

conductors show a very strong dependence of resistivity with temperature.

Hot-electron bolometers (HEBs) are used for the detection of millimeter- and submillimeter radiation. The term *hot electrons* refers to electrons which are not in thermal equilibrium with the lattice. Two different types of HEBs exist, phonon-cooled and diffusion cooled HEBs. In diffusions-cooled HEBs the hot electrons loose their energy by diffusion into the cooling pads, while dominate cooling mechanism in phonon-cooled HEBs is the transfer of energy to the substrate. Diffusion-cooled HEBs show a much larger IF bandwidth, but they are too unstable to operate in a receiver. Phonon-cooled HEBs are very stable, but show a smaller IF bandwidth.

The thermal time constant $\tau_\theta$ determines the IF bandwidth of a HEB mixer. The thermal time constant is a function of the electron-phonon relaxation time, the phonon escape time and material intrinsic parameters.

Thin superconducting films having a high critical temperature $T_c$ and a good acoustic transparency $\alpha$ to the substrate are necessary for the fabrication of HEB mixers.

# Chapter 3

# Thin Film Development

## 3.1  Introduction

The thin films necessary for the hot-electron bolometer (HEB) fabrication are produced by depositing a thin layer onto a carrier material. Processes usually used to deposit a thin layer are physical vapor deposition (PVD), chemical vapor deposition (CVD), electrodeposition and plasma spraying.

The standard method for the deposition of high-quality superconducting films onto substrates is PVD. PVD produces thin films by evaporation or sputtering.

In the evaporation process, the source material is heated to its evaporation temperature. A wire or a sheet of metal is used in this process. A current is applied to the wire or the sheet of metal which generates enough heat to cause vaporization of the source material. The evaporated material condenses on a substrate and forms the thin film. Beside using a resistive heating it is also possible to use a high power electron beam to evaporate the source material (e-beam evaporation).

In the sputtering process, the atoms of the source material are sputtered from the surface as a result of a bombardment with high-energy particles. The high-energy particles, usually argon (Ar) ions, are generated by a glow discharge.

Sputtering has many advantages compared to evaporation such as:

- A greater number of materials such as alloys and compounds can be sputtered.

- A higher packing density of the film can be achieved.

- a better adhesion between film and substrate can be achieved, if the film stress is low.

- Control of film composition and grain structure is more easily accomplished by sputtering.

- Better step coverage, because the material beam is non-directional.

The main disadvantage of the sputtering process should be mentioned as well. Sputtering involves many more process parameters than evaporation. Also, some materials like $SiO_2$ have a very low sputtering rate.

This chapter shows an overview of the PVD process of sputtering. A more detailed characterization of the reactive sputtering process follows.

The sputtering parameters for a certain film are not known in advance. To obtain a film with desired properties a large amount of variables must be investigated and controlled even more so for ultrathin films. The chapter closes with a detailed description of the development of ultrathin niobium nitride (NbN) and ultrathin niobium titanium nitride (NbTiN) films necessary for the fabrication process of HEBs.

## 3.2   Magnetron Sputtering

The technology of sputtering deposition ranges over a wide variety of applications from high-performance coatings applied to cutting tools to high temperature superconducting film deposition.

Figure 3.1 shows a schematic view of a sputtering deposition chamber. Sputter deposition is a vacuum coating process. In the sputtering process an electrical potential $U$ is applied to a target consisting of the material to be sputtered, which is attached to a cathode in the discharge environment inside a vacuum chamber which is evacuated to a base pressure of typically $10^{-6}$ to $10^{-8}$ mbar. The substrate faces the target and a glow discharge is initiated and sustained by gas introduced into the chamber.

The ions of the so called working gas (such as argon) are accelerated towards the target and sputter the target material. The discharge is sustained by secondary electrons produced at the cathode by the impact of the energetic ions, which leads to an additional
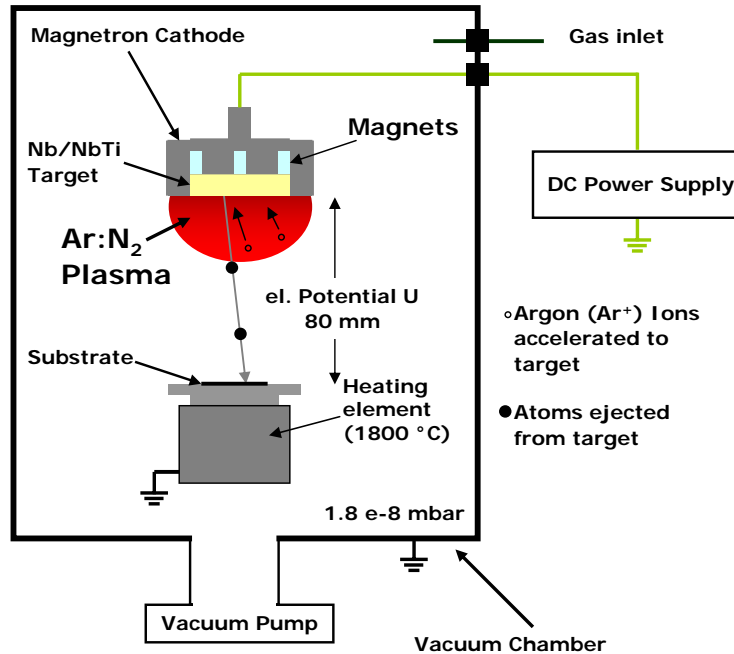
**Figure 3.1:** Schematic view of a sputtering deposition chamber used for the deposition of superconducting ultrathin films.

ionization of the gas. The distance between cathode and target $d$ and the gas pressure $p$ determine the break-through voltage $U_d$. The break-through voltage $U_d$ determines the point from which on the self sustaining gas glow discharge starts.

To enhance the sputtering yield at the cathode, a magnetic field is applied close to the target material, which causes the electrons to circulate over the target surface evoked by its magnet field which is in the order of a few 100 Gauss. This kind of sputtering is called magnetron sputtering. The electrons generate a much higher ionization probability and therefore the plasma ignition takes place at lower gas pressures compared to conventional sputtering.

Another advantage of magnetron sputtering compared to conventional sputtering is the higher density of ionized argon atoms which result in a higher deposition rate at lower pressures. Also

less secondary electrons reach the substrate and therefore the substrate is less heated compared to conventional sputtering.

## 3.3  Reactive Sputtering

Reactive sputtering is a method to deposit films which have a different composition from the target by adding a reactive gas to the conventional magnetron sputtering process to form, depending on the reactive gas, oxides, nitrides, carbides and other compounds.

The reactions can take place at the target, in the gas phase and on the substrate. Target reactions result in actually sputtering a compound target. These usually have a lower sputter yield (which is the number of sputtered particles of the target per primary ion) than elements and result in a reduction in deposition rate [25]. Attempts to sputter from targets of stoichiometric superconducting compounds produced degraded superconducting properties of the thin film. This is due to the presence of oxides within the grain boundaries inside the target material [26].

Reactive sputtering is the favorable method for the deposition of thin NbN and NbTiN superconducting layers necessary for the fabrication of phonon-cooled HEBs. One basic problem of the reactive sputtering process is to determine the essential process parameters to control the superconducting film growth and quality.

The most important process parameter in the preparation of thin films by reactive sputtering is controlling the partial pressure of the reactive gas.

The partial pressure of the reactive gas is a function of the reactive gas flow rate in a glow discharge process. A hysteresis loop occurs, which is unwanted for the deposition of a superconducting film with a desired crystal structure and the required stoichiometry [27]. The sputtering of the target surface and the deposition of the reactive product on the target surface determine the hysteresis loop. An idealized reactive sputtering hysteresis loop for the partial pressure $p$ and the flow rate $\rho$ of the reactive gas is shown in figure 3.2.

The graph clearly shows the dynamics taking place in a reactive sputtering process. For a low flow rate of the reactive gas, its partial pressure remains zero. This is caused by pumping the reactive gas with the vacuum pump and the reaction of reactive gas on surfaces within the deposition chamber. This phenomenon is
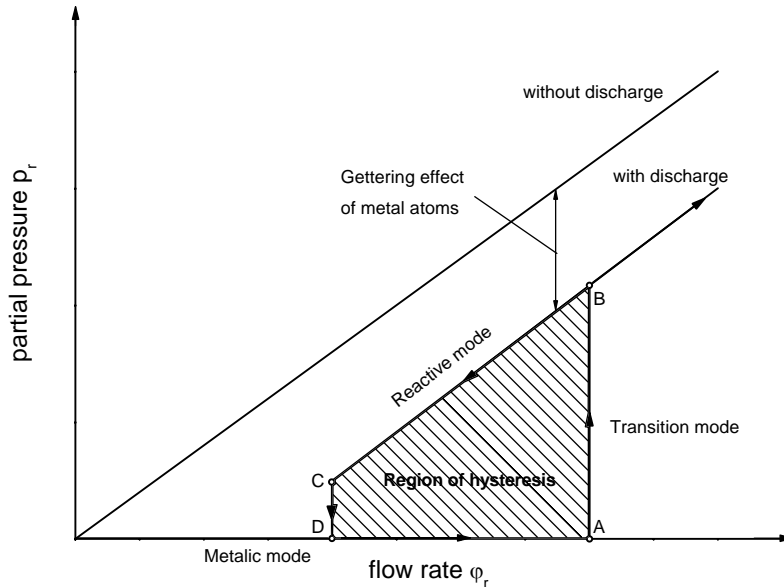
**Figure 3.2:** Hysteresis loop of the flow rate ρ and the partial pressure p of the reactive gas occurring in a reactive sputtering process (taken from [27])

called gettering. This part of the sputtering process is called the metallic mode, because only the metallic target material is sputtered. The metallic mode is characterized by a high deposition rate and metal sputtering occurs. The deposited film is a metal film doped with atoms form the reactive gas - in the case of nitrides the film is called "under-nitrogenized". The discharge voltage and current barely differ from the values for sputtering in a pure working gas atmosphere [28].

Beyond point A, indicated in figure 3.2, the gettering process is saturated and the limited pumping capacity leads to an increase of the partial pressure of the reactive gas and a decrease in deposition rate. The target and the deposition chamber walls are coated with a layer of the reactive compound. Because of the presence of the compound layer on the target surface, the target is called poisoned. When the target becomes poisoned, the sputtering rate drops rapidly because the compound will have a lower sputter-

ing yield than the purely metallic surface [29]. When the target is poisoned, several instabilities can occur like arcing, because an increase in secondary electron emission from the compound surface takes place, especially when sputtering nitrides [30]. Due to the lower sputtering rate, less reactive gas is consumed, and its partial pressure jumps to a much higher level, which differs from the partial pressure without discharge.

Increasing the flow rate $\rho_r$ further causes a higher partial pressure, but the difference in pressure with and without discharge will remain constant. This pressure difference corresponds to the amount of reactive gas included into the deposited film, which is now a stoichiometric compound. Therefore this mode is called reactive or compound mode. In the reactive mode the sputtering rate is very low because of the lower sputter yield of the compound and the higher secondary electron emission of the compounds [28]. By decreasing the flow rate below point B the system remains in the reactive mode and returns into the metallic mode for flow rates below a certain value (point C).

The optimal value of the reactive gas flow rate $\rho_r$ is located within a narrow range around point A/B. Then it is possible to deposit a compound film with good stoichiometry at a comparable rate to that of the metallic film [31].

This scenario makes it difficult to control the sputtering rate and the film composition by simply controlling the flow of the reactive gas.

A solution to deal with this difficulty is described in section 3.6.

## 3.4   Thin Film Formation on the Substrate

The next step which takes place in the thin film deposition is the film growth on the substrate.

This process involves the condensation of the vaporized atoms or molecules onto the substrate, followed by the formation of the film by nucleation. The next stage is the interface formation and finally the continuous growth process of the thin film [32].

When using PVD, the sputtered material reaches the substrate in an atomic or molecular form. The atoms reaching the surface of the substrate can either condense on the surface, re-evaporate after a residence time or can be reflected immediately. If the atoms do not condense on the surface immediately they are called adatoms

and they have a surface mobility. The adatoms can diffuse above the substrate surface with a motion determined by its binding energy to the substrate, the temperature of the substrate and the energy of the adatom [33].

The adatoms condense on the substrate surface and after a certain time the atom will either evaporate from the surface or will join with another diffusing single atom to form a doublet [25]. The atomic motion occurs on length scales of the order of Angstroms, and time scales that reflect the typical atomic vibration frequencies (i.e. $10^{-13}s$) [34]. The chance of re-evaporation of a doublet is much smaller than the chance of re-evaporation of a single atom, but the doublets will trap other single atoms to form triplets etc. This phase of thin film formation is called nucleation stage of the film growth. Surface contamination can influence the nucleation density and the nuclei orientation [35].

The nucleation phase starts statistically with the formation of three-dimensional islands of atoms. Preferred positions where the nucleation starts are surface discontinuities (scratches or steps), lattice defects, foreign atoms in the surface or surface areas with different crystallographic orientation [36].

The islands start to grow in size rather than in number because the mean free path of diffusing atoms, doublets etc. is equal to the mean island separation and atoms will attach themselves with much higher probability to existing islands than to create new ones. When these islands grow large enough to touch, this stage of film-formation is called coalescence stage.

The deposited film can react with the substrate to form an interfacial region. The structure, composition and thickness of the interface region can be influenced by substrate surface preparation or cleaning, substrate temperature and deposition time [36].

The coalescence stage leads to a macroscopic network, and at the percolation thickness, optical and all other properties change abruptly and further thickness growth leads to a polycrystalline real structure.

The film grows by a further nucleation of the depositing atoms on the previously deposited material. The deposited film generally grows in a columnar morphology. For ultrathin films ($<$ 5 nm) the substrate effects are dominant and they usually show a poor crystal quality, columnar growth occurs for much thicker films ($>$ 80 nm), but this depends on the deposited material [37].

It is important to notice that the film growth could vary over the

substrate surface due to surface inhomogeneities.

## 3.5   Superconducting Films for HEB Devices

HEB devices are based on ultrathin superconducting films. Two different compounds of niobium (Nb) have been used as superconductor in this work: Niobium titanium nitride (NbTiN) and niobium nitride (NbN).

Both are type-II superconductors and have similar superconducting properties. Bulk NbTiN has a critical temperature of 16-17 K and a resistivity of around 90 $\mu\Omega$cm (at 300 K) [38]. A critical temperature of 16 K and a resistivity of 160 $\mu\Omega$cm (at 300 K) can be found for NbN [26].

## 3.6   Properties of Reactive Sputtering

In order to realize the process of reactive sputtering described above some practical problems have to be solved.

Usually a voltage- or power stabilization is used for reactive magnetron sputtering. Figure 3.3 shows the current-voltage (I-V) characterization of the magnetron cathode, which was used for the deposition of NbTiN. The cathode was operating under the conditions of voltage stabilization.

At low discharge voltages, the deposition rate of the compound on the target is *higher* than its sputtering rate, the target is poisoned. At a certain voltage, the deposition rate of the compound becomes *smaller* than the sputtering rate of the target. At this stage the target becomes more metallic. The sputtered metal absorbs more reactive gas and the reactive gas pressure decreases. This causes a much greater depletion of the compound on the target surface. The current increases because the sputter yield of the metal is larger than the sputter yield of the compound. This causes a hysteresis in the I-V-characteristic of a voltage-stabilized magnetron sputtering environment [39].

The I-V characteristic of the magnetron niobium titanium cathode using a current stabilization looks completely different (see Figure 3.4). The curve shows almost no hysteresis compared to the

**Figure 3.3:** Current-voltage (I-V) characterization of a NbTi magnetron sputtering cathode using voltage stabilization in a $Ar/N_2$ and in pure argon gas mixture. The curve for the reactive sputtering ($Ar+N_2$) shows a clear hysteresis loop.

I-V curve of the voltage stabilized cathode, because the current stabilization compensates for the change in the sputtering rate occurring at the transition from the metallic to the reactive mode.

When the current is kept constant, the sputtering process is held in an equilibrium state. If the sputtering rate increases, the area of the target covered with the compound material gets smaller and the sputtering rate of metal increases. A higher amount of metal-atoms absorbs more reactive gas, so the partial pressure of the reactive gas decreases and the discharge voltage as well. The sputtering rate than returns to its initial value.

This results in a correspondence between the discharge voltage U, the partial pressure of the reactive gas $p_r$ in the discharge and the fraction of the target coated by the compound [39]. As described above the most important parameter in reactive sputtering is the partial pressure of the reactive gas $p_r$. Its control is essential and can be observed by monitoring the discharge voltage U.

To ensure a precise control of the reactive partial gas pressure, the technique of monitoring the discharge voltage is widely

**Figure 3.4:** Current-voltage (IV) characterization of a NbTi magnetron sputtering cathode using current stabilization in a $Ar/N_2$ gas mixture. The curve shows almost no hysteresis compared to the IV curve of the voltage stabilized cathode.

used [39].

# 3.7 Deposition of Ultrathin NbN/NbTiN Films

To fabricate thin films such as NbTiN or NbN with good crystalline orientation and a proper stoichiometry, the determining factor is the nitrogen ($N_2$) content in the film. A variation of the nitrogen content in the film has the effect of changing the lattice constant of the nitride which results in different values of the film critical temperature $T_c$ [26].

The film properties also show a strong dependence on the other magnetron sputtering conditions such as argon partial pressure, substrate temperature during deposition and the sputtering rate.

Beside the strong dependence on the sputtering parameters the critical temperature decreases with the thickness of the film especially when the mean free path $l$ becomes much smaller than the

zero-temperature coherence length $\xi_0$ in the superconductor. This is called the "dirty limit" of a superconductor. In this thesis superconducting films in the "dirty limit" are called ultrathin films, while superconducting films in the clean limit are called thin films.

NbN is a superconductor with a coherence length of $\xi_0 = 5$ nm [40] and NbTiN also has a very short coherence length of $\xi_0 = 3.8$ nm [41].

The following approach was used to find the optimum sputtering parameters for the deposition of NbN and NbTiN ultrathin films. This method is one way to find the optimal sputtering parameters rather than the only or optimum method. The following description of the development of ultrathin films is shown for NbN films in detail. Finding the optimal sputtering parameters for ultrathin NbN films is basically very similar to the optimization process for NbTiN ultrathin films.

The NbN and NbTiN films are deposited in a custom-made load locked cryopumped DC magnetron sputtering system. The sputtering machine is equipped with a heated and a water cooled substrate table and is working at a base pressure of $2 \times 10^{-8}$ mbar.

A 76.6 mm diameter Nb/NbTi alloy sputtering target (99.7 purity), with argon ($\geqslant$ 99.9999 % purity) and nitrogen ($\geqslant$ 99.9999 % purity) as sputtering gas is used. The target to substrate separation is approximately 8 cm. The radio of Nb to Ti in the NbTi target is found to be the best trade-off between the critical temperature $T_c$ and the resistivity $\rho$ by using 78 % Nb to 22 % Ti by weight [42].

## 3.7.1 Measurement Methods for Electrical Properties of Thin Films

The aim of the ultrathin film development is to deposit ultrathin films as thin as possible. For NbN it is known, that films thinner than 3 nm do not become superconducting at all [43]. Thus, film thicknesses of 3-4 nm are desired for the HEB fabrication. There is a difference between depositing thin and ultrathin NbN films.

The layer roughness is determined by the NbN grain size. The grain growth is typically in the order of 5-10 nm for NbN films and results in larger grain sizes with increasing film thickness [26]. The surface roughness of the NbN layer does not increase for thicker films, because the fine polycrystalline structure "averages

out" the effects of roughness in successive layers. An atomic mismatch at the grain boundaries appears in polycrystalline structures and these mismatches are important for the physical and electrical properties of the material. Therefore ultrathin NbN layers (5-10 nm) may have different electrical properties than thicker NbN layers ($>$ 20 nm). Five samples of about 5 nm ultrathin NbN films are deposited on high-resistivity silicon (Si) substrates to determine the optimal nitrogen flow, rather than thicker ($>$ 20 nm) NbN films.

The measurable properties of the ultrathin NbN films are the critical temperature $T_c$ and the resistivity $\rho$. The critical temperature $T_c$ (defined as the mid point temperature of the resistance versus temperature transition) and in addition, the resistivity $\rho$ just above the critical temperature (normally measured at 20 K) of the films are good indicators of the film quality.

To measure the critical temperature a simple liquid helium probe (dipstick) setup was used. The dipstick is essentially a metal tube having a probe holder on the lower portion of the dipstick. At the upper end there is a connector port to connect the dipstick to the PC-controlled measurement setup.

The PC-controlled experimental setup for the resistance vs. temperature (R-T) measurement uses a dual lock-in system, National Instruments data acquisition cards and dedicated control software [44]. The dipstick measurements are performed in liquid helium at 4.2 K. The temperature of the sample can be increased above 4.2 K by slowly extracting the dipstick from the helium container. A temperature diode is integrated at the probe mount in direct vicinity of the sample.

The Van der Pauw [45] structure is used to measure the sheet resistance and the critical temperature. The structure used here is shown in figure 3.5. The structure consists of an arbitrarily shaped piece
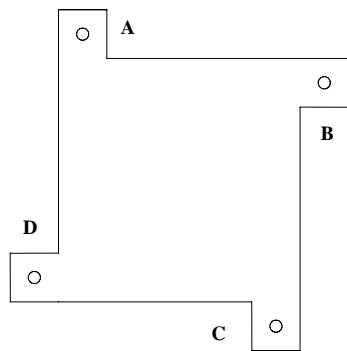


**Figure 3.5:** Van der Pauw structure with bonding contact pads (A, B, C, D)

of thin film, with 4 small contacts placed on the periphery of sample.

By taking voltage measurements from adjacent leads when cur-

rent is forced through the other 2 leads, then rotating the lead positions by 90°, any asymmetry in the structure can be corrected by using a mathematical function [45]. This structure is symmetrical by design, so the measured resistance values do not need to be corrected.

Still, the average of the two measurements yields a better estimate of the sheet resistance of the underlying material. The area of the sample is about 2.3 $mm^2$. The only process parameter that is needed for the calculation of the resistivity of the sample is its thickness.

The NbN films are patterned by etching (Ar and $SF_6$), defining the van der Pauw structure using the negative photo resist AZ 5214.

The van der Pauw optical lithography mask used for the lithographical patterning also contains some solid strips of different width. These strips can also be used to measure the resistivity and critical temperature.

## 3.7.2  Optimizing the Sputtering Parameters for Ultrathin NbN Films

As mentioned above the most important parameter for the deposition of NbN films by reactive sputtering is the partial pressure of the reactive gas. In order to find a reasonable starting range for the nitrogen flow, the complete curve of nitrogen flow versus target voltage for the Nb cathode has to be recorded first.

To determine this curve, a fixed argon flow rate is introduced into the sputtering chamber and the cryopump is throttled to result in an argon partial pressure of 0.5 Pa. To remove any Nb target contamination the target is pre-sputtered by pure argon as sputtering gas for 15 min. Figure 3.6 shows the nitrogen flow rate versus target voltage of the niobium cathode.

The sputtering power determines the deposition rate of the deposited compound. For ultrathin films a sputtering rate of 2-5 Å/s is desired. For this sputtering system a constant current of 0.3 A results in a sputtering rate of roughly 3 Å/s and therefore 0.3 A is set as a starting point. Then nitrogen is introduced into the sputtering chamber progressively in 0.25 sccm[1] increments. The

---

[1][sccm], standard cubic centimeters per minute
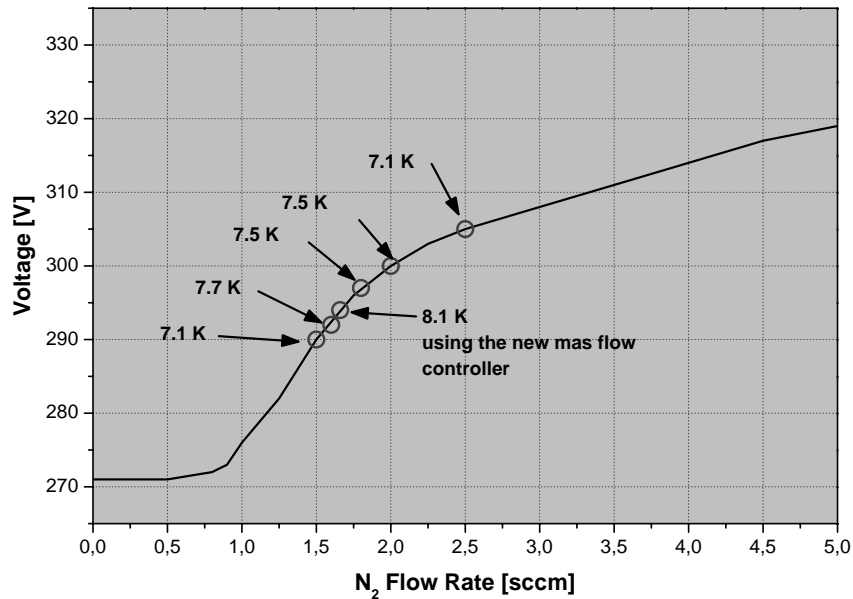
**Figure 3.6:** Target voltage for different nitrogen ($N_2$) flow rates of the Nb cathode, at a constant current of 0.3 A and 0.5 Pa argon partial pressure. The critical temperature $T_c$ of 5 nm ultrathin NbN films for different $N_2$ flow rates is indicated as well. This graph shows only the voltage resulting from the increase of the $N_2$ flow, therefore it does not show any hysteresis that would show up in a similar curve with decreasing $N_2$ flow rate.

throttle valve is kept at a constant position so that the total pressure can vary with the $N_2$ flow rate. As nitrogen is introduced into the system the target voltage increases stronger than linearly. The target voltage curve for 0.5 Pa argon partial pressure is shown in figure 3.6. This graph shows only the voltage resulting from the increase of the $N_2$ flow, therefore it does not show any hysteresis that would show up in a similar curve with decreasing $N_2$ flow rate.

The critical temperature of 5 samples deposited at different operating points in the curve are also shown in figure 3.6. The deposition rates at 1.6 sccm and 2.0 sccm $N_2$ flow rate were determined in the first place. The deposition rates should be slightly different. It was not possible to measure the difference in deposition rates because this value was within the error range of the thickness measurement which is described in section 3.7.5. All five sample were

estimated to be about 5 nm thin.

The $T_c$ shows a maximum of 7.7 K for 1.6 sccm $N_2$. The range of the nitrogen flow rate, which results in the maximum critical temperature is very narrow. A flow rate of 1.6 sccm $N_2$ results in the maximum critical temperature $T_c$ of 7.7 K. The nitrogen flow rate can be related to the nitrogen partial pressure by using the $\Delta U$ method described in section 3.6.

The resolution of a mass flow controller is determined 0.1 % of the maximum flow rate. The flow controller used for the 5 NbN samples had a maximum flow rate of 100 sccm and therefore a resolution of 0.1 sccm. By using a mass flow controller with a maximum flow rate of 20 sccm which was built in later on, it was possible to adjust the nitrogen flow rate between 1.6 sccm and 1.7 sccm. Using this mass flow controller and a flow rate of 1.66 sccm it was possible to deposit a 5 nm ultrathin NbN film having a critical temperature $T_c$ of 8.1 K. This value is also indicated in figure 3.6.

Not only the partial pressure of the $N_2$ reactive gas, but also the partial pressure of the argon working gas has an effect on the film quality. Westra et al. found that the maximum $T_c$ increases with decreasing argon partial pressure [46].

Ultrathin films with successively decreased argon partial pressure have been fabricated.

Figure 3.7 shows the $R - T$ curves for NbN ultrathin films deposited for fixed nitrogen partial pressure at five different argon partial pressures. Decreasing the argon partial pressure from 0.75 Pa below 0.52 Pa results in a dramatic increase in critical temperature $T_c$ of + 1.5 K, from $T_c$ = 6.2 K for 0.75 Pa argon partial pressure to $T_c$ = 7.7 K for an argon partial pressure below 0.5 Pa.

The transition width $\Delta T_c$ (defined as the temperature range from 90% to 10% of the resistance value of the R-T transition) becomes slightly smaller, from $\Delta T_c$ = 2.7 K for 0.75 Pa argon partial pressure to $\Delta T_c$ = 1.8 K below 0.5 Pa argon partial pressure.

For argon partial pressures below 0.52 Pa no change in the critical temperature is observed compared to the the films sputtered at 0.52 Pa argon partial pressure. A lower argon partial pressure results in a higher film stress, at a thickness of 5 nm, the film stress is irrelevant.

The plot legend reads:

- - - - 0.75 Pa Ar partial pressure, $T_C$ = 6.2 K, $\Delta T_c$ = 2.6 K
...... 0.66 Pa Ar partial pressure, $T_C$ = 6.4 K, $\Delta T_c$ = 2.2 K
——— 0.52 Pa Ar partial pressure, $T_C$ = 7.7 K, $\Delta T_c$ = 1.8 K
—·—· 0.44 Pa Ar partial pressure, $T_C$ = 7.7 K, $\Delta T_c$ = 1.8 K
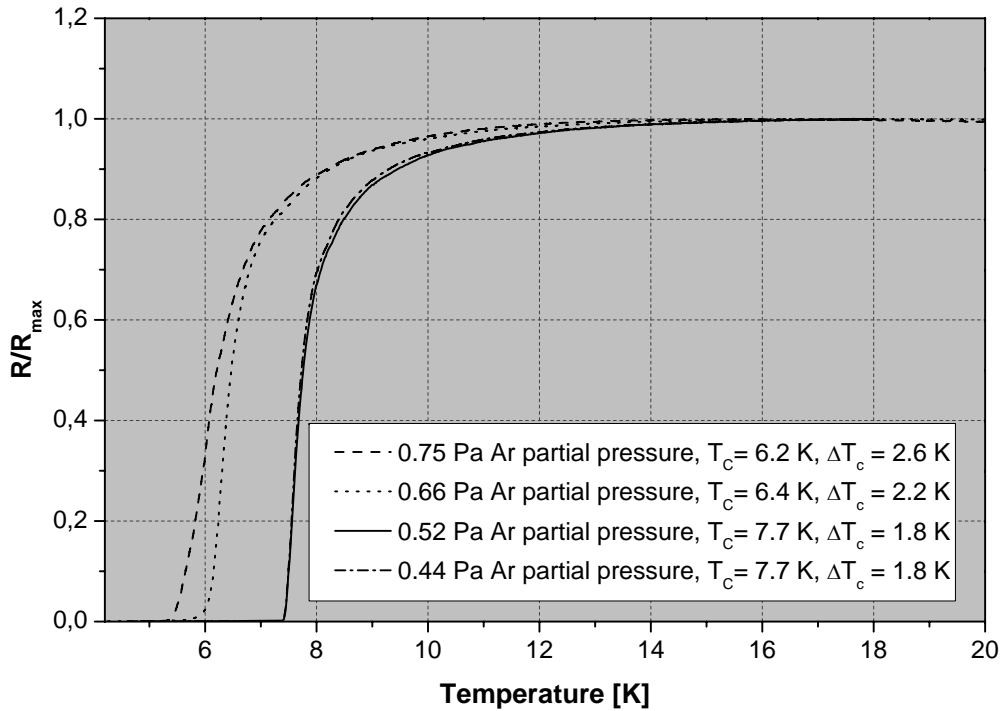
**Figure 3.7:** R−T curves using the optimal nitrogen partial pressure for different argon partial pressures.

## 3.7.3 Influence of Substrate Heating

The substrate temperature during reactive sputtering is found to be an important parameter for the film quality [47].

In the used sputtering system, substrate heating is achieved by a radiative Boralectric® heater [48], based on a PBN/Pyrolytic Graphite resistance heating element with an operating temperature up to 1800°C, which is located 8 mm below the titanium (Ti) substrate holder. Figure 3.8 shows a schematic view of the heating system designed for the sputtering system.

In a high vacuum (HV) system, the thermal heat transfer between the heating element and the substrate is dominated by thermal radiation. The heating element and the substrate holder do not have the same temperature. It was not possible to minimize the distance between the heating element and the substrate holder any further or even put them in a mechanical contact.
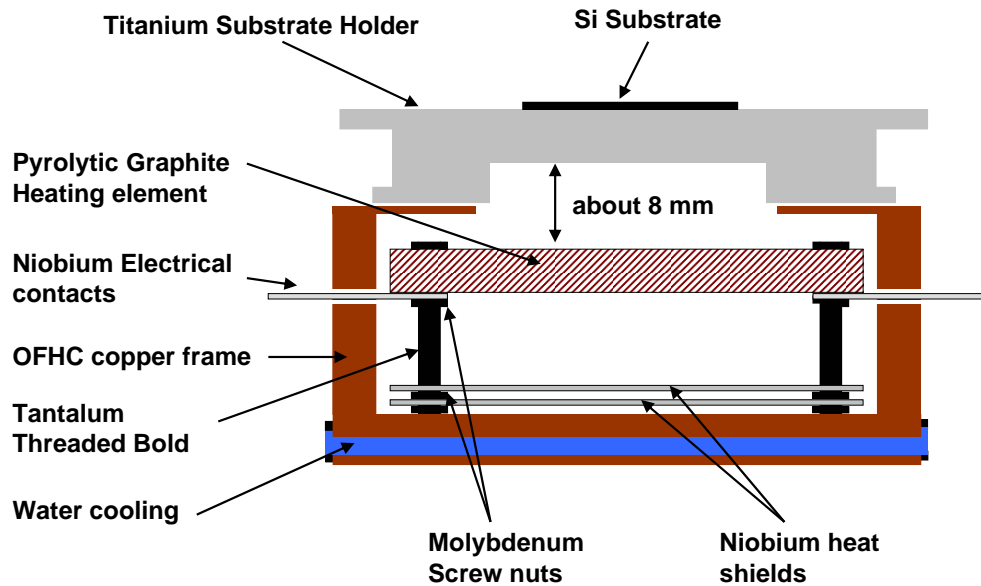
**Figure 3.8:** Schematic view of the heating system designed for the sputtering system

To estimate the temperature of the substrate fixed to the substrate carrier, a PT-100 temperature sensor was mounted on the surface of the substrate carrier, giving a calibration of the PG heating element versus substrate temperature. The temperature of the heating element was measured by a thermocouple which was assembled into a hole in the lateral heater plane.

Figure 3.9 shows the temperature of the heating element and of the substrate holder surface versus time by progressive temperature stages of 100°C. The difference between the heater temperature and the substrate surface at 650°C is about 180-200°C. After 20 min. the heating element and the substrate holder are in a thermal equilibrium, within the limits of this experiment. From this measurement it can be roughly estimated that the surface substrate holder temperature is about 600°C if the heating element has a temperature of 800°C. Only the surface temperature of the substrate holder was measured, the actual surface temperature of the substrate can only be estimated.

The background pressure of the vacuum chamber is also shown in figure 3.9. The background pressure remains constant for substrate surface temperature values lower than 450°C. The in-
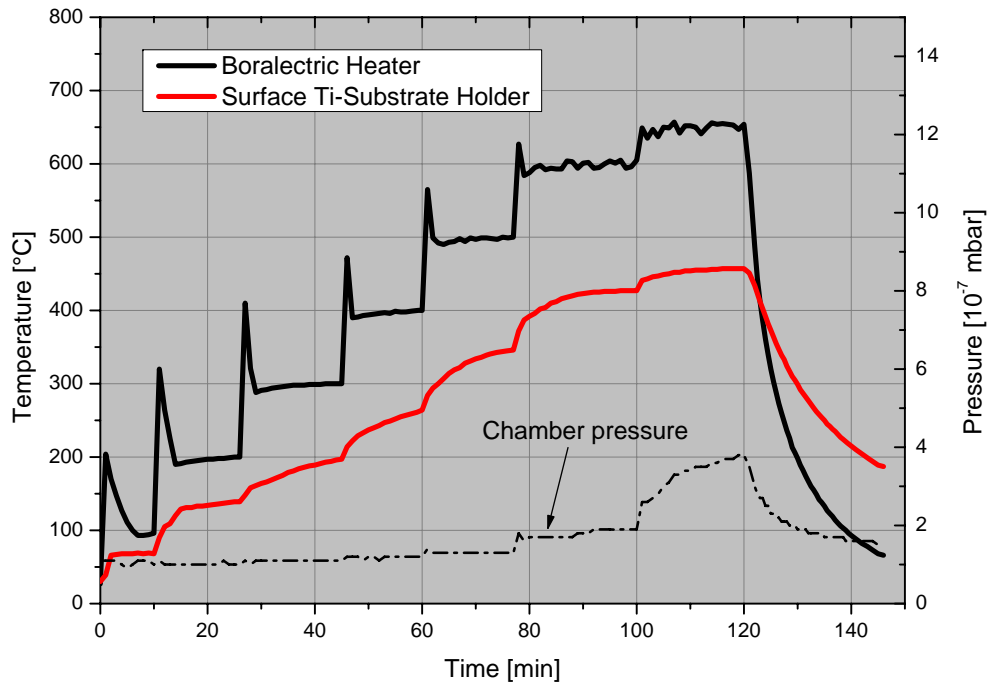
**Figure 3.9:** Temperature measured at the heating element and at the substrate surface for different heating steps (right axis). Also shown is the background pressure of the vacuum chamber (right axis).

creased background pressure for substrate temperatures higher than 450°C is due to outgassing of components inside the vacuum chamber, especially close to the heater station. Outgassing means that trapped or frozen gas inside a material is released. Outgassing is a great problem for the deposition of thin film, since the gas released from components inside the vacuum chamber is build into the deposited thin film.

Heating the substrate during the deposition process improves the crystalline order in the films and increases the grain size [49]. This is due to an increased surface mobility of the adatoms of the deposited material as described in section 3.4.

The influence of heating the substrate during deposition on the superconducting properties of 5 nm ultrathin NbN films is shown by the R-T curves in Figure 3.10. Heating the substrate up to 600°C significantly increases the critical temperature $T_c$ from 8.1 K
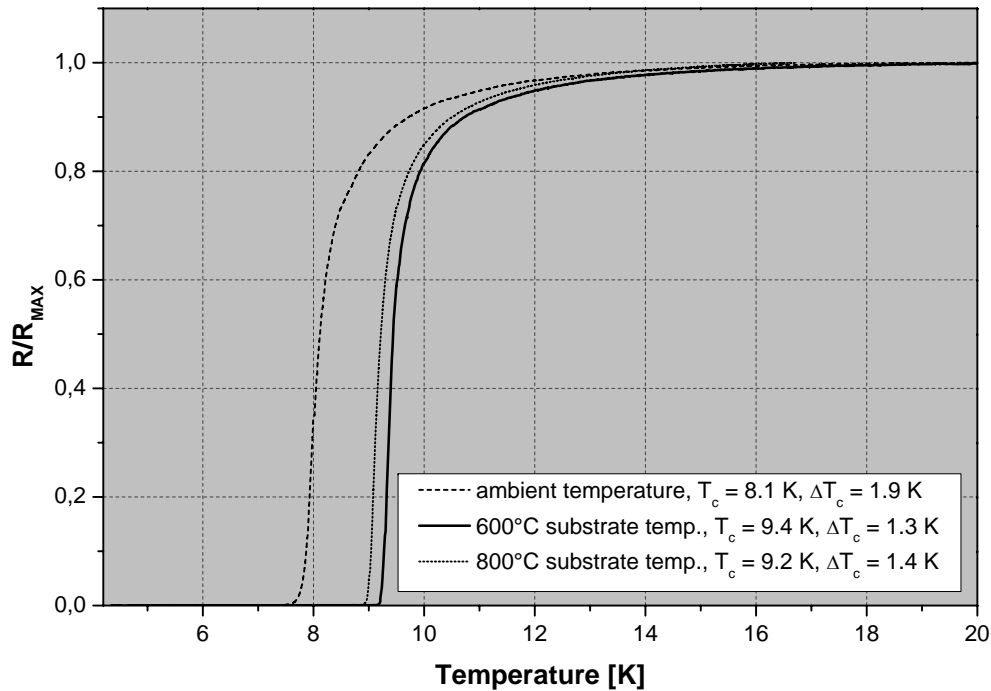
**Figure 3.10:** R-T curves of 5 nm ultrathin NbN films on Si-substrates for different temperatures during deposition.

at ambient temperature to 9.4 K. The transition width $\Delta T_c$ becomes slightly smaller.

Increasing the substrate temperature up to 800°C causes a minor increase of the critical temperature compared to 600°C. An increase of +0.9 K for the critical temperature compared to ambient temperature can be observed. A higher substrate temperature results in a higher quality of the deposited ultrathin film. But the outgassing of components inside the sputtering system increases with temperature. This is observed by the dramatic increase of the background pressure at a heating element temperature of 1000°C (about $2 \cdot 10^{-6}$ mbar). Therefore a heating element temperature of 800°C which results in a substrate holder surface temperature of 600°C was chosen as a tradeoff between background pressure and heater temperature.

Presently, most of the NbN films used for the fabrication of HEB devices are fabricated at the Moscow State Pedagogical University (MSPU) [39]. The process uses a temperature of 900°C. From the

literature it is not quite clear if the Moscow group means the heater temperature or the substrate temperature. In the majority of cases just a deposition temperature is reported.

### 3.7.4 Role of the Interface Layer

The surface of silicon (Si) wafers reacts with oxygen ($O_2$) or steam ($H_2O$) to form a silicon dioxide ($SiO_2$) layer when exposed to air. This is called the native oxide layer of the Si substrate.

$$Si + O_2 \longrightarrow SiO_2$$
$$Si + 2H_2O \longrightarrow SiO_2 + 2H_2$$
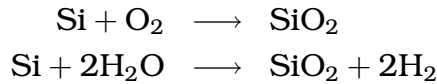
The thickness of this $SiO_2$ layer is between 0.6 and 2.0 nm and depends on the oxidation conditions [50]. The native $SiO_2$ on the Si wafer seems to play an important role for the film quality.

This $SiO_2$ layer can be removed either by a physical plasma etch or by chemical etching. Removing the $SiO_2$ layer by a argon (Ar) plasma etch damages the surface of the silicon substrate and results in a rough surface. This is unwanted for thin film deposition.

Hydrofluoric acid (HF) can be used to remove native $SiO_2$ from silicon wafers chemically. HF (30%) diluted with deionised water to 25 % by volume has been used. The Si wafer was etched by exposing the wafer to the HF for a short time ("dip"), in this case 120 s. Using this diluted HF dip, the $SiO_2$ layer should be substantially removed.

Exposing a Si wafer to a HF dip which removes the $SiO_2$ layer by etching, causes poor quality NbN films as shown in figure 3.11 which shows the R-T curve of a 4 nm ultrathin NbN film deposited on a Si substrate which is exposed to a dip in diluted HF for 120 s. The other curve is the R-T curve of a 4 nm ultrathin NbN film deposited on an untreated Si substrate which shows a critical temperature $T_c$ of only 6.1 K.

Within the limits of this experiment, the native oxide layer seems to be important to get high quality NbN films. The $SiO_2$ layer may be responsible for the reduction of the lattice mismatch between the Si and the NbN.

However, no measurements to analyze the crystal structure of the sputtered NbN films, for example x-ray diffraction, have been done within this work. Therefore it is not possible to finally draw
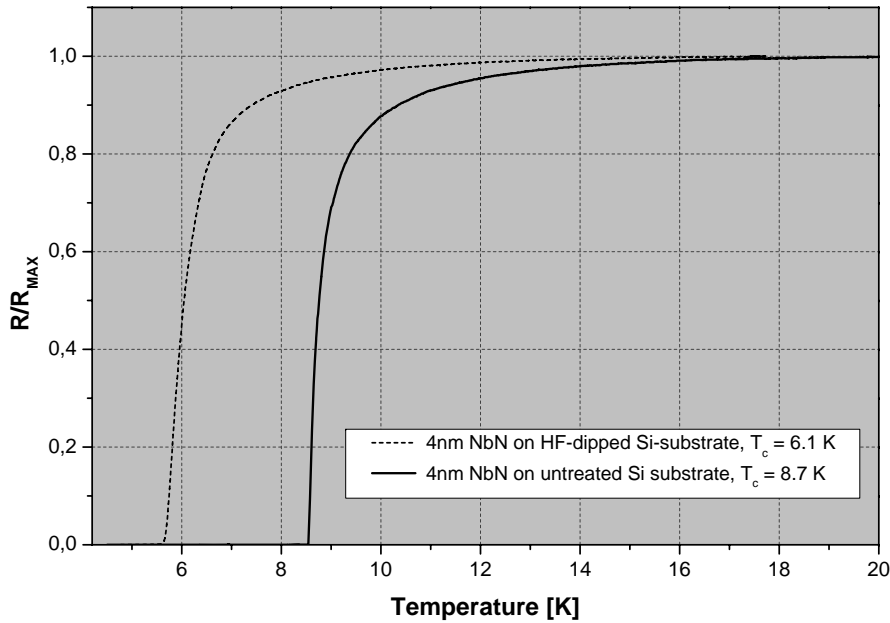
**Figure 3.11:** R-T curves of 4 nm ultrathin NbN films on Si-substrates exposed to a hydrofluoric acid dip which removes the $SiO_2$ layer by etching and on untreated Si-substrates.

a conclusion on the exact film structure. In our case, heating the substrate during deposition is essential for ultrathin NbN films.

Other important film parameters are sheet resistance $R_{sq}$ and resistivity $\rho$. The sheet resistance of the film is determined using the van der Pauw method, which is a special four-point resistance measurement described in section 3.7.1. The NbN samples are etched with $SF_6$ and Ar, defining the van der Pauw structure using the reversal photo resist AZ 5214. The current used for the van der Pauw measurement is 10 μA.

The electrical properties: sheet resistance, resistivity, and resistance ratio ($R_{300}/R_{20}$) have been measured for 5 nm ultrathin NbN films sputtered at ambient temperature, at 600°C, and at 800°C. The properties of the NbN films sputtered at these temperatures are summarized in table 3.1.

The observed resistivity values range from 430 μΩcm for films sputtered at ambient substrate temperature to 260 μΩcm at 600°C. This is within the range of the resistivity found by other groups [18].

| deposition temperature | crit. temp. $T_c$ [K] | sheet resist. $R_{sq}$ [$\Omega$] | resistivity $\rho$[$\mu\Omega$cm] | $R_{300}/R_{20}$ |
|---|---|---|---|---|
| ambient | 8.1 | 861 | 430 | 0.78 |
| 600 °C | 9.4 | 520 | 260 | 0.88 |
| 800 °C | 9.2 | 589 | 294 | 0.86 |

**Table 3.1:** Properties of 5 nm ultrathin NbN films sputtered at different substrate temperatures. This table indicates that heating the substrate during deposition is essential.

HEB devices are based on strips of NbN ultrathin films, thus the resistivity determines the length to width ratio of the HEB device for a desired resistance. The sheet resistance of a film with the resistivity $\rho$ and a thickness $t$ is defined:

$$R_S = \frac{\rho}{t} \tag{3.1}$$

The unit is Ohms, but it is referred to as Ohms per square. The resistivity of 260 $\mu\Omega$cm results in a sheet resistance $R_S$ of 580 $\Omega$ for a 5 nm ultrathin film. The normal state resistance of the HEB device should stay within the range of 100-200 $\Omega$, because the planar antennas are designed to have an impedance of 100 $\Omega$. A HEB device of 400 nm length and 2800 nm width has a resistance of 100 $\Omega$, which is exactly the antenna impedance, seen at the bolometer at the resonance frequency for the used double slot antenna. Therefore it is generally possible to fabricate HEB devices based on these NbN films.

As shown in table 3.1 all of the films had a resistance ratio ($R_{300}/R_{20}$) less than unity, indicating a nonmetallic conduction. Table 3.1 indicates that there is a correlation between resistance ratio and the critical temperature, which could also be found in previous samples.

### 3.7.5 Estimation of Film Thickness

The sputtering rate is the rate at which the material is removed from the target. The sputtering rate is proportional to the power density of the plasma at a constant total sputtering pressure. The deposition rate in reactive sputtering is a function of the sputtering rate, the distance from the target to the substrate and the total sputtering pressure.

Film thickness was measured by a mechanical stylus surface profiler (Tencor Alpha-Step 100). The resolution of the Tencor Alpha-Step 100 is 50 Å. So it is not possible to measure the thickness of a 4 nm thin film with a high accuracy directly. The relation between the sputtering time and the film thickness is assumed to be linear. Films of different thickness (> 20 nm) have been deposited and the measured thickness values were used to interpolate the sputtering time for a 4 nm thin film.
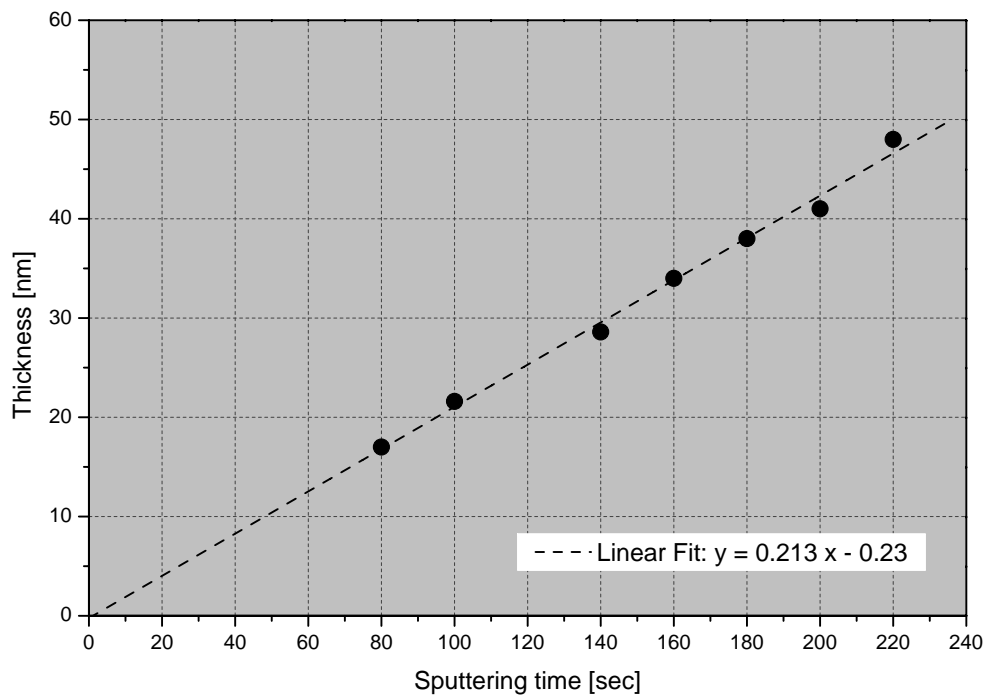


**Figure 3.12:** NbN film thickness versus sputtering time for 0.5 Pa argon partial pressure. The dotted line is a linear fit to the measured values.

The sputtering time is controlled by a shutter between the cathode and the substrate. The shutter is computer-controlled to achieve a high accuracy.

Figure 3.12 shows the film thickness versus sputtering time for the different NbN film samples ranging from 15 nm to 50 nm thickness. The NbN film thickness versus sputtering time is in good agreement with a linear behavior, so that it is indeed possible to derive a deposition rate for these particular sputtering parameters.

The slope of linear fit in figure 3.12 represents the deposition rate. The deposition rate for NbN using an argon partial pressure of 0.5 Pa, 1.6 sccm nitrogen flow rate, 81 W sputtering power and a substrate temperature of 650°C was found to be 2.1 Å/s.

The thickness at zero sputtering time is extrapolated to -0.23 nm which can be neglected within the accuracy of this experiment. For 5 nm ultrathin films, this results in a sputtering time of 25 s. This is a well controllable sputtering time.

## 3.7.6 Uniformity of the Film

In order to give a rough estimation of the large-scale uniformity of the critical temperature of the NbN ultrathin film across the wafer, a $30 \times 30$ mm$^2$ wafer was cut into three $10 \times 30$ mm$^2$ pieces after the deposition.
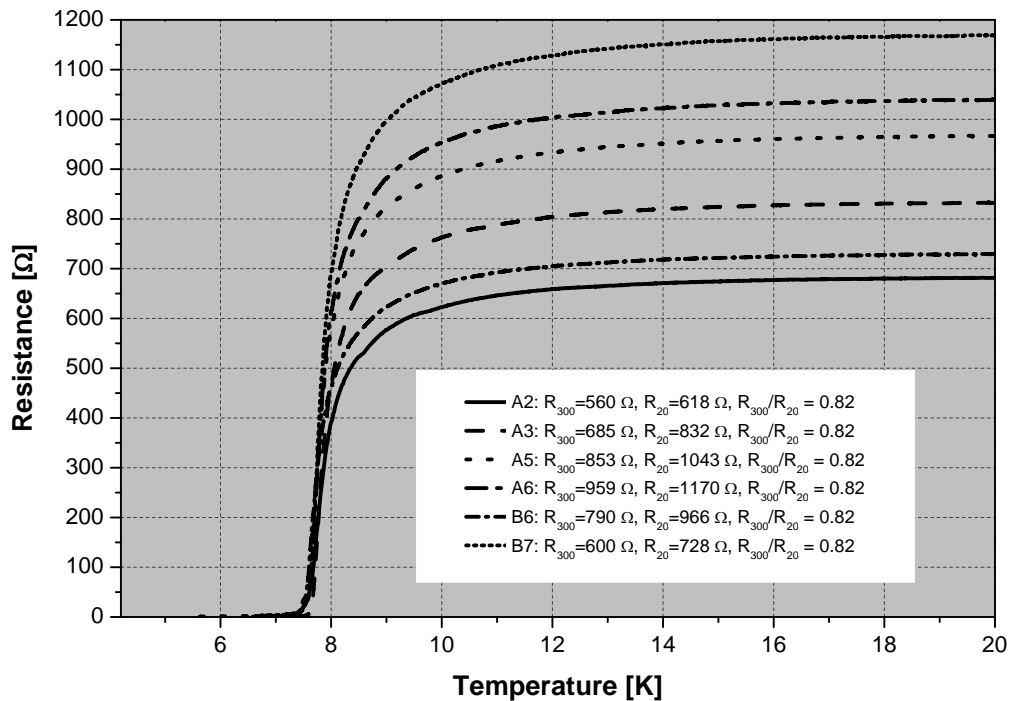


**Figure 3.13:** Resistance versus temperature of a 4 nm thin NbN film measured across a $10 \times 30$ mm large wafer. The identifiers A2-A6 and B6-B7 are contact positions on the wafer in 5 mm distance respectively.

The critical temperature was measured at positions separated by 5 mm each across the wafer slice to get an indication of the large-scale critical temperature distribution across the wafer.

Figure 3.13 shows the resistance versus temperature diagram of the 5 different position on the center part of a split wafer. The NbN film is about 4 nm thick. The identifiers A2-A6 and B6-B7 indicate contact positions on the wafer.

Although the critical temperature $T_c$ of the wafer is slightly lower than the expected $T_c$ of a 4 nm thin NbN film, figure 3.13 clearly shows that the critical temperature and the resistance ratio $R_{300}/R_{20}$ remains constant, indicating that the film thickness is very uniform across the 10×30 mm wafer. There were no alignment marks on the NbN wafer and the bond wires were connected to the NbN film by visual judgment. Therefore the resistance in this diagram varies because the four-point probe distance was different for each measurement point.

## 3.7.7  NbN films for HEB Fabrication

Based on the optimization described in the previous sections, 3-4 nm ultrathin NbN films have been fabricated. The optimized deposition conditions are listed in table 3.2

| Parameters | Value |
|---|---|
| Base pressure (ambient temp.) | $2 \cdot 10^{-8}$ mbar |
| Gas flow rates | 60 sccm Ar |
| | 1.65 sccm $N_2$ |
| Current | 300 mA |
| Power | 84 W |
| Heater temperature | 800 °C |
| Deposition rate | 2 Å/s |
| Deposition time | 20 s. |

**Table 3.2:** Optimized sputtering parameters for 3-4 nm ultrathin NbN films.

The NbN film is deposited on a 350 μm thick and 30×30 mm large high-resistivity Si wafer using the sputtering parameters shown in table 3.2.
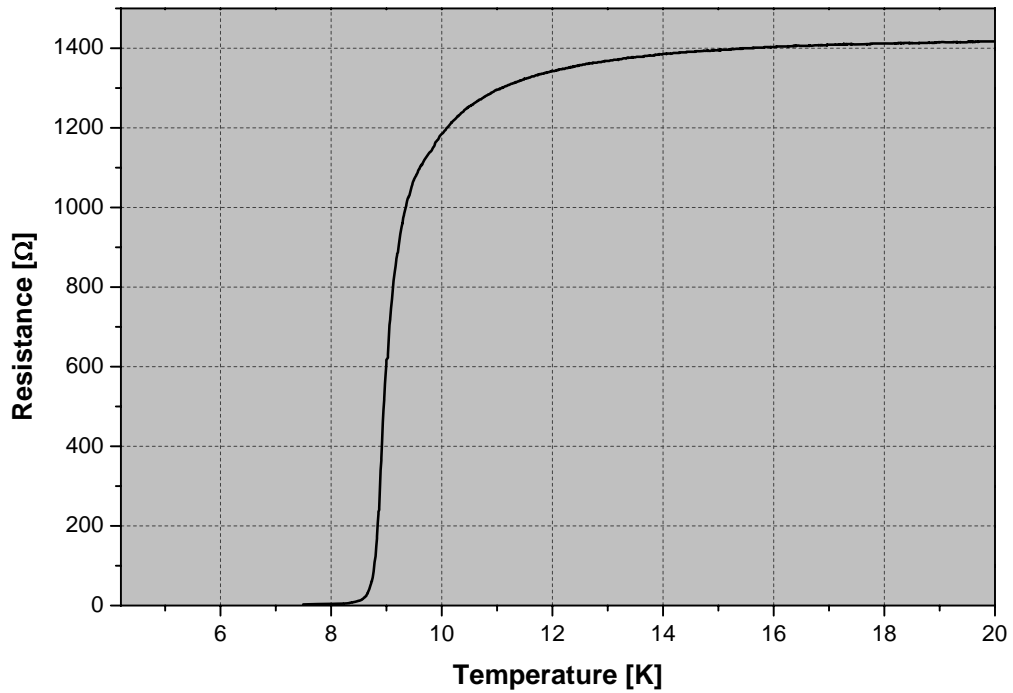
**Figure 3.14:** Resistance versus temperature curve of the NbN film used for the HEB batch [NbN-LSK FR 3 LARGE]

A roughly $2 \times 2$ mm piece is separated from the $30 \times 30$ mm Si wafer to determine the critical temperature $T_c$ and the resistance ratio $R_{300}/R_{20}$ of the NbN film before the HEB fabrication starts. Figure 3.14 shows the R-T curve of the NbN film before the actual fabrication process of the HEB batch [NbN-LSK FR 3 Large]. The NbN film has a critical temperature $T_c = 9.1$ K, a transition width $\Delta T_c = 1.9$ K and a resistance ratio $R_{300}/R_{20} = 0.85$.

# 3.8 Sputtering Parameters for Thin NbTiN Films

In this work HEB devices based on NbN and on niobium titanium nitride (NbTiN) have been fabricated. Now, the optimization of ultrathin NbTiN films is presented.

The ultrathin NbTiN films were prepared on silicon substrates by reactive DC-magnetron sputtering with a NbTi alloy target. The sputtering environment is the same one used for the ultrathin NbN films described in section 3.2.

The sputtering parameters for ultrathin NbTiN films can be determined in the same way as described in the previous section for ultrathin NbN films. The approach used for optimizing the sputtering parameters of ultrathin NbTiN films was different because the optimal sputtering parameters for thin ($>$ 100 nm) NbTiN films existed already. The thin NbTiN films were used for the superconductor-insulator-superconductor (SIS) device fabrication for the Herschel Space Observatory [51].

The parameters taken from the NbTiN film development for SIS fabrication were the argon partial pressure (0.60 Pa) and the sputtering power (about 300 W). The thin NbTiN films used for SIS fabrication were deposited in a different sputtering system. At this time the new sputtering system which was used for the NbN ultrathin film deposition did not exist. Therefore the nitrogen partial pressure had to be optimized. The films used for the SIS device fabrication were deposited on substrates at ambient temperature.

| Parameters | Value |
|---|---|
| Base pressure | $2 \cdot 10^{-8}$ mbar |
| Gas flow rates | 150 sccm Ar |
| | 8 sccm $N_2$ |
| Current | 1.2 A |
| Power | 305 W |
| Sputtering pressure | 0.63 A |
| Deposition rate | 5 Å/s |

**Table 3.3:** Sputtering parameters used for thin (300 nm) NbTiN films.

To optimize the nitrogen partial pressure 9 NbTiN films were deposited on glass substrates using different nitrogen flow rates. The

critical temperature and the resistivity of these NbTiN films were determined by the van der Pauw measurement setup described in section 3.7.1.
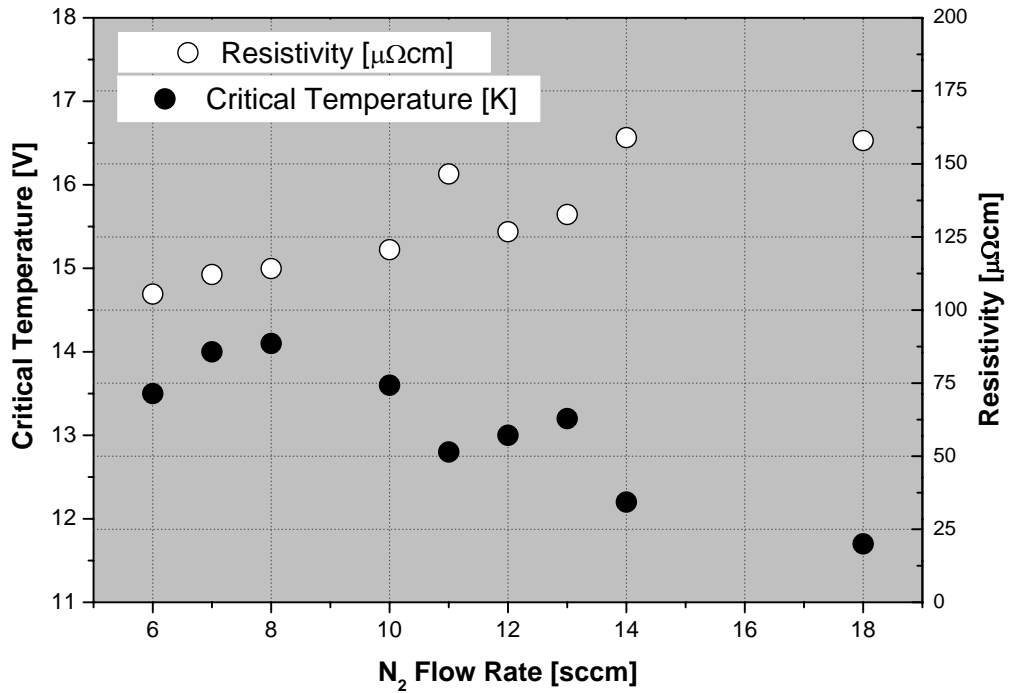


**Figure 3.15:** Critical temperature $T_c$ and resistivity of thin (about 300 nm) NbTiN films for different nitrogen flow rates

Figure 3.15 shows the critical temperature $T_c$ and the resistivity $\rho$ of the NbTiN films for different nitrogen flow rates. The thickness of these NbTiN films was about 300 nm. Glass substrates were used because for such thick NbTiN film the substrate does not influence the NbTiN film quality.

The critical temperature of the NbTiN films increases for nitrogen flow rates lower than 18 sccm ($T_c$ = 11.6 K for 18 sccm $N_2$) and reaches a maximum value of $T_c$ = 14.1 K for a nitrogen flow rate of 8 sccm as shown in figure 3.15. The values of the critical temperature for flow rates of 6 and 7 sccm indicate that the film quality gets worse for flow rates lower than 8 sccm, since the critical temperature $T_c$ decreases.

The resistivity $\rho$ of the NbTiN films deposited on glass substrates for different nitrogen flow rates is also shown in figure 3.15. The

resistivity $\rho$ decreases continuously from 158 $\mu\Omega$cm for a nitrogen flow rate of 18 sccm to 106 $\mu\Omega$cm for a nitrogen flow rate of 6 sccm.

A nitrogen flow rate of 8 sccm was chosen for further optimization because the maximum critical temperature $T_c$ was reached for this nitrogen flow rate. Table 3.3 summaries the sputtering parameters used for the deposition of 300 nm thin NbTiN films.

NbTiN films with a critical temperature $T_c$ of 14.1 K and a resistivity $\rho$ of 106 $\mu\Omega$cm have been obtained for the sputtering parameters shown in table 3.3. This critical temperature $T_c$ and this resistivity $\rho$ is approximately the same as reported by other groups [52] [53] [54].

The deposition rate of 5 Å per second was one major disadvantage of these sputtering parameters. Reducing the sputtering power to decrease the sputtering rate resulted in a deteriorated film quality of the thin NbTiN films. Using a sputtering power lower than 280 W resulted in NbTiN films with a critical temperature $T_c$ lower than 4.2 K.

Similar to the case of NbN, the nitrogen partial pressure also determines the quality of the NbTiN films, but the flow rate range which results in high-quality NbTiN is much larger than the flow rate range for ultrathin NbN films.

## 3.9 Sputtering Parameters for Ultrathin NbTiN Films

To find the optimal sputtering parameters for ultrathin NbTiN films, the sputtering parameters for thin NbTiN films were used. Starting with a 100 nm thin NbTiN film deposited on a silicon substrate, the sputtering time was reduced to deposit thinner films down to a thickness of 5 nm. Seven NbTiN films of different thicknesses were deposited on silicon substrates at ambient temperature.

The critical temperature $T_c$ was measured by using the van der Pauw method described in section 3.7.1. The red curve in figure 3.16 shows the critical temperature $T_c$ of NbTiN films deposited on Si substrates for different film thicknesses.

The critical temperature $T_c$ of NbTiN films having a thickness larger than 20 nm remains almost constant at about 13-14 K and starts to decrease for NbTiN films thinner than 20 nm. A dramatic
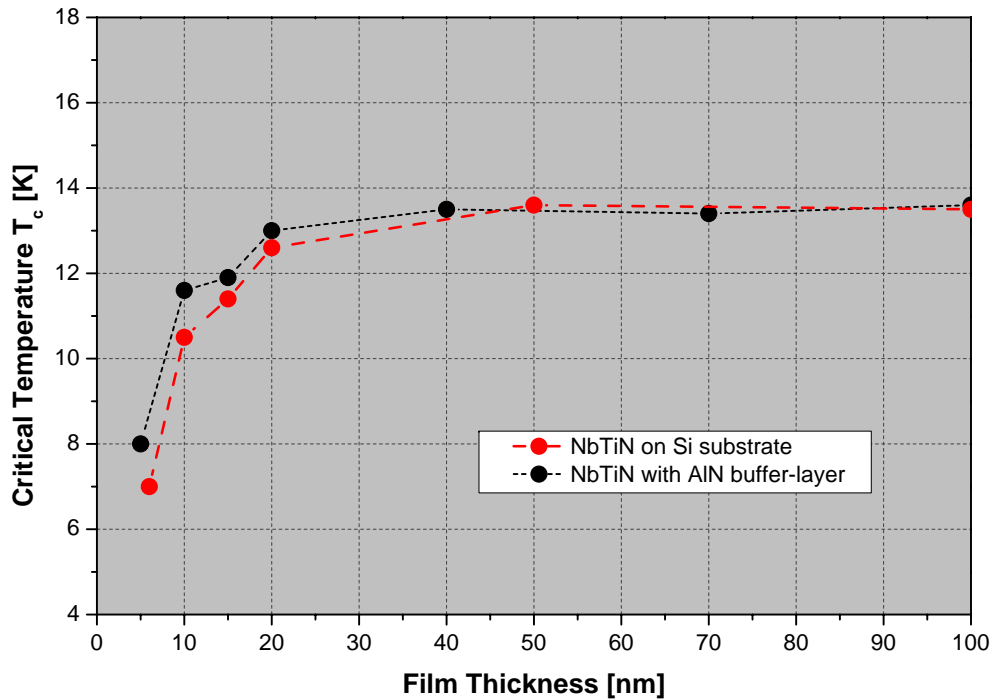
**Figure 3.16:** Critical temperature $T_c$ of NbTiN films on Silicon substrates as function of film thickness

decrease in the critical temperature $T_c$ is found for NbTiN films thinner than 10 nm. The thinnest NbTiN film on a Si substrate having a critical temperature $T_c$ higher than liquid helium (4.2 K) was found to be 6 nm. A 5 nm ultrathin NbTiN film was deposited on a Si substrate at ambient temperature, but it did not show a critical temperature above 4.2 K, therefore it is not indicated in figure 3.16.

It was not possible to deposit a 5 nm ultrathin NbTiN on a Si substrate having a critical temperature $T_c$ higher than 4.2 K at ambient substrate temperature.

### 3.9.1 Role of the Interface Layer

It has been found that an intermediate layer between the substrate and an ultrathin superconducting film can improve the quality of the superconducting film. Several materials have been already studied with respect to their properties as a buffer layer. It is well known that ultrathin *NbN* films show a large improvement in film

properties when deposited on either crystalline magnesium oxide (MgO) or on a MgO buffer layer on a Si substrate [55].

On the one hand, a buffer layer reduces the lattice mismatch between the substrate and the superconducting film which improves the superconducting film quality, but the buffer layer also affects the acoustic matching between the superconducting film and the substrate which may have an influence on the phonon escape time of the HEB device. For NbTiN there seems to be an acoustic mismatch to MgO [56].

Here, NbTiN ultrathin films on Si substrates were deposited using Aluminium Nitride (AlN) as a buffer layer. It was already shown that AlN was successfully used as buffer layer for the deposition of NbTiN for HEB devices [57]. AlN has a hexagonal close packed (hcp) structure and exhibits a lattice match with the NbTiN crystal structure.

The black curve in figure 3.16 shows the critical temperature $T_c$ of a NbTiN film deposited on an AlN buffer layer on a Si substrate. For a NbTiN film thickness larger than 20 nm, the influence of the AlN buffer layer on the critical temperature $T_c$ of the NbTiN films is not noticeable. The critical temperature $T_c$ is the same as the critical temperature $T_c$ of NbTiN films deposited on Si substrates without the buffer layer.

For ultrathin NbTiN films ($< 20$ nm) the critical temperature $T_c$ improves compared to the NbTiN films deposited on Si substrates without an AlN buffer layer. The lattice match is assumed to be the reason that the buffer layer of polycrystalline AlN increases the quality of ultrathin ($< 20$ nm) NbTiN films, since the growth of the first nanometers are promoted, after which the layer quality is nearly independent of the preceding layer.

Figure 3.17 shows the resistance versus temperature (R-T) curves of a 10 nm thin NbTiN film deposited on an AlN buffer layer and deposited on a Si substrate without an AlN buffer layer. The critical temperature $T_c$ improves by 1 K from 10.5 K for NbTiN on an Si substrate to 11.5 K for NbTiN on an AlN buffer layer.

## 3.9.2 Influence of Substrate Heating

The substrate heating at the time of the NbTiN film development was rather limited, compared to the heating system used for NbN films because an old heating system was used. Substrate heating
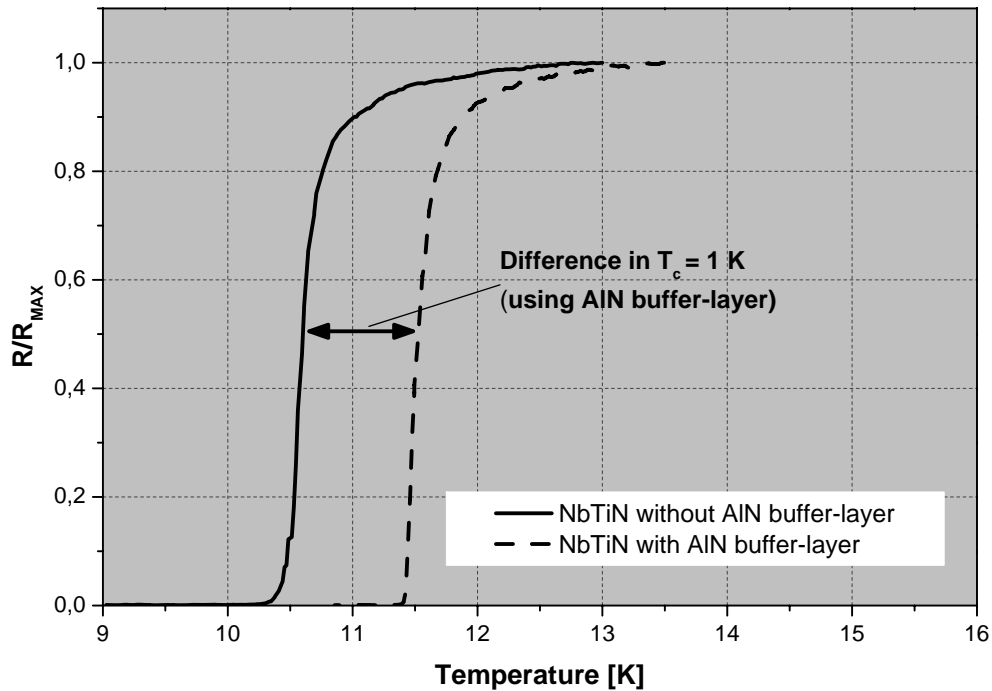
**Figure 3.17:** R-T curve for 10 nm thin NbTiN films deposited on a Si substrate and on AlN buffer layer on a Si substrate.

was achieved by a radiative quartz lamp heater below the substrate holder. The temperature of the heater could be adjusted from 0°C to 500°C. The temperature of the heater was measured by a PT-100 temperature sensor mounted a few mm above the quartz lamp.

To estimate the temperature directly on the substrate surface, a bimetal thermometer was fixed on the substrate holder and the temperature was monitored through the window of the vacuum chamber. For 500°C heater temperature the substrate surface temperature was measured to be 280°C.

Although the heating system was rather limited, a substrate temperature of roughly 280°C improved the critical temperature of a 5 nm ultrathin NbTiN film deposited on an AlN buffer layer.

Figure 3.18 shows the R-T curves of two 5 nm ultrathin NbTiN films, one deposited on an AlN buffer layer at ambient substrate temperature and one deposited on a Si substrate at 280°C substrate temperature. Compared to sputtering at ambient temperature, the critical temperature of a 5 nm ultrathin film increases
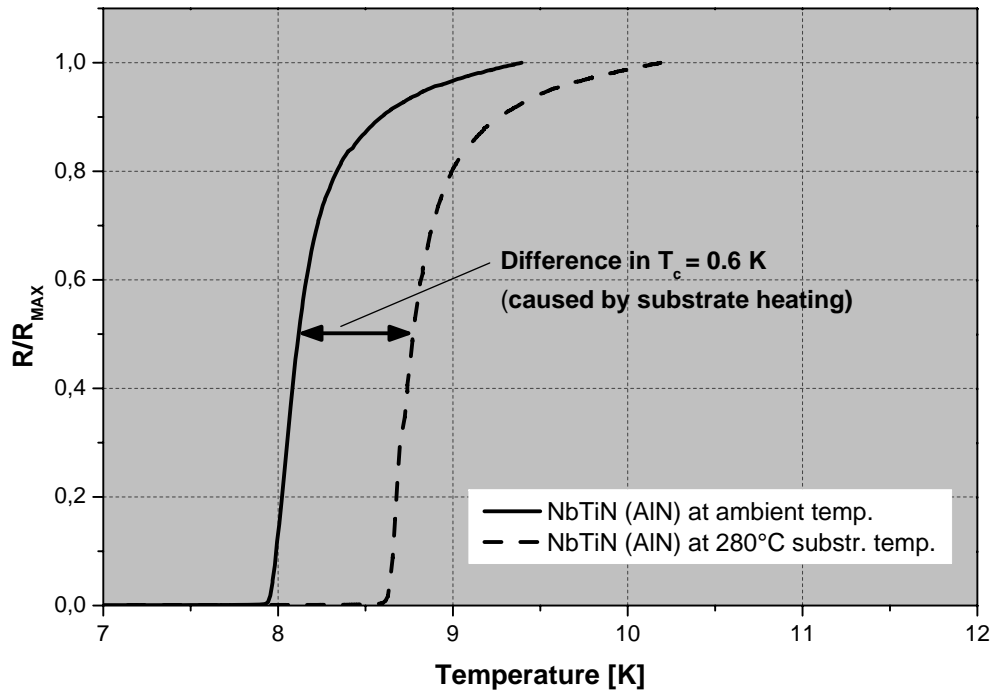
**Figure 3.18:** R-T curves for 5 nm ultrathin NbTiN films deposited on an AlN buffer layer for ambient substrate temperature and for 280°C substrate temperature.

by + 0.6 K from $T_c$ = 8.2 K at ambient temperature to $T_c$ = 8.8 K at 280°C substrate temperature. The transition width becomes slightly smaller. The resistivity is also affected by heating the substrate. The resistivity drops by about 20% from $\rho$ = 220 $\mu\Omega$cm for films deposited at ambient substrate temperature to $\rho$ = 180 $\mu\Omega$cm for a substrate temperature of 280°C.

The first generation of HEB devices was fabricated using NbTiN films with an AlN buffer layer. By using the new heating system described in section 3.7.3 it was possible to deposit 4 nm ultrathin NbTiN films on Si substrates without using an AlN buffer layer. The sputtering parameters were the same as the one used for old heating system. Thus the increased critical temperature $T_c$ is due to the elevated substrate temperature of 600°C.

Figure 3.19 shows the R-T curve of the 4 nm ultrathin NbTiN films deposited on a Si substrate at 600°C.

**Figure 3.19:** R-T curve of 4 nm a ultrathin NbTiN film deposited on a Si substrate at 600°C

## 3.10 Summary

Ultrathin NbN and NbTiN films have been deposited by reactive DC-magnetron sputtering.

Controlling the partial pressure of the reactive gas (nitrogen) is crucial for ultrathin NbN films with a critical temperature $T_c$ of about 8 K. The optimum value of the nitrogen flow rate can be obtained by depositing a few films at different points of the target voltage versus nitrogen flow rate curve. A method for a precise control of the nitrogen partial pressure by monitoring the target voltage has been introduced.

Substrate heating of 600°C is essential for the deposition of ultrathin NbN films on Si substrates. The elevated substrate temperature increases the surface mobility of the adatoms of the deposited material. Not only the heating is essential, but also the native oxide ($SiO_2$) layer on the Si substrates seems to be necessary for high-quality ultrathin NbN films.

The estimation of the thickness of the ultrathin films is an im-

portant concern. It is not possible to measure the thickness of a 5 nm ultrathin NbN film by using a profiler. Almost all groups fabricating ultrathin NbN films interpolate the thickness by measuring the deposition rate of much thicker layers ($> 20$ nm). Raman scattering and wavelength-dependent ellipsometric measurements are currently investigated for the use of the characterization and thickness measurement of ultrathin NbN films [58].

The approach of determining the optimal sputtering parameters for ultrathin NbTiN films was slightly different because the sputtering parameters for thin ($\sim 300$ nm) NbTiN films already existed. Like for NbN ultrathin films, substrate heating is essential for the deposition of ultrathin NbTiN films. Using the limited old heating system (max. operating temperature $\sim 400°$C) it was not possible to deposit 5 nm ultrathin NbTiN films on Si substrates having a critical temperature $> 4.2$ K. The use of AlN as buffer layer improved the NbTiN film quality and made it possible to deposit 5 nm ultrathin films on Si substrates with a 20 nm thick AlN buffer layer.

The replacement of the old limited heating system with a heating system based on a radiative Boralectric® heater made it possible to deposit a 4 nm ultrathin NbTiN film on a Si substrate without the use of an AlN buffer layer.

The nitrogen partial pressure is much lower (1.6 sccm) for the deposition of ultrathin NbN films compared to ultrathin NbTiN films (6 sccm). The very low nitrogen flow rate necessary for ultrathin NbN films required a mass flow controller having a maximum flow rate of 20 sccm since the accuracy depends on the maximum flow rate. The superconducting properties of ultrathin NbN films are more sensitive to changes in the nitrogen partial pressure compared to NbTiN deposition.

Basically a long term reproducibility in terms of the film quality is given by monitoring the target voltage and using a constant current regulation. The reproducibility of the NbTiN and NbN ultrathin film quality is influenced by a lot of other conditions inside the sputtering system, like impurities inside the target and the sputtering system or the target erosion.

# Chapter 4

# Device Fabrication

## 4.1  Introduction

Quasi-optical mixers at THz frequencies use dielectric lenses and planar antennas to couple the radiation from the telescope into the device, whereas in waveguide mixers, a waveguide horn followed by a waveguide and a waveguide probe is used to couple the radiation into the device.

The HEB device fabrication is different for waveguide and quasi-optical HEB devices. The planar antenna, defined by optical lithography, is directly integrated onto a dielectric substrate. This substrate is glued to the flat side of an extended hemispherical silicon lens. The substrate used here is 350 μm thick, compared to waveguide substrates which can only be a few μm thick at THz frequencies. It is not possible to handle substrates which are that thin, therefore $Si_3N_4$ on Si substrates or Si membranes are used. The unnecessary Si is removed with an etching step.

Because the chip with the HEB, integrated into a planar antenna, is relatively large (2 × 4 mm), one batch (30 × 30 mm silicon substrate) carries only 50 HEB devices, compared to some hundred HEB devices for a waveguide batch.

The actual HEB microbridge definition is the same for both waveguide and quasi-optical HEB devices. The HEB device dimensions are about 2-4 μm in width and about 0.3-0.8 μm in length. Thus, electron beam lithography (EBL) has to be used for the contact pads and the bolometer microbridge.

The actual process steps for the device fabrication are more or less standard technology for the preparation of HEB devices in con-

trast to preparing the ultrathin NbN and NbTiN films which are the most critical part in the device fabrication.

This chapter describes the sequences necessary for the HEB fabrication process, which consists of lift-off processes using patterning by optical and EBL lithography. The HEB device fabrication finishes with an etching step which removes the unnecessary parts of the sputtered superconducting ultrathin NbTiN or NbN film. A schematic outline of the different fabrication steps, as cross-section and side view, for the area of one device is shown in figure 4.6.

In the following sections, the term *wafer* or *substrate* refers to the $30 \times 30$ mm$^2$ Si substrate which is diced into 51 separate *chips* $(2.5 \times 4$ mm), each holding one HEB *device* integrated into a planar antenna. Only one wafer is processed at the time. This is called a single-wafer process. But it has become common to call this wafer process one *batch*, although a batch process usually refers to several wafers that are processed simultaneously. Here, several chips are processed simultaneously on one wafer.

## 4.2 Lithography Patterning

Lithography is a process to pattern a layer of resist on the surface of a wafer. Optical lithography uses ultraviolet (UV) radiation to expose the resist, while electron beam lithography (EBL) uses a focused electron beam to expose the resist. For optical lithography, a lithography mask containing the pattern is needed, while EBL uses the electron beam to pattern the resist directly.

In UV lithography, the object size to be patterned is limited by the diffraction limit of the used wavelength. A Karl Süss MJB3 Mask Aligner with UV 300 and UV 400 optics is used for the optical lithography process. Using this lithography system and an AZ5214E photoresist, the lithography is capable of a resolution of about 0.8 µm.

Electron beam lithography offers a much higher patterning resolution compared to optical lithography. The resolution of an EBL system is not limited by diffraction, but electron scattering and the so-called proximity effect are limiting the resolution. The resolution of the EBL system used here, which is a modified standard scanning electron microscope, is below 100 nm depending on the resist used.

Patterning the structure of the HEB microbridge and the planar antenna structure requires three different lithography steps, one optical lithography and two EBL lithography steps. The large antenna structures are patterned using optical lithography, while the very small HEB microbridge is patterned by EBL.

## 4.2.1 Antenna Patterning

In the first fabrication step, the planar antenna structure and the wiring pads are defined on the wafer which already carries the blanket deposited ultrathin NbTiN/NbN film on it.
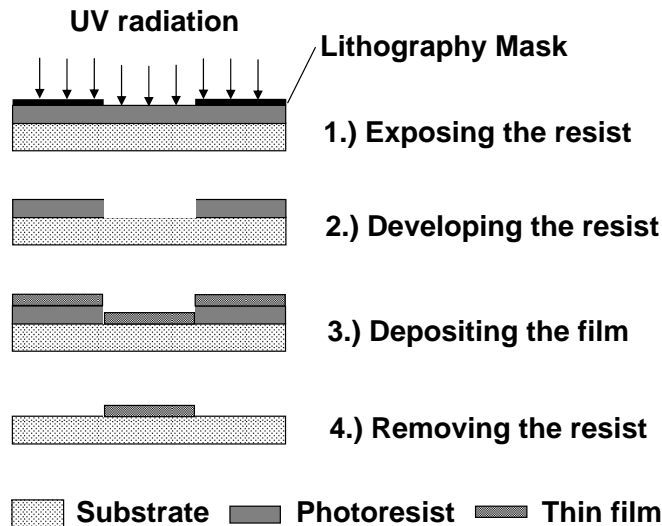


**Figure 4.1:** Schematic outline of the lift-off process

One wafer holds 51 HEB devices located in the centers of planar antennas. Two different types of antennas have been used: logarithmic-spiral antennas and double-slot antennas. The logarithmic-spiral antennas are non-resonant and are designed for a large RF bandwidth, covering a range of 0.8 THz to about 5 THz. The resonant double-slot antennas have a much better beam coupling, but are optimized for a specific frequency: 0.8 THz, 1.6 THz, 1.9 THz, 2.5 THz and 2.7 THz. The RF bandwidth of the double-slot

antennas is roughly 100-200 GHz but strongly depends on the design frequency. The relative bandwidth gets wider for higher design frequencies.

The lithography mask used for the first fabrication step, consists of 8 logarithmic-spiral antennas and 43 double-slot antennas. The antenna structure consists of a 200 nm thick gold (Au) layer. A so-called lift-off process is used to define the antenna structure and the wiring pads on the wafer.

Figure 4.1 shows the schematic outline of the lift-off process. The lift-off process is performed by using an AZ5214 image reversal photoresist. Details on working with photoresist can be found in [59]. The 200 nm Au layer is deposited by DC magnetron sputtering. During the deposition, the substrate is cooled to avoid burning the photoresist. After the deposition, the lift-off is performed in boiling acetone.

Figure 4.2 shows a microscope picture of a spiral antenna structure and a double slot antenna structure right after the lift-off process.
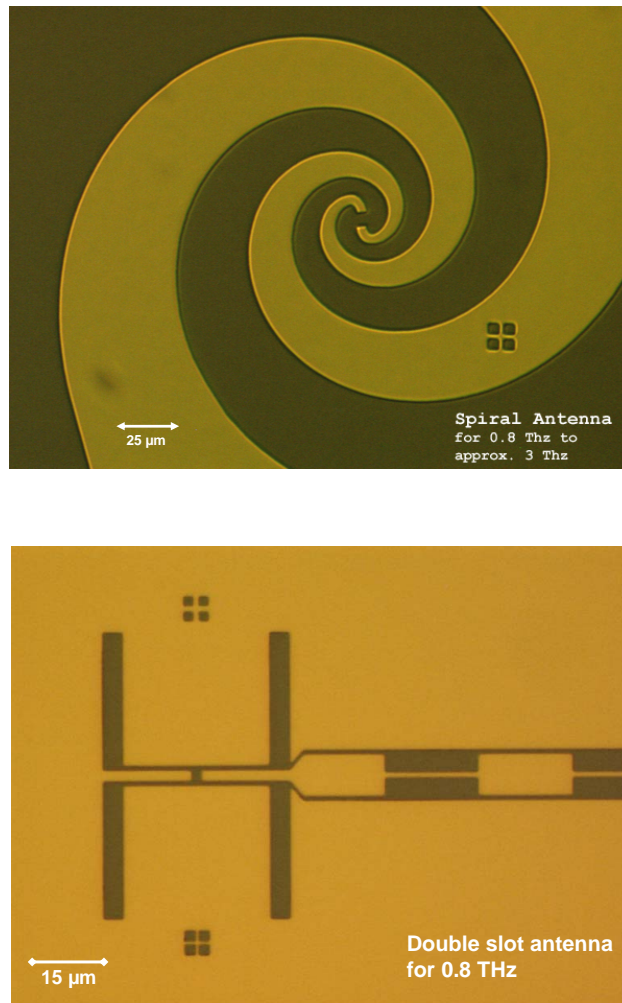
**Figure 4.2:** Microscope picture of a spiral antenna structure (top) and a double slot antenna structure (bottom) after the lift-off process. The bright features are 200 nm of gold.

## 4.2.2 Definition of the Microbridge

In the next fabrication step, the HEB microbridge between the contact pads of the Au antenna is defined. Since the length of the microbridge is below 1 μm, EBL lithography is used.

The main process parameters needed for this fabrication step are: e-beam exposure dose, the beam current, the exposure time and the development time. One major challenge which occurs in this e-beam fabrication step is the different exposure time of the double layer resist depending on layer underneath the resist. The exposure time of the double layer on 4 nm thin NbTiN/NbN on Silicon (Si) and Au layers are different, because the backscattering of the electrons is different for the different layers.

Test structures, 10 μm long strips which are half on Si and half on a Au layer, were exposed and developed to determine the process parameters for the EBL.

**1.) Spin coating of Copolymer**

150 nm PMMA
600 nm Copolymer
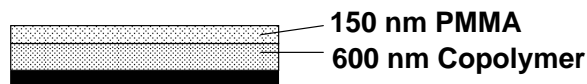
**2.) E-Beam exposure and development**

**3.) Deposition of metallization**

Deposited thin film
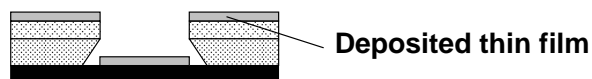
**4.) Lift-off process**

**Figure 4.3:** Schematic side view of the e-beam lift-off process using a double layer (PMMA and copolymer) resist

The definition of the microbridge starts with patterning the contact pads in the center of each chip. The distance between the pads defines the length of the HEB device, which is typically 0.3 to 0.8 μm.

Like the antenna structure, the contact pads are defined using a lift-off process. A multi-layer resist approach is used to enhance the undercut edge profile of the resist layer. As described before, the undercut profile is an advantage for the lift-off process. Also, the multi-layer resist provides resolutions greater than achievable with a thick single layer resist [60].

Figure 4.3 shows a schematic side view of the lift-off process using a double layer resist. The double layer structure consists of a polymethyl methacrylate (PMMA) layer on top of a high sensitivity copolymer resist. PMMA is commonly used as a high resolution resist for e-beam lithography. Details about the fabrication process can be found in the appendix.

A 20 nm thick aluminium (Al) layer is deposited on top of the double layer resist to provide a conducting layer. The electrons used to exposure the resist pass through the thin Al layer with little scattering.

After electron beam exposure, the Al conducting layer is chemically removed by an Al dissolver solution. The exposed parts were removed with a PMMA developer.

The 80 nm thick Au layer is deposited onto the substrate. The area of the contact pads determines the contact resistance and influences the mixing properties of the HEB device. This is described in detail in chapter 6.3.

The lift-off process is performed in boiling acetone.
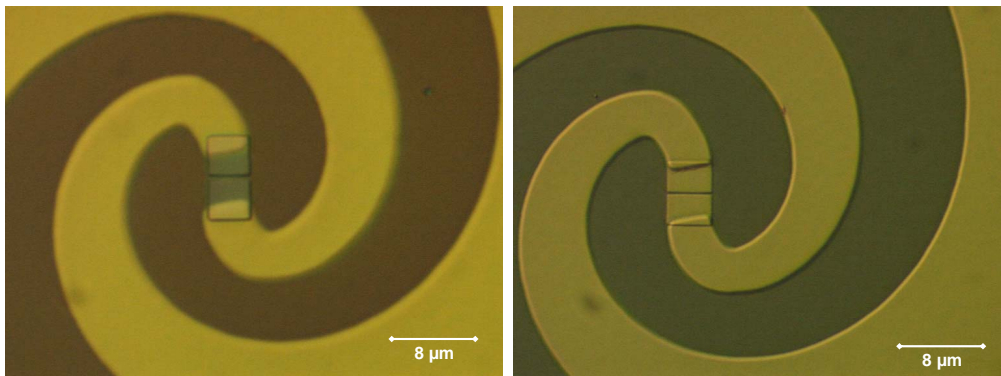


**Figure 4.4:** Optical microscope picture of a spiral antenna structure with the contact pads definition. The left picture shows the antenna structure before the contact Au is deposited onto the substrate and the right picture shows the spiral antenna after the lift-off process.

Figure 4.4 shows the optical microscope picture of a spiral antenna structure with the contact pads definition. The left picture shows the antenna structure before the contact Au is deposited onto the substrate and the right picture shows the spiral antenna after the lift-off process.

### 4.2.3 Definition of the Etching Mask

In the last lithography step the HEB microbridge width is defined. The ultrathin NbTiN/NbN still covers the whole wafer. The film has to be removed except for the area of the HEB microbridge between the Au contact pads.

Removing the ultrathin NbTiN/NbN is performed by reactive ion etching (RIE). An etching mask which covers the area of the HEB microbridge and parts of the Au contact pads is defined using e-beam lithography with a ma-N2403 negative photoresist.

## 4.3 Separation of the HEB Chips

The wafer is covered by an optical lithography photoresist to protect the HEB devices and is then diced using a wafer dicing saw. After the separation the resist is removed from the chip with acetone.

Figure 4.6 summarizes the HEB fabrication process in cross-sections and side views.

## 4.4 Summary

Phonon-cooled HEB devices for quasi-optical mixers have been successfully fabricated. The HEB devices were fabricated on high-resistivity Silicon. In order to realize the small device dimensions (about $4 \times 0.4$ μm) electron beam lithography (EBL) was used. To realize the much larger antenna structure, a conventional optical lithography fabrication step was used.

The most critical step, beside the deposition of the ultrathin superconducting film, in the fabrication of phonon-cooled HEBs is the length definition of the microbridge. A successful lift-off is the requirement for a further fabrication of the wafer. A Copolymer/PMMA double resist layer was used to ensure a good lift-off.
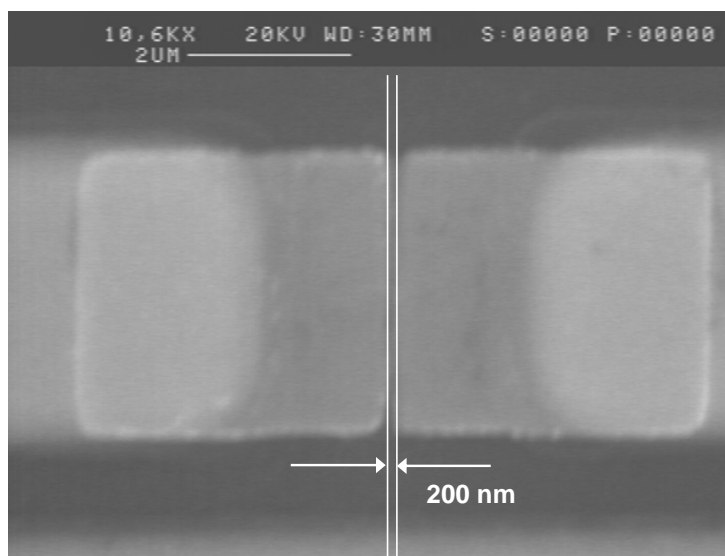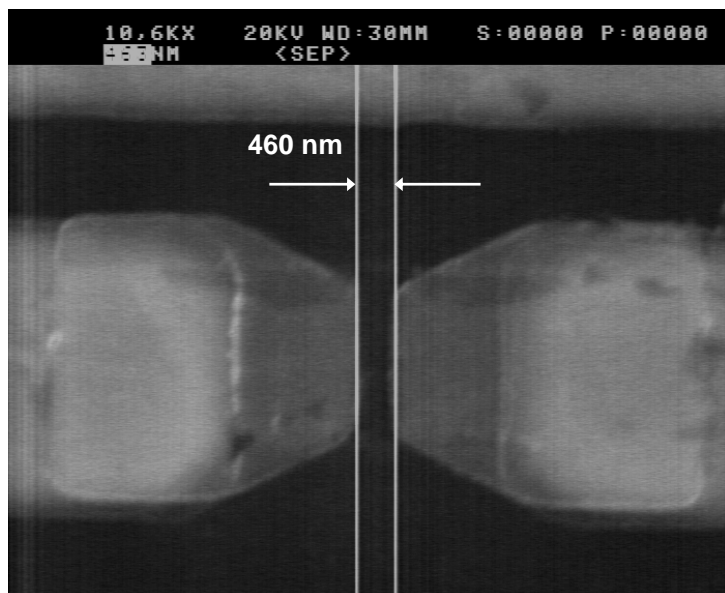
**Figure 4.5:** SEM picture of the HEB microbrigde

71

Cross section:                        Top view:

1. Substrate with NbN/NbTiN layer:

NbN/NbTiN

Si substrate

2. Definition of antenna by optical lithography :

200 nm Au
antenna
structure

3. Definition of Au contact pads by EBL (PMMA):

75 nm Au
contact pad

4. Definition of etching mask by EBL (PMMA):

PMMA

5. Creation of the actual HEB bridge by RIE:

RIE Etching
to remove
NbN/NbTiN
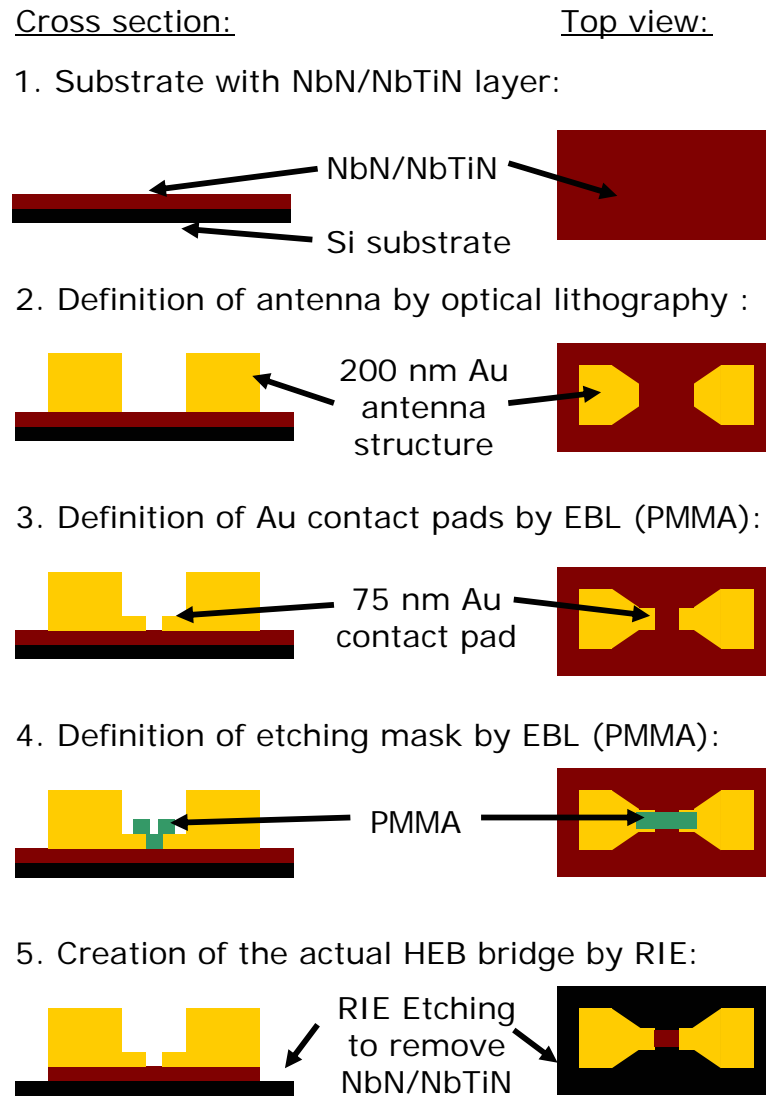
**Figure 4.6:** Schematic outline of the HEB fabrication process as cross-section and side view

# Chapter 5

# Mixer Design

## 5.1 Introduction

At millimeter (mm) and submillimeter (submm) frequencies, two distinct methods of coupling the radiation from the telescope into the mixer are commonly applied: waveguide techniques and quasi-optical methods. The quasi-optical mixers are sometimes called *open structure mixers*.

In waveguide mixers, a waveguide horn antenna is used to transform the free space wave mode coming from the telescope into a waveguide mode. The waveguide horn is attached to a mixer block where the HEB device is suspended across the waveguide and a waveguide probe is used to couple to waveguide mode into the detector.

The quasi-optical mixer uses a planar antenna on the flat side of a silicon hemispherical lens to couple the radiation coming from the telescope into the HEB device.

The mixer developed in this thesis for test measurements and for the GREAT 2.7 THz channel is a quasi-optical mixer. Its design is presented in this chapter.

## 5.2 Quasi-Optical Coupling

The two different approaches of how the radiation is coupled into the HEB device are shown in figure 5.1.

Waveguide coupling is widely used for mixers in the frequency range up to 1 THz and is currently being developed for the fre-

quency range up to 2 THz due to recent developments in micro-machining [61].

**Quasi-optic**

RF radiation

IF

HEB device

extended hemispherical
silicon lens

**waveguide**

RF radiation

IF

Waveguide mount
for HEB device

Waveguide
horn antenna
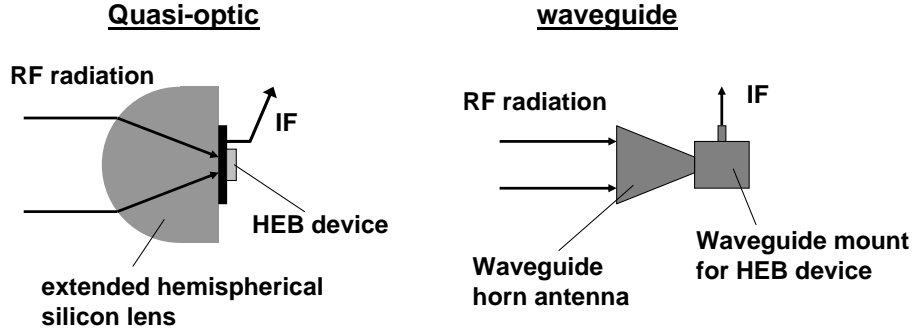
**Figure 5.1:** Schematic view of quasi-optical and waveguide system. Waveguide coupling uses a waveguide horn antenna. Quasi-optical coupling uses a planar antenna on the flat side of a silicon lens to couple the radiation from the telescope into the detector.

A waveguide consists of a hollow metallic tube that guides a propagating electromagnetic wave. The metallic tube can be rectangular, circular or elliptical in cross section. The dimension of the waveguide scales with the used wavelength band. Each waveguide has a cut-off frequency. The lowest frequency of a wave which can propagate through the waveguide is the cut-off wavelength. The cut-off frequency of a rectangular waveguide is:

$$f_{cut-off} = \frac{c}{2a} \tag{5.1}$$

where $c$ is the speed of light and $a$ is the longest dimension of the waveguide cavity. Thus, small dimensions (around 100 μm) are necessary for the THz frequency range.

Since the skin depth gets smaller for shorter wavelengths, the surface roughness of the waveguide walls becomes important. The tolerances of the waveguide together with the small dimensions make waveguide structures for THz frequencies very difficult to manufacture.

A waveguide horn antenna is used to collect the RF radiation. The directivity of an antenna is the ratio of the radiation intensity in one direction to the radiation intensity averaged over all directions. The Gaussian beam coupling efficiency or the Gaussicity is defined

as the coupling efficiency of a far-field pattern of an antenna to the far-field pattern of a Gaussian beam. A corrugated waveguide horn antenna provides an excellent Gaussian beam coupling efficiency of up to 0.98 and a well defined beam pattern.

The quasi-optical coupling is more often used at frequencies above 1 THz. A dielectric lens and a planar antenna are used to couple the radiation from the telescope into the HEB device. The HEB device is integrated into the planar antenna on a mixer chip, which is located at the back focus of lens. The dielectric lens is fabricated from the same material as the HEB substrate in order to prevent reflections at the substrate-lens interface.

One critical factor of the quasi-optical coupling is the inferior antenna efficiency compared to the waveguide method. Only a reasonable antenna efficiency of 0.92-0.94 is expected for the lens-antenna system.

## 5.2.1 Focusing Lens

A basic property of planar antennas on dielectric substrates is that the radiation is transmitted into the dielectric side and directly into the air side. For an elementary slot antenna it was found that the ratio of powers between the dielectric and air is $\epsilon_r^{3/2}$, where $\epsilon_r$ is the relative dielectric constant of the substrate [62]. This means that 97 % of the radiated power is transmitted into the substrate for Silicon ($\epsilon_r$ = 11.8), which is used as substrate material.

This involves the other problem of a planar antenna on a dielectric substrate: Planar antennas on dielectric substrate suffer from power losses due to substrate modes. Substrate modes occur, if radiation from the planar antenna at angles larger than the critical angle $\theta_c$ are totaly reflected at the substrate surface. Figure 5.2 shows a schematic view of a planar antenna on a dielectric substrate.

The unwanted substrate modes can be minimized by reducing the thickness of the dielectric substrate. For a low loss operation, the substrate thickness should be thinner than 0.04 $\lambda$ for a double slot antenna [63]. For THz frequencies the substrates have to be extremely thin (about 10 μm) and are very fragile.

An infinite thin dielectric substrate can by synthesized by a lens, made of the same material like the substrate carrying the planar antenna, which is attached to the antenna substrate [64]. Thus,
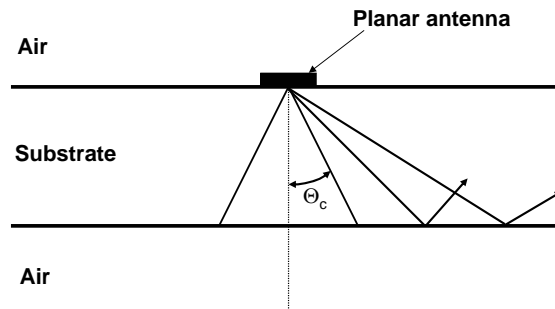
**Figure 5.2:** Planar antenna on a dielectric substrate. All the power radiated above the critical angle is trapped in the substrate and coupled to substrate modes.

this technique eliminates substrate mode losses.

Another effect of the dielectric lens is that the effective aperture of a planar antenna for THz frequencies of several mm$^2$ is increased to several cm$^2$ by placing the antenna in the focus of the dielectric lens.

The substrate lenses can be obtained commercially. The device integrated into the planar antenna can be glued to the flat side of the lens. This makes the quasi-optical approach easy to install and a low cost manufacture compared to waveguide.

**hemispherical lens**

**hyperhemispherical lens**

$\frac{R}{n}$
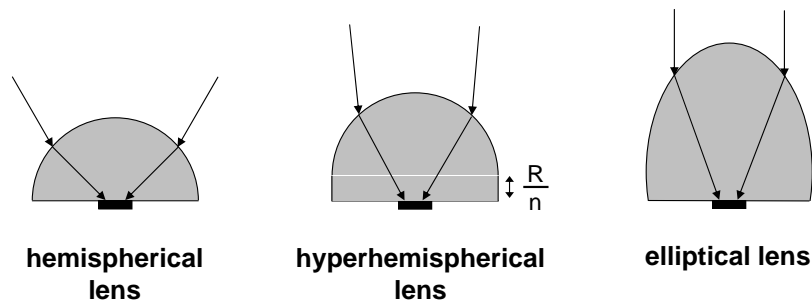
**elliptical lens**

**Figure 5.3:** Different shape of dielectric lenses

The aim of a quasi-optical lens antenna system is the coupling of the radiation from the telescope to the detector with high efficiency. Different type lenses can be used to achieve this goal.

The shape of the lens can be either elliptical, hemispherical or hyper-hemispherical. Figure 5.3 shows the different types of the dielectric lenses.

A hemispherical or extended hemispherical lens is one half of a symmetrical sphere, divided by a plane through its center. The hemispherical lens has a converging input beam. By using a extended hemispherical lens, which is a hemispherical lens with an extension length $l$, the directivity can be increased. The ratio of the extension length $l$ and the radius $R$ determines the Gaussicity and the directivity of the lens-antenna system.

A hyperhemispherical lens is a hemispherical lens with an attached cylindrical extension with a length of $R/n$, where $n$ is the refractive index of the lens material and $R$ is the radius of the lens. The hyperhemispherical lens is a approximation to an elliptical lens.

The elliptical lens is an ellipsoid divided by the plane perpendicular to the principal axis through the second geometrical focus of the ellipse. It focuses a plane wave to a point and produces a paraxial beam. The reflection loss at the lens surface of this type of lens is much higher compared to the other type of lenses [65].

For the mixer presented in this thesis, two different extended hemispherical lenses were designed: one lens with a radius of 2.5 mm and one with a radius of 5 mm. The 5 mm lens will be used for 0.8 THz, while the 2.5 mm radius lens is used for LO frequencies higher than 1.6 THz.

The extension length determines the directivity and the Gaussicity of the lens antenna system. The values of the extension length were taken from [62]. A tradeoff between directivity and Gaussicity has to be found for a selectable extension length. By choosing a extension length to radius ratio of 0.34, a Gaussicity of 93% is reached for 0.8 THz up to 88% Gaussicity for 2.7 THz. This means that the lens-antenna system is usable up to 2.7 THz. The directivity of about 32 dB is quite good.

To avoid dielectric losses at THz frequencies, the lenses have been fabricated from high resistivity Silicon material. The lenses have been produced by Sumipro Submicron Lathing BV, Almelo, Netherlands.

Figure 5.4 shows the technical drawing of the two different lenses used for the quasi-optical mixer.

**Silicon Lens Type 1:**            **Silicon Lens Type 2:**



all dimensions in mm
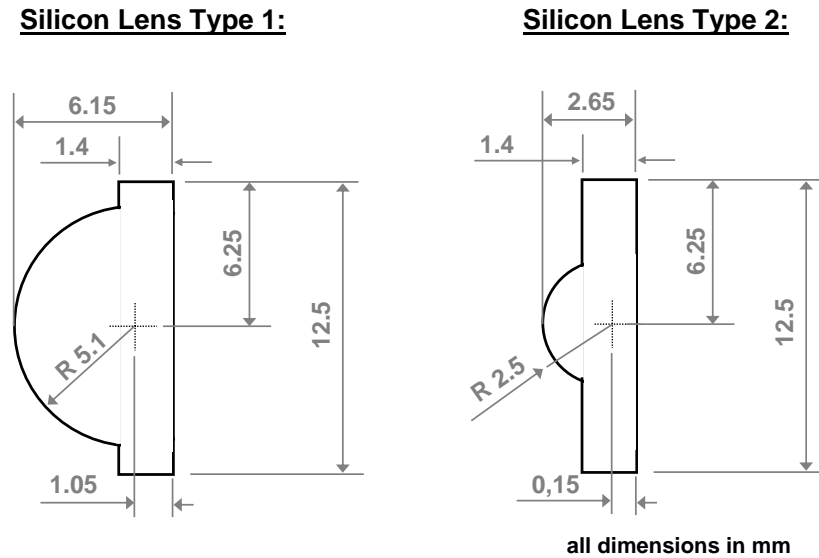
**Figure 5.4:** Technical drawing of the two different lenses. Type 1 is used for 0.8 THz and Type 2 is used for frequencies higher than 1-6 THz

## 5.2.2 Anti-Reflection Coating

Silicon shows very low absorption for radiation in the frequency range of 1-5 THz [66], but one of the major disadvantages of the silicon lens-antenna coupling is the reflection loss at the lens-air interface. An anti-reflection coating reduces the reflection loss.

The radiation propagates from vacuum ($n_0$=1.0) into silicon ($n_1$=3.42) which results in a reflection coefficient of R ~ 0.30 or ~ 30%. This reflection loss results in a 20-30% increase of the noise temperature of the receiver [67].

For a transition from vacuum to silicon the ideal index of refraction is 1.85. A material used for anti-reflection coating of Silicon lenses is Parylene, a polymer which is providing a useful combination of properties such as thermal stability, good adhesion properties and a very low permeability to moisture, chemicals, and other corrosive gases. It is possible to apply Parylene to a curved surface. Parylene has a refractive index of $n_{Parylene} = 1.639$ [68] which is close to the optimum value of $n_{opt} = 1.85$ and is therefore a good choice for the reduction of the reflection loss.

The refractive index $n_{Parylene}$ is independent for frequencies be-

tween 450 GHz and 2.8 THz for both Parylene C and D. For a single anti-reflection Parylene layer such as for silicon hemispherical lens for HEBs, the absorption loss due to the parylene layer is 2-3% [69].

Three different Parylene anti-reflection coatings are necessary:

| Frequency | Parylene layer thickness |
|---|---|
| 0.8 THz | 57.8 μm |
| 1.6 THz | 29.9 μm |
| 2.5 THz | 18.5 μm |

**Table 5.1:** Parylene layer thickness as anti-reflection coating for different frequencies

The Parylene anti-reflection coating was deposited with an accuracy of ± 0.1 μm by an external company (DiMer Beschichtungen GmbH [70]).

## 5.2.3 Planar Antennas

The HEB is integrated into the planar antenna. Two different types of planar antennas have been used: spiral antennas [71] and double slot antennas [65]. Figure 5.5 shows a layout of a spiral antenna and double slot antenna, also indicated is the position of the HEB device and the IF ports, which are used to couple the IF out of the device.

The antenna design for the planar antennas (spiral and double-slot), used for the HEB fabrication, was provided by Chalmers Institute of Technology, Göteborg, Sweden [72] within the scope of ESA ESTEC CCN8 contract on the development of novel superconducting HEB mixers and SIS mixers.

The logarithmic spiral antenna belongs to the class of frequency independent antennas [71], that means that the impedance, the radiation pattern and the polarization do not change with frequency. In practice, the spiral antenna is frequency independent only in a limited frequency range between an upper and a lower limit. This frequency limit is determined by the inner and outer radius of the spiral antenna.

The logarithmic spiral antennas, used for the HEB fabrication, were designed to cover the frequency range from 0.5 THz to 3 THz and the polarization is circular. It is a simple form of antenna
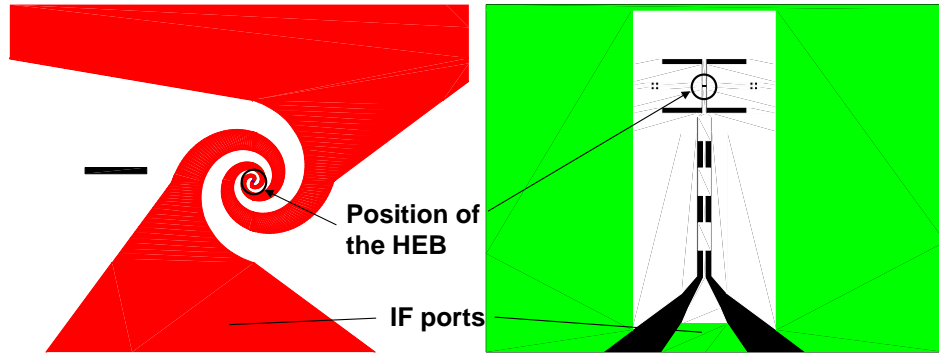
**Figure 5.5:** Schematic layout of a spiral (left) and a double slot (right) antenna. The HEB device is indicated in the picture.

because it does not need a RF filter for coupling the IF out the antenna.

The antenna impedance is purely real and can be estimated by [73]:

$$Z_{\text{antenna}} = \frac{Z_0}{\sqrt{2(1 + \epsilon)}} \tag{5.2}$$

where $Z_0$ is the characteristic impedance of free space and $\epsilon$ is the dielectric constant of the substrate material. For the Silicon substrate used for the HEB device fabrication, the impedance of the spiral antenna is found to be about 75 $\Omega$.

The spiral antenna is useful for laboratory measurement, but less suitable for the operation at a telescope, due to an inferior beam pattern compared to a double slot antenna [74].

The linear polarized double-slot antenna is not a broad-band antenna because it is a resonant antenna. Different antenna dimensions are needed for different operating frequencies of the mixer. The double-slot antennas have been designed for 0.8 THz, 1.6 THz, 1.9 THz, 2.5 THz and 2.7 THz RF frequency. Figure 5.6 shows a schematic layout of a double slot antenna and the different dimension for the different designed frequencies.

The impedance of double slot antenna for the different frequencies, seen at the bolometer is 100 $\Omega$. The RF bandwidth of the different double-slot antennas is several hundred GHz and the bandwidth increases with increasing the designed frequency.

The HEB is connected to a coplanar waveguide (CPW) transmis-
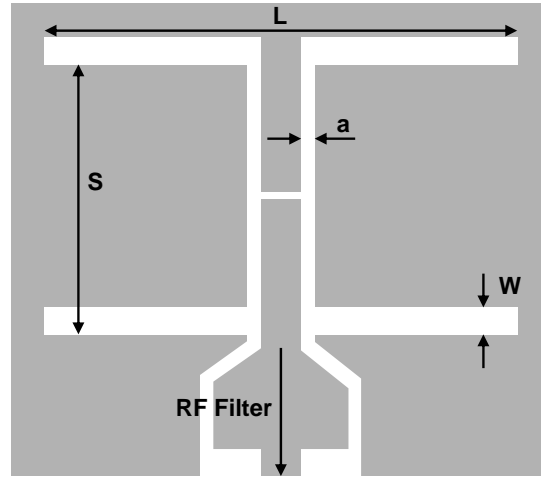
| Frequency | S | L | W | a |
|---|---|---|---|---|
| (THz) | (µm) | (µm) | (µm) | (µm) |
| 0.8 THz | 64 | 112 | 8 | 2 |
| 1.6 THz | 32 | 56 | 4 | 2 |
| 1.9 THz | 27 | 47 | 3 | 2 |
| 2.5 THz | 20 | 36 | 2.5 | 2 |
| 2.7 THz | 19.8 | 34 | 2 | 2 |

**Figure 5.6:** Dimensions of double slot antennas for different frequencies

sion line in the center of the double slot antenna, which is used to couple the IF out of the bolometer and also bias the HEB. The CPW transmission line is connected to a short circuit on one side and on the other side to a RF filter. This RF filter consisting of low and high impedance quarter-wavelength CPW lines, act as a low pass filter with short circuit for the designed RF at the slot antenna. The IF lies within the pass band of the filter.

## 5.3   Mixer Unit

The combination of the planar antenna and the Silicon lens have to be mounted in a setup that can be integrated into a cryostat to cool the bolometer to 4.2 K.
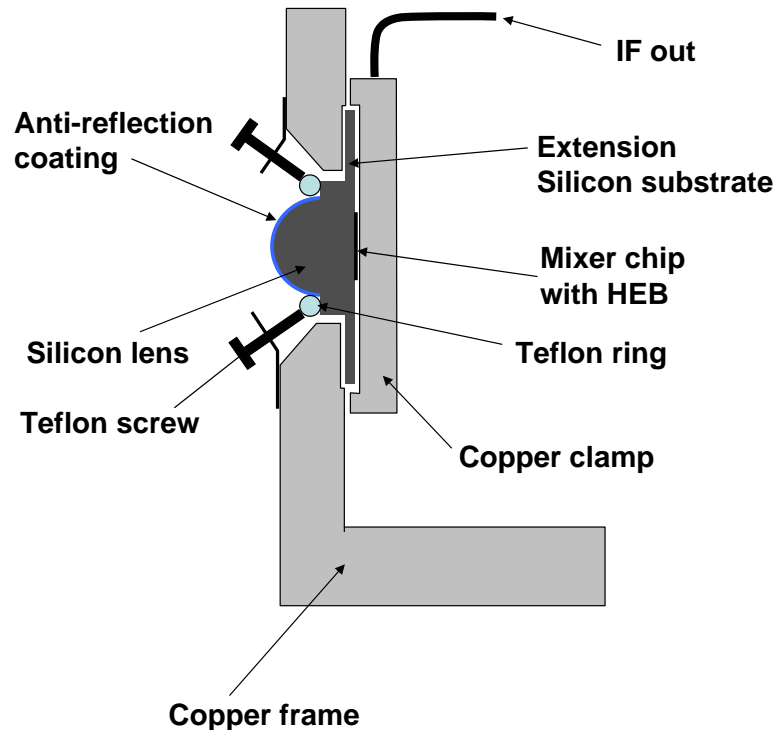
**Figure 5.7:** Schematic side view of the mixer mount.

The schematic view of the mixer unit is shown in figure 5.7. The extended hemispherical lens is mounted in the circular opening of the mixer unit. The lens is centered by using a Teflon ring and is fixed by four Teflon screws. A 350 μm thick, both side polished wafer is used as an extension layer of the lens. The chip with the HEB integrated into the planar antenna is placed on the backside of the extension wafer and is clamped by a copper clamp. The copper clamp is bolted to the mixer unit.

An SMA cable is integrated into the copper clamp to couple the IF frequency out of the HEB device. The electrical connection to the bias circuit is also made through the IF connector. The center wire of the SMA cable provides the contact to the chip, when the copper clamp is adjusted on the mixer unit. Figure 5.8 shows a optical microscope picture of the HEB chip clamped by the copper clamp. The copper clamp is connected to the ground pads of the HEB chip and is also connected to the copper screen of the SMA

cable. This provides a good ground for the IF and DC connection.

Indium foil is used to improve the electrical contact. The Indium foil is very important below the center wire of IF connection, but is also used to improve the contact between the ground plane of the HEB chip and the mixer clamp.

A very thin layer of cryogenic high vacuum grease (Apiezon N) is used at all interfaces of the silicon parts and also between the extension wafer and the mixer mount. The cryogenic vacuum grease improves the thermal contact. The grease also fills the micropores of the adjoining surfaces. With an refractive index of about 1.5 it is in any case better than the refractive index of the vacuum.
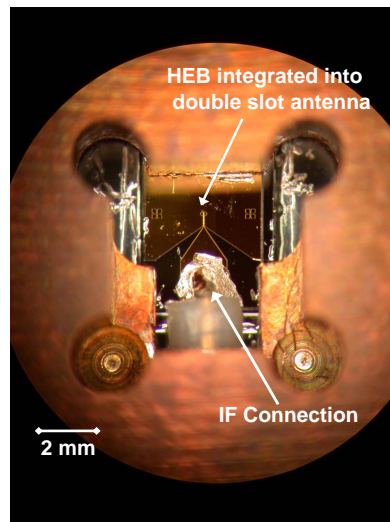


**Figure 5.8:** Microscope picture showing back side of the mixer unit. The HEB chip is clamped under the mixer clamp.

The major problem of the lens-antenna system is the exact position of the planar antenna on the flat side of the lens. An off-axis displacement of the planar antenna influences the scan angle, the directivity, the Gaussicity and the reflection loss [75].

The effects of an antenna misalignments were studied especially for cryogenic space instruments like the HIFI instrument onboard of the Herschel satellite. The alignment of the HEB chip to the lens needs to be less than 5-10 µm to avoid significant beam misalignment [76].

In this version of the mixer unit, the adjustment of the HEB chip is done by visual judgement by using the boundary of the

mixer clamp as alignment assistance. This leads to an accuracy of about 30 μm. Figure 5.8 shows a microscope picture showing the back side of the mixer unit.

This mixer unit is very useful for laboratory tests, but for the use in a telescope some improvements have to be made. An improvement planed for the next version of this mixer is the use of an IF circuit board. So, the connection between the IF circuit board and the HEB chip can be done by using wire bonding. The chip alignment can be improved by placing the HEB chip into an opening in the IF circuit board.

Figure 5.9 shows a photography of the fabricated mixer unit, as front view, side view and back view.

The mixer unit including the copper clamp, Teflon ring and Teflon screws have been fabricated in the mechanical workshop of the institute.

## 5.4   Summary

In this chapter the mixer unit including the lens-antenna system was described. The major challenge is the coupling of the radiation coming from the telescope into the mixing device. A quasi-optical lens-antenna design was used for this mixer.

Two different lenses have been designed. The extension length of the hemispherical lens was chosen to be the best trade-off between Gaussicity and directivity.

The largest coupling loss occurs on the surface of the lens. Therefore a Parylene anti-reflection coating is used to reduce the reflection loss. High resistivity Silicon is used as lens material to minimize the absorption loss inside the lens.

The mixer mount was fabricated in the workshop of the institute. The major challenge of this mixer unit is the alignment of the mixer chip. The beam pattern and the focus are very sensitive to the position of the planar antenna on the backside of the extended hemispherical lens.
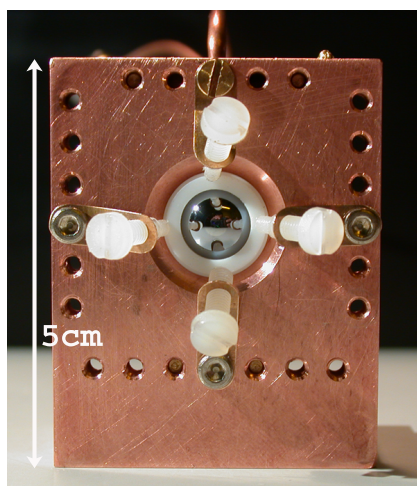
Front view
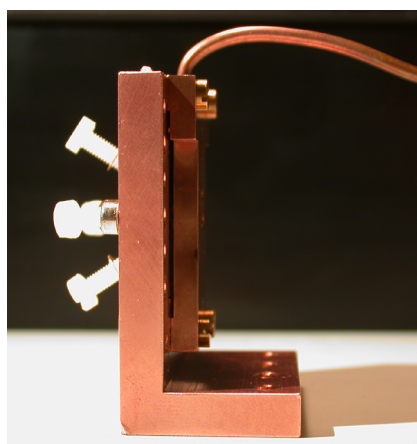
Side view
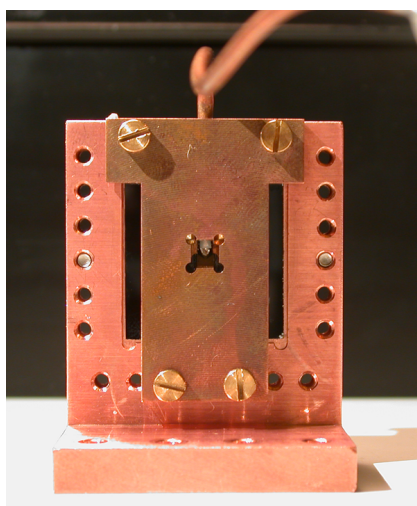
Back view

**Figure 5.9:** Photography of the mixer unit.

# Chapter 6

# DC Measurements

## 6.1 Introduction

In order the verify the fabrication process of the HEB device fabrication, direct current (DC) measurements were performed before the more complex heterodyne measurement is performed. The selection of HEB devices which will be used for the RF measurements is based on the results of the DC measurements. The HEB device chips are measured by using the dipstick measurement setup described in chapter 3.

Two different measurements were performed. First the resistance versus temperature (R-T) curve and then the current versus voltage (I-V) curve of the HEB device is measured.

The contact resistance between the contact pads and the superconducting NbTiN/NbN film have been studied. A cleaning process which improves the transparency of the interface is established. The improved interface transparency results in lower RF and IF losses and should improve the HEB sensitivity and LO requirement.

## 6.2 R-T Characteristics

The resistance versus temperature (R-T) curve of an HEB is used to determine the successful fabrication process and some characteristics of the HEB device.

The normal state resistance of the HEB device is determined by the geometry of the NbN/NbTiN microbridge. The normal state resistance equals the RF impedance of the HEB device [77]. So,

the HEB device dimensions are chosen to fit the impedance of the planar antennas. The spiral antenna has an impedance of 75 $\Omega$ and the double-slot antennas have an impedance of 100 $\Omega$.
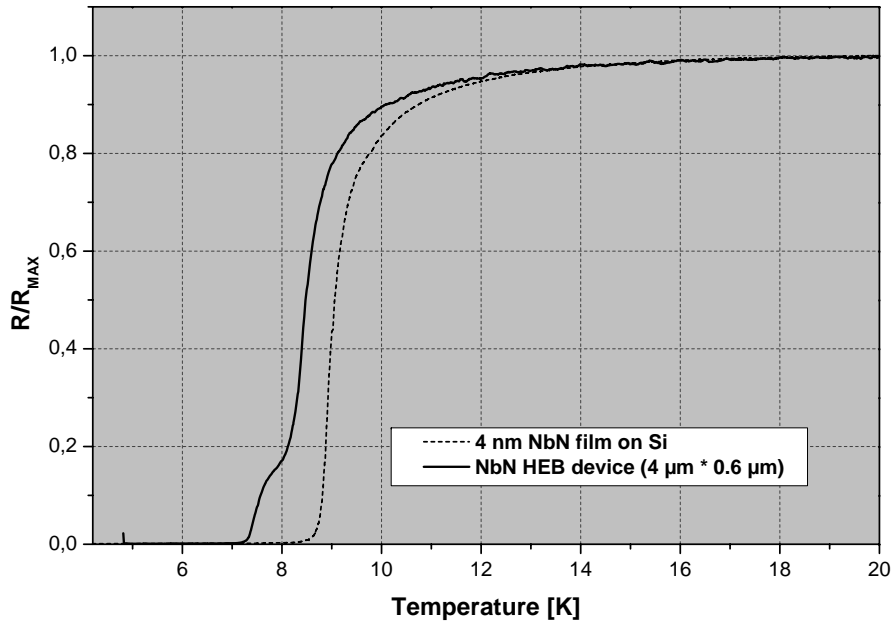


**Figure 6.1:** Resistance versus temperature (R-T) curve of a 4 nm ultrathin NbN-film before the HEB fabrication process, and the R-T curve of the fabricated NbN HEB device (NbN-LSK3-d6).

Figure 6.1 shows the R-T curve of a 4 nm ultrathin NbN-film before the HEB fabrication process and the R-T curve of the fabricated NbN HEB device (NbN-LSK3-d6). This device was used for the RF measurement in chapter 7.

The R-T curve of the NbN ultrathin film shows one resistive transition at 8.9 K, whereas two different transitions are observed for the R-T curve of the HEB device, one at 8.3 K and one at 7.3 K. The transition at the higher temperature is due to the NbN microbridge itself and the lower transition is due to the interface between the contact pads and the NbN microbridge [2] which is discussed in detail below.

The critical temperature of the HEB microbridge is lower than the critical temperature of the NbN film before the fabrication. The decrease of the critical temperature is due to the fabrication

process. The different lithography steps including the exposure baking steps (130°C) and the reactive ion etching (RIE) may change the film properties.

The R-T curve of the HEB device is an important method to verify a successful fabrication. From the experience of several HEB batches, one can say that the critical temperature of the HEB microbridge should not be more the 1 K lower than the critical temperature of the NbN film before fabrication. The R-T curve is also important for the calculation of the noise or the gain of the HEB based on models.

The transition width $\Delta T_c$ is also important to observe. Some R-T curves of different HEB fabrication batches showed an abrupt transition in contrast to the gradual decrease of the resistance towards the critical temperature observed in figure 6.1. This is an indication of an unsuccessful Gold (Au) lift-off process.

Figure 6.2 show the R-T curve of successfully fabricated HEB device and the R-T curve of an HEB device with an unsuccessful lift-off of the contact pads. For the unsuccessful lift-off of the contact pads there is still an Au layer on top of the NbN superconducting microbridge. This Au layer decreases the critical temperature of the NbN layer due to the proximity effect.
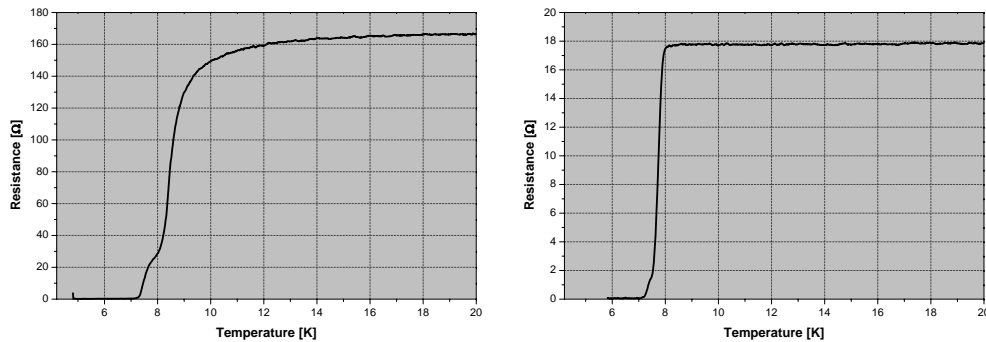


**Figure 6.2:** Example for an unsuccessful lift-off of the contact pads in the HEB fabrication. The left side shows an R-T curve of successfully fabricated HEB device, on the right side the R-T curve of an HEB device with an unsuccessful lift-off of the contact pads is shown.

For the dc current, the Au/NbN double layer behaves as a shunt circuit.

# 6.3 Contact Resistance

Figure 6.3 shows a schematic cross-sectional drawing of an HEB device. The HEB device consists of a 4-5 nm ultrathin NbTiN/NbN film, which is below the Au antenna structure due to fabrication reason. The ultrathin NbN/NbTiN film is covered with 80 nm thick contact pads and a 200 nm thick Au antenna structure.

The RF current distribution through the HEB device is also shown in figure 6.3. The RF current flows through the thick Au antenna structure and than flows from the Au contact pads into the NbN/NbTiN film within a certain distance from the bridge edge. This is because the surface impedance of the Au layer is lower than the surface impedance of the superconducting NbN/NbTiN.
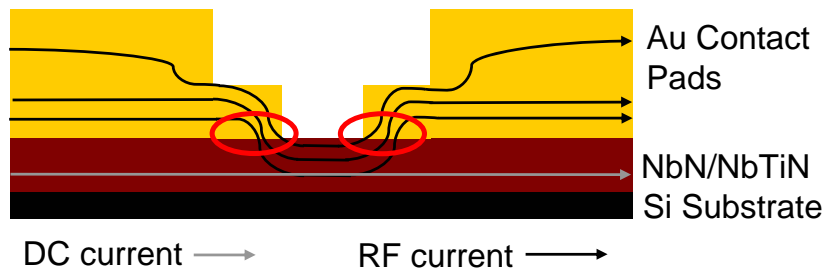


**Figure 6.3:** Schematic side view of the HEB device. The distribution of the RF and the DC currents are indicated.

The quality of interface between the contact pads and the superconducting NbN/NbTiN film is quite important for the mixer performance of the HEB device [2]. In the conventional fabrication process, there is no additional cleaning of this interface area. Native oxide and other surface contaminants of the superconducting NbN/NbTiN film result in a contact resistance between the Au contact pads and the superconducting NbN/NbTiN film.

Determining and optimizing the cleaning process before depositing the contact pads leads to a better control over the interface. The cleaning process consist of an oxygen plasma etching step, followed by an argon physical plasma etching step. The oxygen plasma etching step removes organic contaminations (like residues of PMMA resist), but causes the formation of an oxide layer on the surface of the NbN/NbTiN film. The following Argon etching step removes

the oxide layer. To restore the superconducting NbN/NbTiN film properties that might be affected by the cleaning process, a NbTiN layer (10 nm) is deposited on top of the contact area. The result is shown in R-T curve in figure 6.4
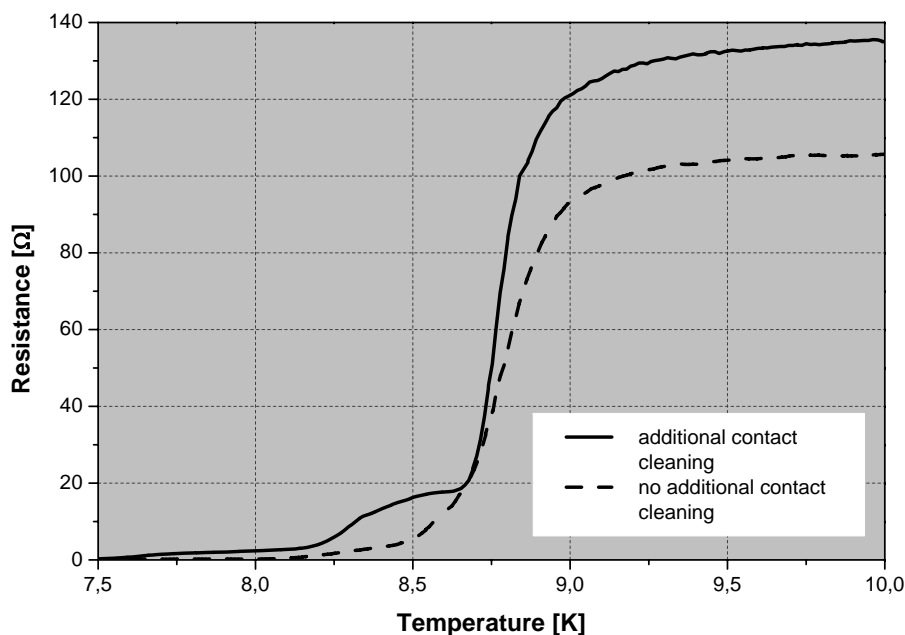


**Figure 6.4:** Resistance versus temperature curves of two devices with and without additional cleaning of the interface.

Two different superconducting transitions are observed, one due to the NbN/NbTiN microbridge itself and the lower transition due to the interface between the Au contact pads and the NbTiN/NbN bridge [78]. The parts of the bridge close to the contact pads show a reduction of the critical temperature $T_c$ associated with the superconducting proximity effect.

The superconducting proximity effect occurs at the interface of a normal- and a superconducting material. Cooper pairs from the superconductor diffuse into the normal conducting material [79]. This causes an inducement of the superconductivity into the normal conductor and also a suppression of the superconductivity in the superconductor. The strength of the proximity effect depends on the interface transparency [80].

Devices with additional cleaning show a larger resistance value at the lower transition. A higher value of resistance at the lower

transition is caused by a larger proximity effect and therefore indicates an improved interface transparency. The improved interface transparency with it the lower contact resistance results in lower RF and IF losses and should improve the HEB sensitivity and the LO power requirement. This is observed in NbN HEB devices [2].

## 6.3.1 Contact Resistance in NbTiN HEBs

Up to now this chapter described the R-T characteristics of NbN HEB devices. NbTiN was also used to fabricate HEB devices. The investigation of the contact resistance was performed on ultrathin NbTiN films since these ultrathin films were developed before the ultrathin NbN films. The influence of the contact interface on the dc characteristics of NbN HEB devices was performed by Hajenius et al. [78]. Performing the investigation of the contact resistance on NbTiN HEB device made it possible to compare the results of the contact resistance investigation of NbN and NbTiN.

To investigate more precisely the influence of cleaning the interface of NbTiN HEBs, different cleaning processes have been applied to NbTiN HEB devices.

Different cleaning processes have been applied to one NbTiN HEB batch by using a faceplate with a square opening, which covers about 85% of the wafer to protect the remaining HEB devices from the applied cleaning process. After the cleaning process, the faceplate is rotated and the next cleaning process is applied to the wafer.

Figure 6.5 shows the R-T curves of the NbTiN HEB devices with different cleaning process applied to the interface area: a "soft-clean", a "strong clean" and no additional cleaning process. The soft-clean consists of a oxygen $O_2$ plasma clean (3 W) for 6 sec, followed by an argon Ar clean (6 W) for 5 sec, the strong-clean consists of an oxygen $O_2$ plasma clean (3 W) for 6 sec, followed by an Ar clean (6 W) for 30 s. After the plasma cleaning process, a 15 nm NbTiN film is deposited into the contact area in-situ. The oxygen plasma cleaning step is primary used to remove residual e-beam resist. If the duration of the oxygen cleaning step is too long, the oxygen plasma starts to oxidize the surface of the NbTiN ultrathin film.

The critical temperature $T_c$ of the microbridge slightly differs ($\pm$ 0.5 K) for the different HEB devices across the wafer. This is
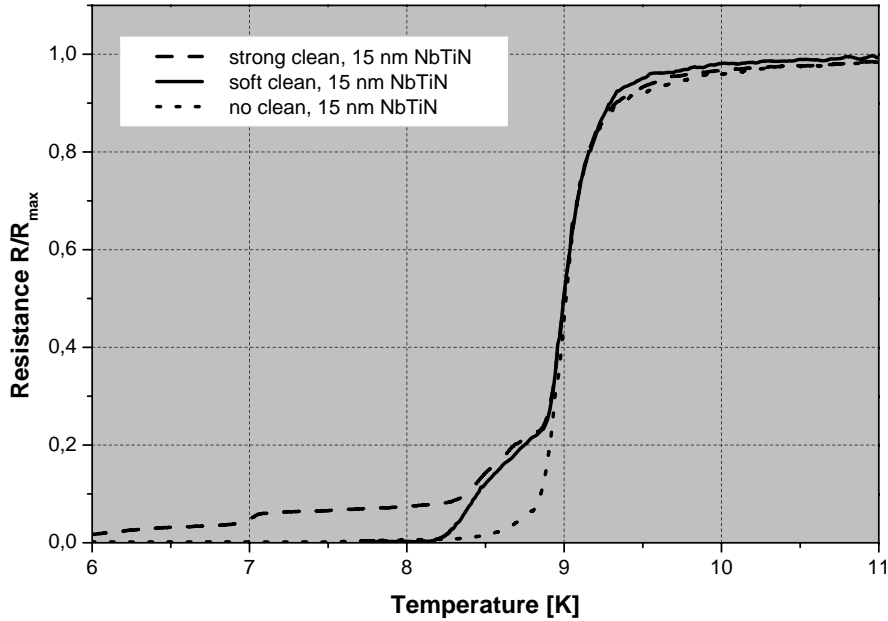
**Figure 6.5:** Resistance versus temperature curves for HEB devices with different cleaning processes applied to the interface area.

probably due to the large-scale uniformity of critical temperature of the NbTiN ultrathin film across the wafer. To compare the R-T curves for the different cleaning processes, the R-T curves were shifted in the temperature axis to the critical temperature of 9 K, which was the maximum critical temperature found for HEB devices across the wafer. The critical temperature of the microbridge should not be influenced by the cleaning process, because it is covered by a PMMA resist layer.

About 10 HEB devices were measured for each cleaning process. Figure 6.5 shows one average sample for a soft clean, a strong clean and without an additional cleaning process.

The uncleaned device shows only one superconducting transition temperature $T_c$ of 9 K, with a small "extension" from 8.8 K to 8.5 K. This extension is an indication of a proximity effect into the microbridge. The proximity effect is reduced due to the bad transparency of the interface.

The soft-cleaned device shows two superconducting transition temperatures, one at 9 K and one at 8.5 K. This indicates that the critical temperature of the contact pads and the microbridge is

different. The lower transition temperature of 8.5 K is attributed to the proximity effect of the contact pads. Since the resistance value for the lower transition temperature is much higher than for the uncleaned device, a part of the microbridge is still normal conducting due to the proximity effect. Thus, a higher resistance at the lower transition indicates a stronger proximity effect caused by an improved interface transparency .

The strong-cleaned device shows also two superconducting transition temperatures. The second transition temperature is almost the same as the one for the soft-cleaned device, but the R-T curve has a long extension with a step at 7 K. This indicates that the superconducting NbTiN film of the contact pads is substantially deteriorated by the Ar plasma etch.

These results are in good agreement with the results of Hajenius et al. [78].
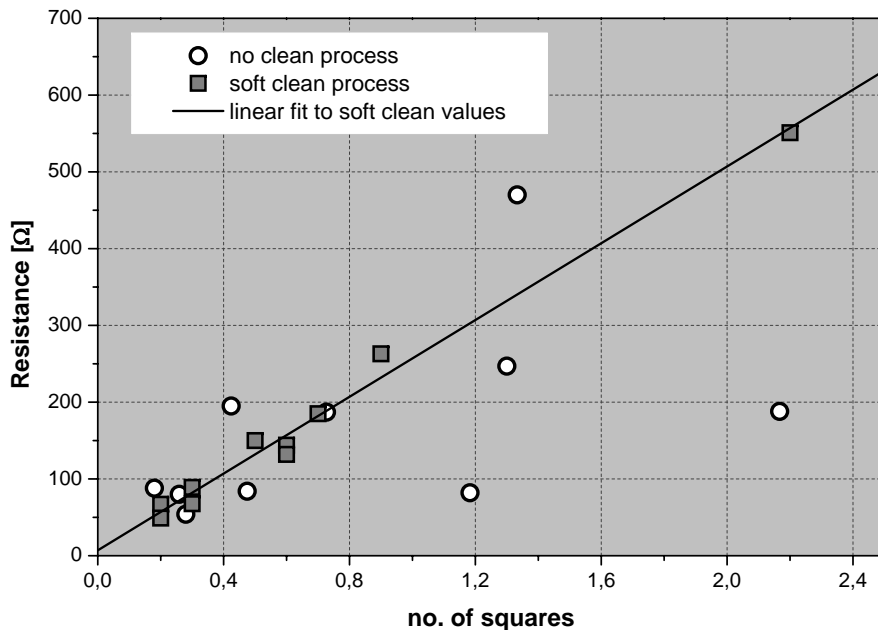


**Figure 6.6:** Resistance versus nominal bridge length (in number of squares) for devices with and without additional cleaning of the interface area.

Another result of the contact resistance analysis is the reduction in scattering of the standardized resistance of the HEB devices. Figure 6.6 shows the resistance versus bridge length in number of

squares for different HEB devices with an additional soft-clean and without an additional cleaning process. The dashed line is a linear fit to the resistance values of the cleaned devices.

Devices with additional cleaning show very little deviation from the linear behavior, while devices without contact cleaning show a significant scatter in resistance which is attributed to an uncontrolled contact resistance.

The cleaning parameters of the soft-clean were used for the fabrication of the NbTiN and NbN HEB devices.

## 6.4   R-T Characteristics of NbN and NbTiN HEB Devices.

The cleaning process was optimized and tested for the fabrication of *NbTiN* HEB devices. For the fabrication process of *NbN* HEB devices the same cleaning process was applied as for the NbTiN HEB devices fabrication.

Figure 6.7 shows the R-T curves of a NbTiN and a NbN HEB device. Both devices have similar dimension of 4.0 μm × 0.6 μm. The temperature values of the NbTiN device were shifted +0.5 K on the temperature axis in the graph to make the comparison between both devices easier.

Both HEB devices show two different transition temperatures indicating a good interface transparency. The drop-off of the resistance value for temperatures below 11 K is stronger for the NbN HEB device. This is probably due to the different superconducting materials which are used. The stronger declension was also observed for NbN ultrathin films compared to ultrathin NbTiN films.

The resistance value of the lower transition is slightly higher for the NbN HEB device. Within the limits of the resistance measurement one can say that the resistance values are equal. The extension of the lower transition is equal for both HEB devices.

If the R-T curve is used as an indicator for a successful cleaning process, one can say that the optimized cleaning process for the NbTiN HEB devices can also be used for the NbN HEB devices.
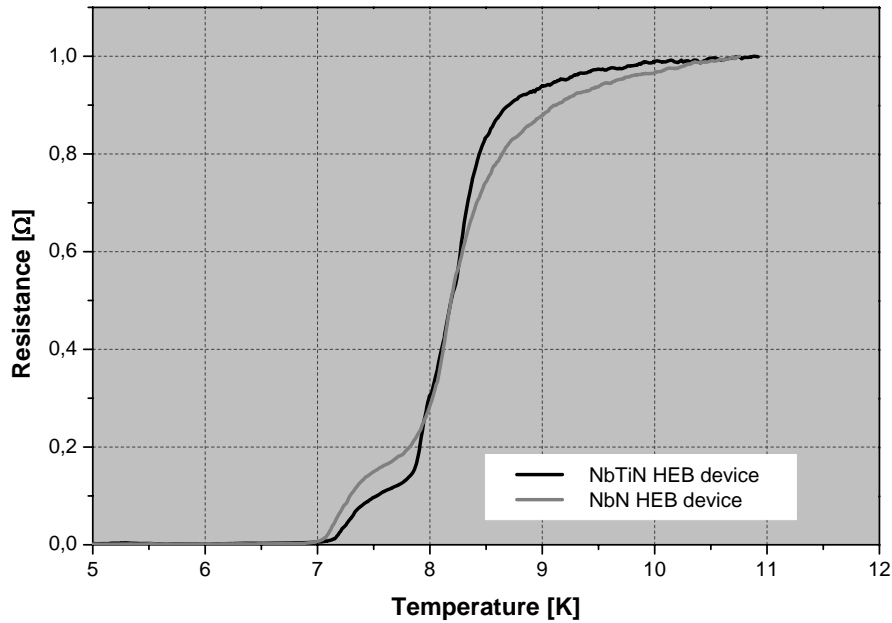
**Figure 6.7:** R-T curve of a NbTiN (NbTiN-Earth21-d6) and a NbN
(NbN-LSK3-e0) HEB device. Both devices have similar
dimensions (about 4 μm × 0.6 μm). The temperature
values of the NbTiN device were shifted by +0.5 K on
the temperature axis in the graph to make the com-
parison between both devices easier

# 6.5  I-V Characteristics

The I-V characteristics of the HEB device were measured using the
same dipstick like the one for the R-T measurement. The I-V char-
acteristics were measured at liquid Helium temperature (4.2 K).
The HEB device is connected to a bias supply. The measurement
setup is controlled by a PC.

The I-V curve of the NbN (NbN-LSK3-e0) HEB device measured
at 4.2 K is show in figure 6.8.

A hysteresis occurs in the I-V curve of all HEB devices. First
current increases from 0 μA to a current value of the critical cur-
rent $I_c$, where the microbridge remains superconducting. Thus, no
resistance occurs in the I-V curve. A further increase of the current
above the critical current causes the HEB device to become normal
conducting. This is indicated by the dashed line in figure 6.8. By
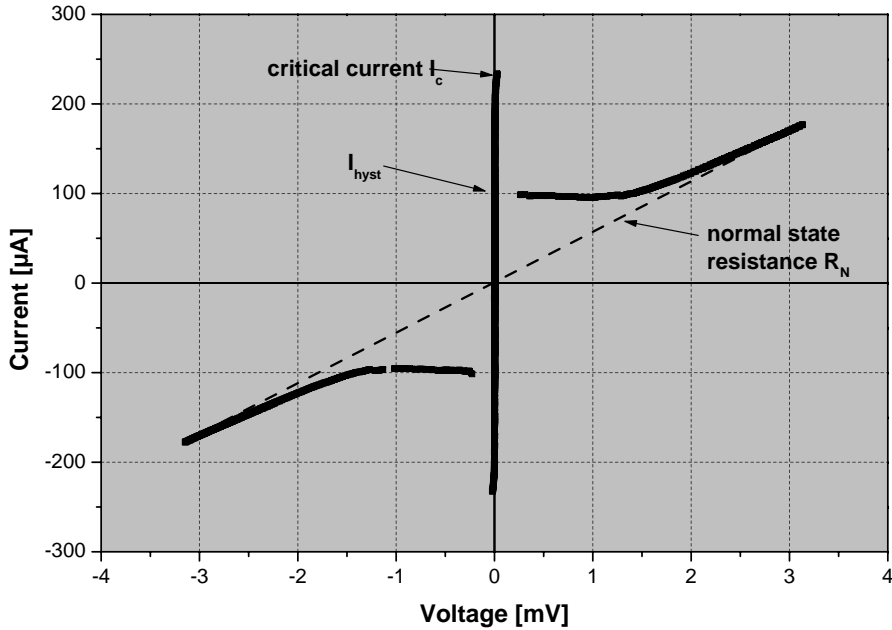
**Figure 6.8:** I-V curve of the NbN (NbN-LSK3-e0) HEB device measured at 4.2 K. The critical current $I_c$ is 232 µA.

decreasing the current, the HEB device reaches the non-linear resistive region with a significant hysteresis.

The critical current of the device is $I_c$ = 232 µA.

## 6.6  Summary

The R-T and the I-V characteristics of NbN and NbTiN HEB devices have been described. The nature of the contact determines the interface transparency between the bolometer and the contact structure. Different cleaning processes have been performed and the influence on the contact resistance have been instigated. The transparency of the interface area can be studied by investigating the R-T characteristics of the HEB devices applied to different cleaning processes.

# Chapter 7

# RF Measurements

## 7.1  Introduction

The mixer characterization described in this chapter was performed to determine the sensitivity and the bandwidth of the hot-electron bolometer (HEB) heterodyne mixer.

The standard Y-factor method was used to determine the receiver noise temperature $T_{rec}$ of the heterodyne HEB mixers based on NbTiN and NbN. By determining the intermediate frequency (IF) noise temperature and IF gain it is possible to derive the mixer noise temperature $T_{mix}$ from the measured receiver noise temperature $T_{rec}$.

The absorbed local oscillator (LO) power can be determined by using the isothermal method within the limits of this method. The results are presented and discussed in this chapter.

First, basic considerations of how to calculate the noise temperature from the Y-factor method are discussed.

The heterodyne measurements were performed at 0.8 THz LO frequency for NbTiN and NbN HEB devices at KOSMA. The NbTiN HEB devices were also measured at 1.6 THz LO at Chalmers University, Göteborg, Sweden.

## 7.2  Receiver Noise Temperature

Any receiver produces noise, even if the input port is connected to a black body load having a temperature of 0 K. In this case, the power that is measured at the output port of the receiver is entirely due to the noise generated by the receiver itself.

If a resistor at the physical temperature $T_{res}$ is connected to the input port of a noise-less receiver, it would produce the same noise power at the output port: $P = k_b T_{res} B$. The temperature $T_{res}$ of the resistor is the equivalent input noise temperature of the non-noise free receiver.

The input noise power $P_{noise}$ and the input noise temperature $T_{noise}$ of a heterodyne system can be determined by using calibrated noise sources. These noise sources are black bodies with known physical temperatures. The method is the so-called Y-factor method. Since the input noise temperature $T_{noise}$ is proportional to the input noise power $P_{noise}$

$$P_{noise} = kBT_{noise} \tag{7.1}$$

we derive the Y-factor against noise powers. k is the Boltzmann constant and B the bandwidth in equation 7.1

The output power $P_{out}$ of a receiver is linearly proportional to the incident power on the receiver:

$$P_{out} = (P_{rec} + P_{in}) \cdot G \tag{7.2}$$

where $P_{in}$ is the incident power on the receiver in the bandwidth B, $P_{rec}$ is the receiver input noise power and G is the receiver gain.

The Y-factor is the ratio of two different noise power levels, one cold temperature source and one hot temperature source. If a cold and a hot noise source ($P_{cold}$ and $P_{hot}$) are applied to the system, the corresponding output powers are:

$$P_{out,hot} = (P_{rec} + P_{in,hot}) \cdot G \tag{7.3}$$
$$P_{out,cold} = (P_{rec} + P_{in,cold}) \cdot G \tag{7.4}$$

From the measured power ratio

$$Y = \frac{P_{out,hot}}{P_{out,cold}} \tag{7.5}$$

it is possible to determine the equivalent receiver input noise power

$$P_{rec} = \frac{P_{in,hot} - Y\, P_{in,cold}}{Y - 1} \tag{7.6}$$

The hot and cold loads are a room temperature (295 K) and a liquid nitrogen temperature (77 K) black body used as a signal source.

The thermal noise power radiated in a bandwidth B by a black body at physical temperature T can be calculated from the Planck's law of black body radiation:

$$P_{\mathrm{Planck}} = kTB \left( \frac{\frac{hf}{kT}}{e^{\frac{hf}{kT}} - 1} \right) \tag{7.7}$$

where $h$ is the Planck constant, $k$ the Boltzmann constant and $f$ is the frequency. In the limit of small $hf/kT$, the term in the exponential becomes small. This gives the Rayleigh-Jeans law, which assumes that the noise temperature of a load is proportional to its physical temperature:

$$P_{\mathrm{Rayleigh-Jeans}} = kTB \tag{7.8}$$

However, for high frequencies and low temperature the equivalent noise temperature of the calibrated black body loads is not equal to its physical temperature. There is another noise term which is not included by the Planck's law and the Rayleigh-Jeans law. The zero-point vacuum fluctuation noise which must be added to the Planck formula, is given by the Callen & Welton radiation law [81]:

$$P_{\mathrm{Callen\&Welton}} = kTB \left( \frac{\frac{hf}{kT}}{e^{\frac{hf}{kT}} - 1} \right) + \frac{hfB}{2} \tag{7.9}$$

The Callen & Welton law is simply the Planck law with an additional half photon per unit of bandwidth.

The noise temperature T of a receiver is defined by equation 7.1 and can be derived form the noise power P in a bandwidth B as:

$$T_{\mathrm{Planck}} \quad = T \left( \frac{\frac{hf}{kT}}{e^{\frac{hf}{kT}} - 1} \right) \tag{7.10}$$

$$T_{\mathrm{Callen\&Welton}} \quad = T \left( \frac{\frac{hf}{kT}}{e^{\frac{hf}{kT}} - 1} \right) + \frac{hf}{2k} \tag{7.11}$$

Figure 7.1 shows the noise power versus physical temperature calculated at a frequency of 1 THz according to the Planck, Callen and Welton and Rayleigh-Jeans law. The Rayleigh-Jeans converges to the Callen and Welton law for large temperatures. The Planck law remains one half photon below the Callen and Welton law. At 1 THz the difference between the physical temperature and the Callen and Welton noise temperature of a black body at 77 K is 2.48 K and for 293 K the difference is 0.68 K.
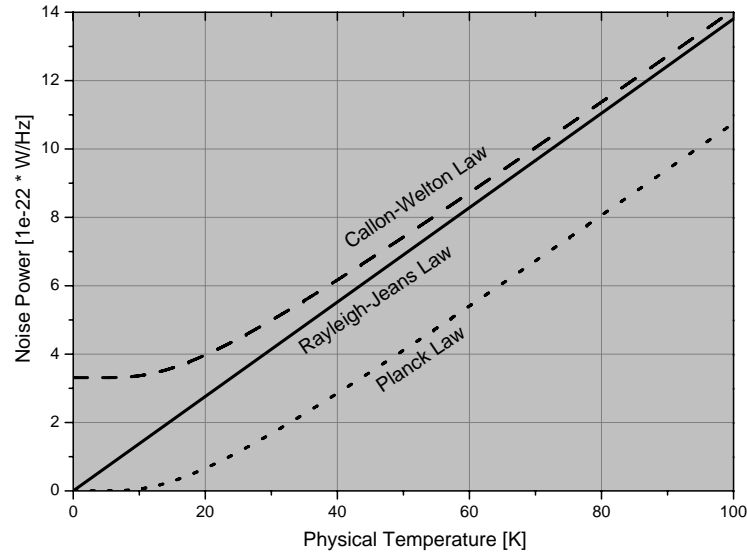
**Figure 7.1:** Noise power versus physical temperature calculated at 1 THz according to the Planck, Callen and Welton and Rayleigh-Jeans Law

So in the THz region it becomes important to use the Callen and Welton law to calculate the receiver noise temperature:

$$T_{rec} = \frac{T_{CW}(293K) - Y\, T_{CW}(77K)}{Y - 1} \qquad (7.12)$$

Equation 7.12 is valid for receivers operating single side band (SSB) and double side band (DSB) mode. The different operating modes of mixer receivers are discussed in chapter (X).

Not only the receiver noise temperature $T_{rec}$ is important in order to characterize the HEB mixer, but also the system noise temperature $T_{sys}$, the mixer noise temperature $T_{mix}$ and the IF amplifier noise $T_{IF}$. Figure 7.2 demonstrates the difference between the different noise temperatures.

The receiver noise temperature $T_{rec}$ includes the intermediate frequency (IF) amplifier noise, the mixer noise and the noise which is generated by the optics. In the system noise temperature $T_{sys}$ the noise power of the the source ($R_{source}$) is also included. In other words, the receiver noise temperature is assumed to be defined at the receiver input, and the system noise temperature is assumed to be defined at the antenna terminals.

The mixer noise temperature $T_{mix}$ is generated inside the HEB at radio frequency (RF) and IF part. The IF amplifier noise temperature $T_{IF}$ includes the noise generated inside the IF amplifier chain.
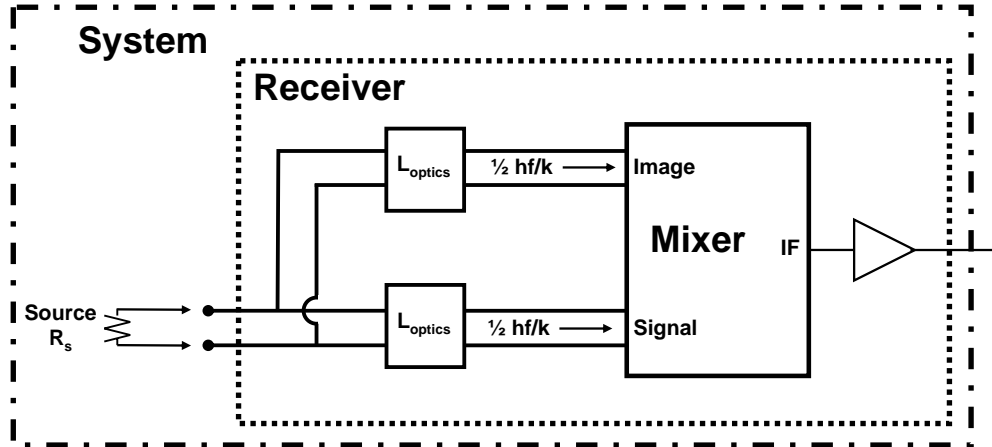


**Figure 7.2:** Definition of System, Receiver and Mixer.

# 7.3 Experimental Setup

In this heterodyne system which is used to characterize the HEB mixer, the LO radiation and the signal radiation are superimposed by a beam splitter. The superimposition of the LO and the signal takes place a ambient temperature. The heterodyne HEB mixer is placed inside a cryostat. The actual mixing process, the down conversion of the RF signal to the lower IF signal, takes place at temperature of 4 K, because the device requires to be in the super-conducting state. The experimental setup for the noise temperature measurement at 0.8 THz is presented in figure 7.3.

The Local Oscillator (LO) is a Gunn-Oscillator, followed by a frequency doubler, followed by a frequency tripler, resulting in an LO-frequency of 804 GHz and an maximum output power of 112 µW.

In order to adjust the output power of the LO a polarizing wire grid was placed in the beam path of the LO to attenuate the LO power.

The LO radiation and the signal radiation are combined by a 12 µm thick Mylar beam splitter. The 12 µm Mylar beam splitter has a signal transmission of 92 % at 804 GHz. That means that only 8 % of the available LO power is used to pump the HEB device, because only that amount of the LO radiation is reflected by the beam splitter. It is only possible to use a beam splitter if sufficient LO power is available. Otherwise it would be necessary to use a different way to combine the LO and the signal. A Martin-Puplett interferometer can be used which has a transmission of up to 99 % for both LO and signal radiation.

The combined signal is transmitted by the window of the cryostat and focused on the beam waist produced by the lens antenna combination. Teflon windows are used for the 300 K vacuum cryostat window and the 77 K heat shield. The Teflon vacuum window is 0.52 mm thick and the Teflon at the 77 K shield is 0.3 mm thick.

A window with two layers of Zitex G [82] is embedded into the 4 K heat shield. Zitex G is a sintered Teflon material with acts as a effective blocking filter for infrared (IR) radiation, with less the 1 % transmission for radiation of 1-50 µm wavelength Teflon is also an IR blocking filter, but transmits power in the 5-10 µm wavelength range [83]. Also Teflon is more robust than the Zitex material, wherefore it is used for the cryostat window.
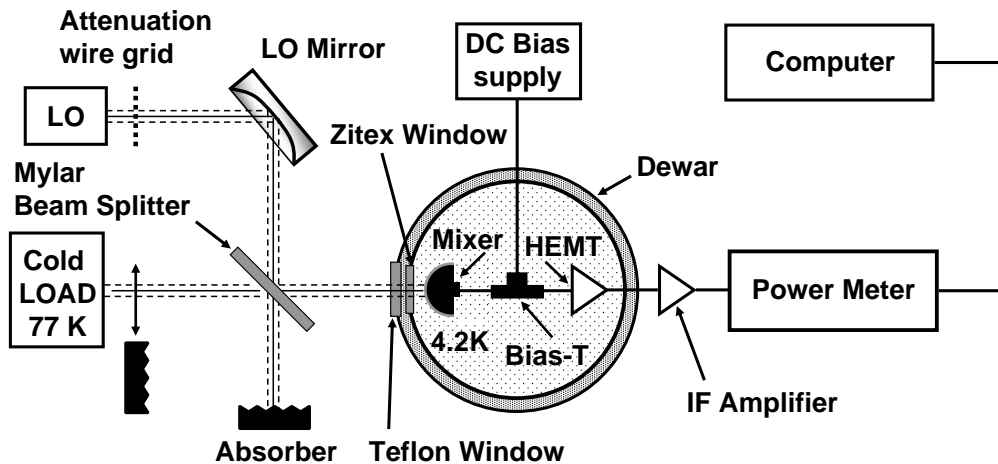


**Figure 7.3:** Schematic view of the experimental setup for the noise temperature measurement at 0.8 THz.

The HEB mixer is bolted to the 4.2 K cold plate of an Infrared

Laboratories liquid Helium (LHe) cryostat. The mixer output is connected to a low noise cryogenic 1 - 2 GHz high-electron mobility transistor (HEMT) amplifier (LNA) through a bias-T and an 1.2 - 1.8 GHz isolator by a semi-rigid coaxial cable. The LNA, the bias-T and the isolator are all mounted on the same cold plate.

The isolator is used because the HEB IF output impedance and the input impedance of the LNA do not perfectly match. The power reflected by the LNA is detected by the HEB since the HEB is a power detector and further more the reflected power influences the bias regime of the HEB. The isolator is used to suppress the reflections at the LNA caused by the impedance mismatch. The HEB device dimension determines the HEB impedance. The nominal length and width of the active HEB area are not perfectly reached during the fabrication. Also the chosen bias point influences the impedance of the HEB.

After a second amplifier at room temperature, the IF signal is connected to a 80 MHz wide tunable bandpass filter. The output power is measured by a calibrated power meter.

Figure 7.4 shows a picture taken of the experimental setup of the noise temperature measurement. Figure 7.5 shows the 4 K cold plate of the cryostat.

## 7.4 NbN and NbTiN HEB Devices

For the operation of a heterodyne HEB mixer the HEB device has to be DC-biased. The optimal bias point and the optimal LO power required for a HEB mixer are chosen to maximize the sensitivity, that means to minimize the noise temperature. For HEB mixers it has been established that the optimal LO power condition is found when the hysteresis in I-V curve just disappears, if LO power is applied to the mixer [84].

The HEB mixers used for the heterodyne measurement were NbN and NbTiN HEB mixers. Both HEB devices are integrated into a spiral antenna. Table 7.1 summarizes the properties of the two HEB devices used for the receiver noise temperature measurements.

The critical temperature $T_c$ of both devices is similar. The device size quoted in table 7.1 is the nominal device size, defined by electron beam lithography process. The real size of the device may have a difference of 10-15% in length and width compared to the nom-
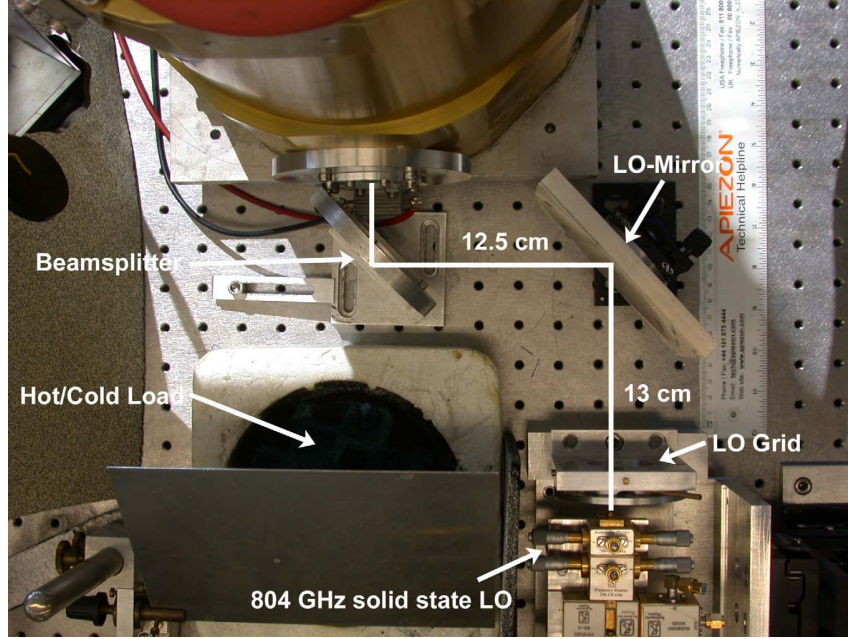
**Figure 7.4:** Picture of the experimental setup of the noise temperature measurement at 0.8 THz.

inal values. The sheet resistance of the NbTiN film is lower than that of the NbN film. In order to ensure a good antenna impedance (70 $\Omega$ for the spiral antennas and 100 $\Omega$ for the double slot antennas) matching, the length to width ratio has to be different for NbN and NbTiN HEB devices.

The volume of the NbTiN HEB is much smaller than the volume of the NbN HEB. Due to the lack of sufficient LO power at the time of the NbTiN HEB device fabrication, the size of the device was adjusted to the available LO power. Using the following noise temperature measurements it is not possible to compare the properties

| Device Name | Material | HEB size [μm × μm] | Crit. Temp. [K] | Resistance at 300K [$\Omega$] |
|---|---|---|---|---|
| Earth26-d6 | NbTiN | 2.8 × 0.5 | 8.3 | 38 |
| LSK-FR3-d6 | NbN | 4.0 × 0.6 | 8.5 | 145 |

**Table 7.1:** Properties of both HEB devices used for the receiver noise temperature
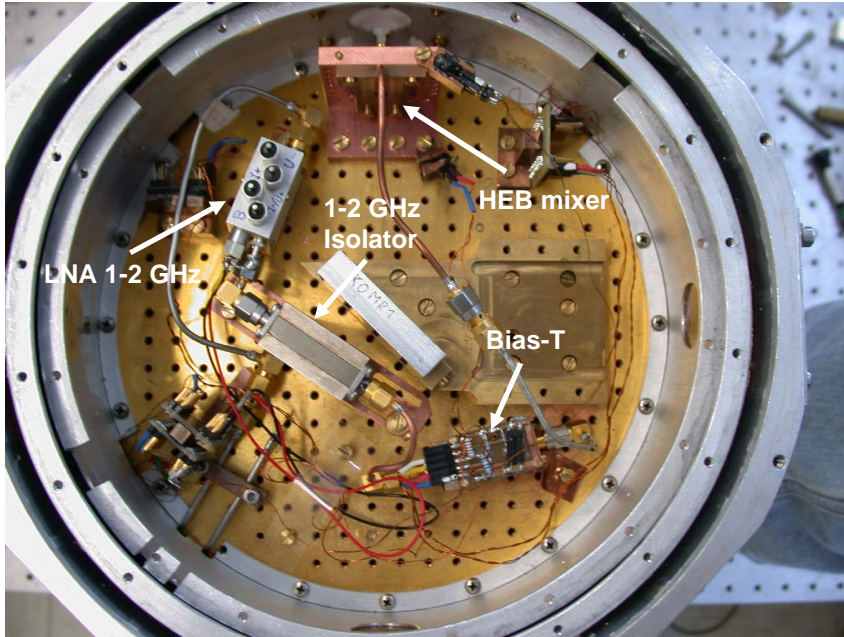
**Figure 7.5:** View inside the cryostat. The experimental setup of the noise temperature measurement at 0.8 THz.

of the NbN HEBs and NbTiN HEBs directly because of the different device geometry.

Figure 7.6 shows the current-voltage characteristic (I-V) for both the NbN and the NbTiN HEB devices each with LO power applied to the input of the mixer (pumped) and without LO power applied to the input of the mixer (unpumped) at a temperature of 4.2 K. The unpumped I-V curves are not continuous because of the hysteresis below voltage values of 1 mV for NbN and below 1.5 mV for NbTiN. To find the optimal operating bias point, the LO power is increased until the I-V curve is non-hysteretic. Only if the I-V curve is non-hysteretic the mixer output is stable.

The general shape of the I-V curve is very similar for both HEB devices. The normal state resistance at the operation temperature was almost the same as at room temperature.

The major difference is the critical current of the two devices. The critical current of the NbN device is $I_c = 141$ µA and the critical current of the NbTiN device is $I_c = 498$ µA. Furthermore the NbN HEB device is slightly less pumped than the NbTiN HEB device at

**Figure 7.6:** I-V characteristics of NbN and NbTiN HEB mixers without LO power and pumped with optimum LO power.

the optimal operation condition.

# 7.5 Performance of the NbN HEB

## 7.5.1 Receiver Noise Temperature

The receiver noise temperature $T_{rec}$ of the NbN HEB mixer was measured using the standard Y-factor method described above. It was possible to perform a continuous measurement of the receiver noise temperature across the IF band (1-2 GHz).

Figure 7.7 shows the uncorrected receiver noise temperature $T_{rec}$ as a function of the IF frequency. Uncorrected means that the receiver noise temperature $T_{rec}$ is not corrected for any losses. It has become common for some groups to correct the receiver noise temperature $T_{rec}$ of quasi-optical mixers for the major optical losses in the signal path. The major optical loss occurs by reflection on the lens surface. It is possible to use an antireflection coating on the surface of the silicon lens to reduce the reflection. Sometimes measurements are performed without this antireflection coating and afterwards the receiver noise temperature is corrected for the 1.5 dB reflection loss. Therefore these noise temperature measurements should be carefully compared with measurements from other groups.

All the measurements at KOSMA were performed without an antireflection coating on the silicon lens, which contributes about 30% to the receiver noise temperature [74], but the receiver noise
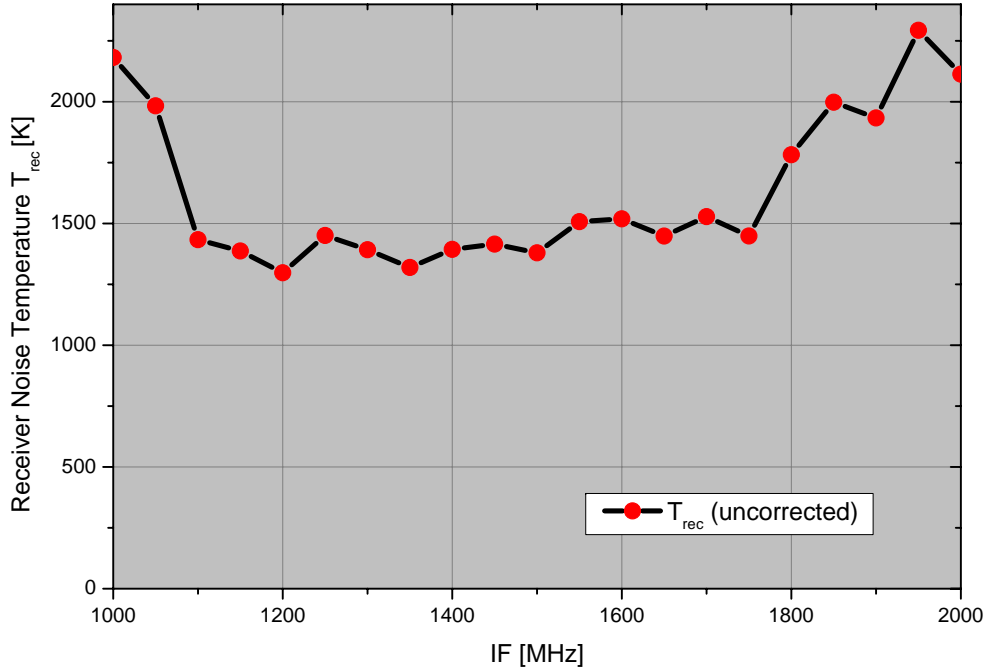
**Figure 7.7:** Uncorrected receiver noise temperature $T_{rec}$ as function of the IF for the NbN HEB mixer ($4.0 \times 0.6$ μm) at 0.8 THz LO-frequency.

temperature is not corrected for the lens reflection loss.

The lowest receiver noise temperature $T_{rec}$ is 1344 K at 1.2 GHz IF. The bias range yielding the lowest noise temperature was very wide (see below). A bias point of 1.5 mV was chosen to determine the receiver noise temperature from the measured Y-factor. The increase of the receiver noise temperature $T_{rec}$ at the lower end of the IF band ($< 1.05$ GHz) and at the upper end of the IF band ($> 1.8$ GHz) is due to the limited bandwidth of the isolator.

A network analysis was performed to determine the ratio of the transmitted signal to the incident signal. A network analyzer contains a source and a receiver and can measure reflections in amplitude and phase of components, circuits and devices. Figure 7.8 show the forward transmission coefficient (S21) as a function of the frequency of the 1-2 GHz isolator used for the RF measurement. From 1 GHz to 1.8 GHz the isolator obtains a good transmission for the IF signal, while for frequencies higher than 1.8 GHz the
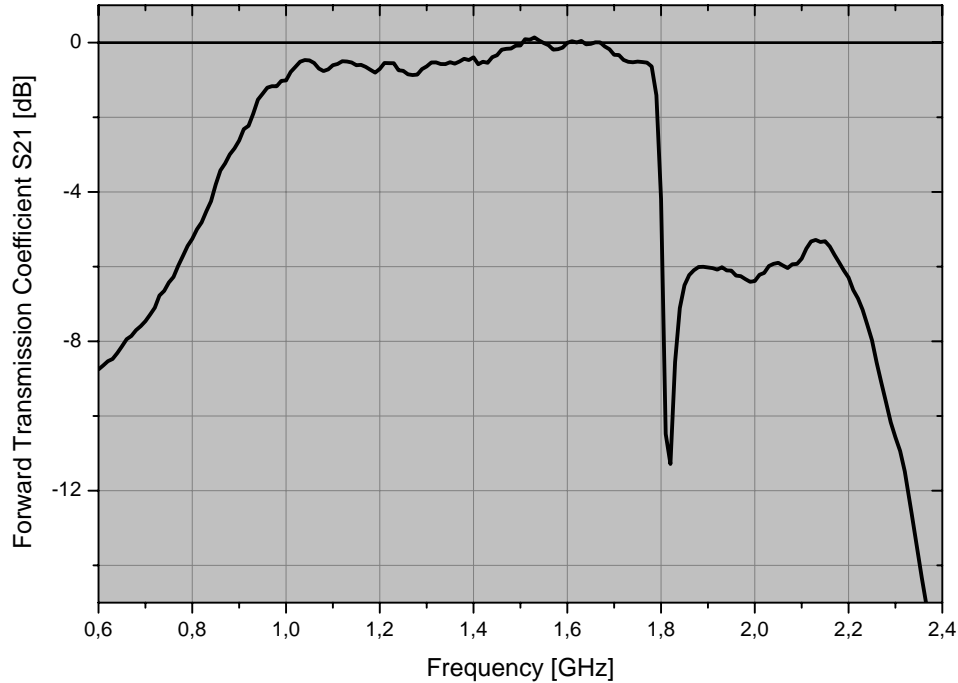
**Figure 7.8:** Forward transmission coefficient (S21) as function of frequency of the 1-2 GHz isolator used for the RF measurement. Measurements performed by P. Munoz

transmission drops below -5 dB. That measurement shows that the IF signal is transmitted almost without loss for frequencies from 1.0 GHz to 1.8 GHz.

An IF dependence of the receiver noise temperature is not observed within the bandwidth of the isolator. The noise temperature varies within 10% in the frequency range of the isolator. The noise temperature bandwidth of a NbN HEB mixer is expected to about 3-4 GHz [43]. Since this NbN HEB mixer does not show an increase of the noise temperature within the bandwidth of the isolator this characteristic indicates that noise temperature bandwidth should be more than 2 GHz. Measurements using a more broad band IF amplifier chain have to be used to confirm this assumption.

Figure 7.9 shows the IF output power for hot (300 K) and cold (77 K) load applied to the signal port of the receiver as a function of the bias voltage. The measurement was a sweep measurement. The bias voltage was swept from -6 to +6 mV using a scan time
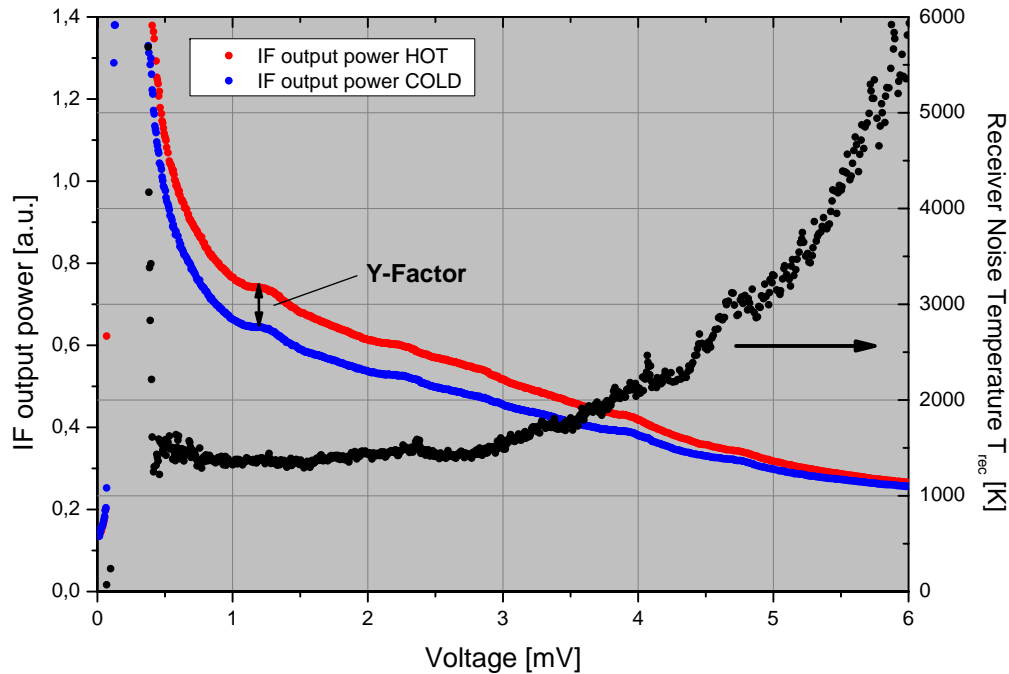
**Figure 7.9:** IF output power for a hot (300K) and cold (77) load applied to the signal port of the receiver as function of the bias voltage. The corresponding receiver noise temperature as function of the bias voltage is also plotted in this graph.

of 2 ms for each current measurement point. The corresponding receiver noise temperature $T_{rec}$ as function of the bias voltage is also plotted in figure 7.9. This mixer has wide bias voltage range from 0.5 to 2.2 mV where the receiver noise temperature is almost constant below 1500 K.

## 7.5.2 Loss Contributions in the Receiver

Losses in the signal path at RF and IF influence the receiver noise temperature of the mixer.

Before the various components are considered, a general concept for the a linear chain of lossy components is derived. The optical components such as beam splitter, cryostat window and infrared (IR) filter act as attenuator so the signal. Beside the atten-

uation, these components also have an intrinsic noise. Both the attenuation and the intrinsic noise of the components degenerate the signal to noise ratio (SNR), which is the signal strength relative to background noise. The gain G of an attenuator is $G < 1$ and is therefore associated with the loss factor $L = \frac{1}{G}$. The noise temperature $T_N$ of an optical component at the temperature $T_{phys}$ is:

$$T_N = (L - 1)T_{phys} \tag{7.13}$$

That means that an optical component with a loss factor of $L = 2$ (3 dB) contributes $T_N = T_{phys}$ to the noise temperature of the whole system. Beside this additive noise component, another effect on the receiver noise temperature $T_{rec}$ occurs for a linear chain of lossy components as shown in figure 7.10.
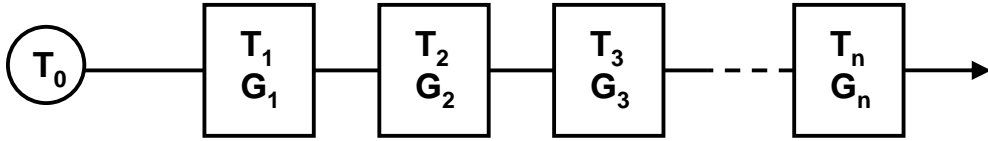


**Figure 7.10:** Linear chain of lossy components.

Each component has a noise temperature $T_{1,2,3...n}$ and a gain $G_{1,2,3...n}$. The power output of the whole chain is:

$$\begin{aligned} P_{out} &= G_1 G_2 G_3 \ldots G_n k T_0 B + G_1 G_2 G_3 \ldots G_n k T_1 B + \ldots \\ &\quad + G_1 G_2 G_3 \ldots G_n k T_n B \end{aligned} \tag{7.14}$$

and the equivalent input noise temperature is:

$$T_{in} = T_0 + T_1 + \frac{T_2}{G_1} + \frac{T_3}{G_1 G_2} + \ldots + \frac{T_n}{G_1 G_2 \ldots G_{n-1}} \tag{7.15}$$

The signal chain of the real system is shown in figure 7.11. The first optical attenuation element at ambient temperature (293 K)

is the 12 μm Mylar beam splitter, used for coupling the LO radiation and the black-body load radiation into the cryostat. Mylar is a polyethylene polyester film with a high transparency for radiation in the millimeter and submillimeter frequency range. In principle the beam splitter is a Mylar foil mounted on a circular metal frame. The Mylar foil is used in a 45° angle so that the black-body load radiation is transmitted through the beam splitter and the LO radiation is reflected by the beam splitter. The transmission of the Mylar beam splitter at horizontal polarization at 804 GHz is calculated to be 92 %. The calculated values have been confirmed by fourier-transform-spectrometer (FTS) measurements [85]. The beam splitter attenuation of -0.41 dB contributes to the receiver noise temperature $T_{rec}$.

The next optical component at ambient temperature is the Teflon Cryostat window. The FTS was also used to determine the transmission and the reflection of the 0.52 mm thick Teflon window. The loss due to transmission and reflection was found to be 5 % for 800 GHz [85]. The transmission and the reflection loss of the 0.7 mm thick Teflon window embedded into the 77 K shield is 8 % [83]. The Teflon windows in the signal path contribute a loss due to attenuation and reflection of -0.62 dB.

Two layers of Zitex G 108 [82] (0.2 mm thick) were used as an IR filter inside the cryostat. The optical properties of Zitex have been investigated in [83]. Zitex G 108 should have a transmission of more than 96 % at 800 GHz. In our measurement setup 2 layers of Zitex were used. Therefore a FTS measurement of 2 Zitex layers was performed to verify the transmission. A transmission of 88,18 % was measured by the FTS [85] in contrast to the predicted 96 %. An attenuation loss of -0.5 dB is estimated.

The signal radiation is coupled into the HEB device by a silicon lens and a planar antenna which is clamped on the backside of the lens. Due to the high refractive index of silicon, a high reflection loss of -1.5 dB occurs on the surface of the lens [67]. By using a Parylene antireflection coating the reflection can be significantly reduced. For these measurements a silicon lens without an antireflection coating was used. Assuming an absorption loss in high-resistivity ($> 5$ kΩcm) Silicon of -0.1 dB, the silicon lens contributes -1.6 dB attenuation to the whole signal chain of the receiver.

The loss of all the optical components at 804 GHz sums up to $G_{opt} \approx -3$ dB. This is comparable to the loss reported by other

113

**Gain:** -0.41 dB    -0.62 dB      -0.5 dB    -1.6 dB    -0.5 db      -14 dB    +98 dB

**Noise:** 1250 K    1138 K      986 K      879 K    608 K      542 K

```
        ┌────────┐ ┌────────┐ ┌────────┐ ┌────────┐ ┌────────┐
   ───▶ │ beam-  │ │Teflon- │ │  IR    │ │  Si    │ │Antenna │ ──◯──  ▷
        │splitter│ │windows │ │ filter │ │ Lens   │ │coupling│
        └────────┘ └────────┘ └────────┘ └────────┘ └────────┘
```

Optical Loss        RF-Loss    Mixer    IF amplifier
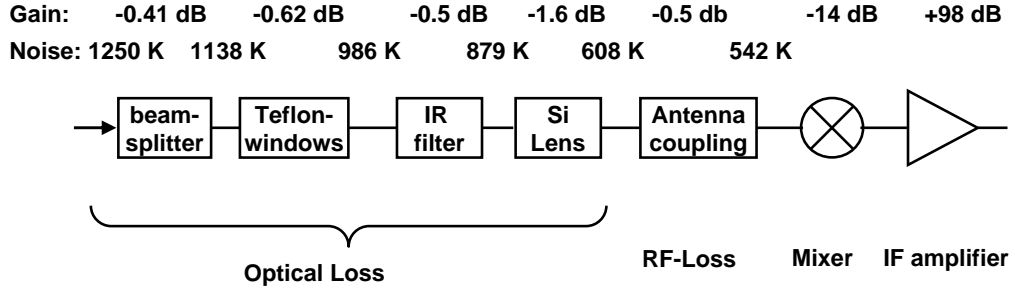
**Figure 7.11:** Signal chain of the receiver. The performance is calculated for a receiver noise temperature $T_{rec}$ = 1250 K.

groups [2].

Another main loss occurs by coupling the propagating beam into active HEB device. This is achieved by quasi-optical coupling using a planar antenna, which is discussed in chapter 5 in more detail. Büttgenbach found that the aperture efficiency of a planar logarithmic spiral antenna is 76 % [86]. The impedance mismatch between the HEB device and the planar antenna causes a loss in the signal path as well. The coupling loss due to the HEB device integrated into a planar antenna is assumed to add another -0.4 dB attenuation loss to the system chain.

Table 7.2 summarizes the losses described above. According to the table 7.2 the silicon lens contributes the major loss. The total loss of the signal chain of the receiver is -3.44 dB. This means that only 45 % of the total power provided to the receiver system is actually dissipated on the HEB device.

The estimation of an attenuation of -3.44 dB is very optimistic. According to simulations of Focardi et.al., the total power loss in this kind of receiver operating at 2.5 THz was shown to be -6 dB. Although the model is applied to a twin slot antenna at 2.5 THz it is reliable at 800 GHz [87].

There is not a straightforward way to measure the loss in the RF coupling and the mixer conversion loss separately. Therefore the RF losses and the mixer conversion loss can not be separated. The antenna coupling loss is not included in the calculation of the mixer noise temperature $T_{mix}$ which follows below.

| Component | Material | Gain [dB] | Phys. Temp. [K] |
|---|---|---|---|
| Beam splitter | Mylar | -0.41 | 293 |
| Cryostat window | Teflon | -0.23 | 293 |
| 77K window | Teflon | -0.39 | 77 |
| IR filter | Zitex | -0.41 | 4 |
| Si lens (reflection) | Silicon | -1.50 | 4 |
| Si lens (absorption) | Silicon | -0.10 | 4 |
| antenna coupling | - | -0.40 | 4 |

**Table 7.2:** Losses from components in the measurement system

### 7.5.3 Calibration of the IF System

The losses described above are all losses within the RF part of the receiver. The down-converted IF signal is further amplified by a low noise amplifier (LNA) at 4 K and by several amplifier stages at ambient temperature. Each amplifier adds noise to amplified signal. The LNA is the most important part in the IF chain, since the gain and the noise temperature of the LNA determines the gain and the noise temperature of the whole IF chain. The first amplifier in the IF chain influences the rest the IF chain as described in equation 7.14 and 7.15.

The first-stage intermediate frequency (IF) amplifier is a 1-2 GHz low-noise HEMT amplifier operating at 4.2 K. (25 dB gain at 1.5 GHz). The IF signal is further amplified by room temperature amplifiers.

The following approach was used to calibrate if IF amplifier chain. The HEB mixer is heated above its critical temperature $T_c$ so that the HEB acts like a normal conducting resistor. Heating the HEB is achieved by a resistor which is bolted to the mixer block. The temperature T of the mixer block is measured by a calibrated temperature diode.

The input noise power of the IF amplifier chain is:

$$
\begin{aligned}
P_{IF,in} &= kB(T + T_{IF}) \\
&= P(T) + kBT_{IF}
\end{aligned}
\tag{7.16}
$$

where $T_{IF}$ is the noise temperature of the IF amplifier chain, B the bandwidth and k the Boltzmann constant. P(T) is the noise power of the HEB at the temperature T, which acts as a resistor

at the physical temperature T. The output noise power of the IF amplifier chain is:

$$
\begin{aligned}
P_{IF,out} &= P_{IF,in} \cdot G_{IF} \\
&= P(T) \cdot G_{IF} + kBT_{IF} \cdot G_{IF}
\end{aligned}
\tag{7.17}
$$

where $G_{IF}$ is the gain of the IF amplifier chain. The output noise power $P_{IF,out}$ is measured at five different temperatures ranging form 8 K to 20 K.

If the noise power of the HEB in the resistive state is plotted versus the measured output noise power $P_{IF,out}$, the slope of the graph represents the gain of the IF amplifier chain $G_{IF}$ and the intercept represents the noise temperature of the IF amplifier chain $T_{IF}$. The output noise power $P_{IF,out}$ was measured with a calibrated power meter for different IF.

Figure 7.13 shows the gain of the IF amplifier chain as a function of the IF. From 1.05 GHz IF up to 1.95 GHz IF the IF amplifier chain has a gain of about 97 dB. The gain values for frequencies higher than 1.8 GHz should decrease since the transmission of the isolator drops by 5 dB for frequencies higher than 1.8 GHz. It is not clear why the gain of the IF chain increases to values higher than 100 dB for frequencies higher than 1.8 GHz.

Figure 7.12 shows the noise temperature of the IF amplifier chain as a function of the IF. The noise temperature remains constant between 6 K and 9 K in the range from 1.2 GHz to 1.8 GHz IF.

## 7.5.4  Mixer Noise Temperature

The mixer noise temperature $T_{mix}$ is an intrinsic property of the HEB mixer. A noise theory for a HEB mixer can just predict a mixer noise temperature $T_{mix}$, the receiver noise temperature $T_{rec}$ can always be different since it depends on the optics and the IF chain. Therefore, the mixer noise temperature $T_{mix}$ does not account for the influence of the optics and the IF amplifier chain, as described in section 7.2

The mixer noise temperature $T_{mix}$ can be derived from the receiver noise temperature $T_{rec}$ considering the losses in the optical elements as given in table 7.2 and the loss in the IF amplifier chains
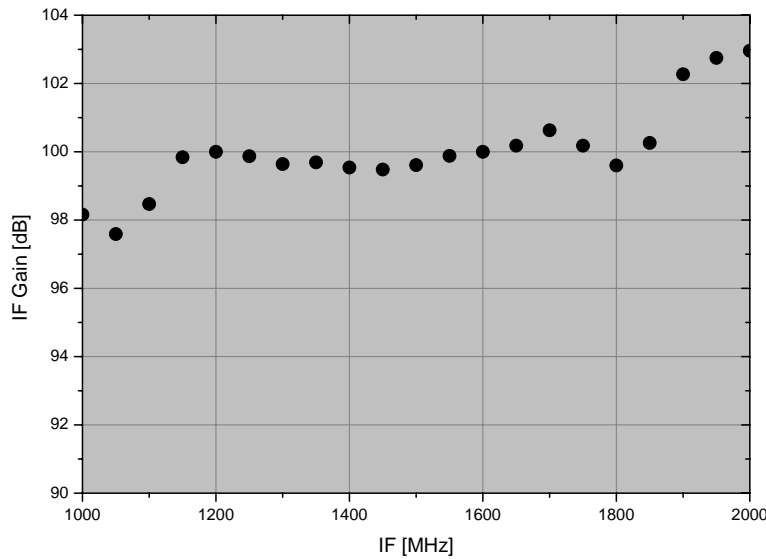
**Figure 7.12:** Gain of the IF amplifier chain as function of the IF frequency.

described in 7.5.3. In figure 7.14 the mixer noise temperature $T_{mix}$ is shown as a function of the IF for 1-2 GHz.

The minimum mixer noise temperature $T_{mix}$ is 420 K at 1.1 GHz IF. The rise in the mixer noise temperature at 1.8 GHz IF is due to the isolator cut-off frequency of 1.8 GHz. So it is not possible to derive the noise bandwidth of the HEB mixer by that measurement. There is a continuous increase of the mixer noise temperature from 440 K to almost 600 K, but like for the receiver noise temperature measurement the bandwidth of the IF chain is too narrow to estimate a bandwidth of the mixer.

The receiver noise temperature $T_{rec}$ is 1450 K at 1.1 GHz IF. That shows that the receiver noise temperature is dominated by noise from the optics and the noise from the IF amplifier.

## 7.5.5 IF Bandwidth

The efficiency to convert the high-frequency RF signal into an IF signal is characterized by the conversion gain G of the mixer.

For an IF bandwidth measurement the black body load is replaced by a coherent source and a wide-band IF amplifier chain is used. In order to determine the IF bandwidth of the HEB the IF
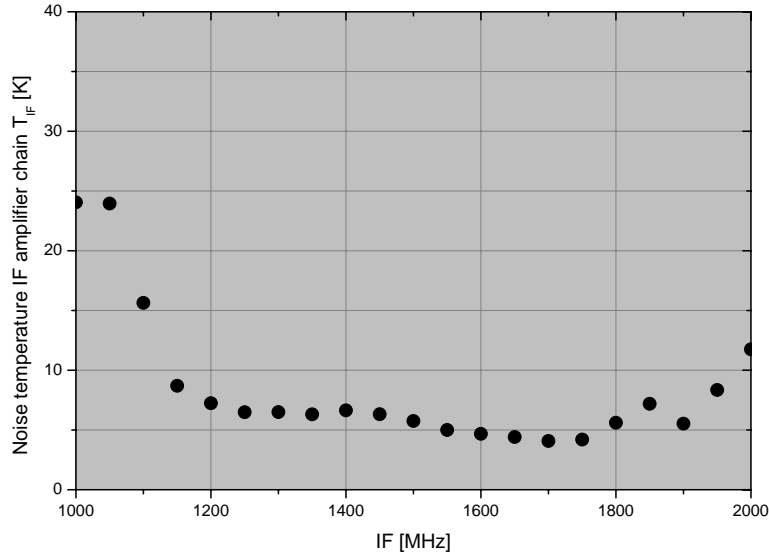
**Figure 7.13:** Noise temperature of the IF amplifier chain as function of the IF.

amplifier chain should span at leat a few times the IF bandwidth of the device. Than the LO and the signal frequency can be tuned to span the entire IF bandwidth of the device.

The experimental setup lacked of a wide band IF amplifier chain and of a second coherent source. However, there is a possibility to deduce the gain from the receiver noise temperature $T_{rec}$ measurements.

Knowing the loss of the optics and the gain of the IF amplifier chain $G_{IF}$, the mixer gain $G_{mix}$ can be determined from the receiver gain $G_{rec}$. The receiver gain $G_{rec}$ can be derived from the noise temperature measurement together with the known noise and gain of the IF chain.

The IF output power in response to a hot (293 K) and a cold (77 K) load are:

$$\begin{aligned}
P_{IF,hot,out} &= G_{rec} \cdot P_{IF,hot,in} \\
P_{IF,cold,out} &= G_{rec} \cdot P_{IF,cold,in}
\end{aligned} \tag{7.18}$$

where $G_{rec}$ is the receiver gain and $P_{IF,in}$ is the noise power applied to the input of the receiver. The noise power of a hot (293 K) and a cold (77 K) load are:
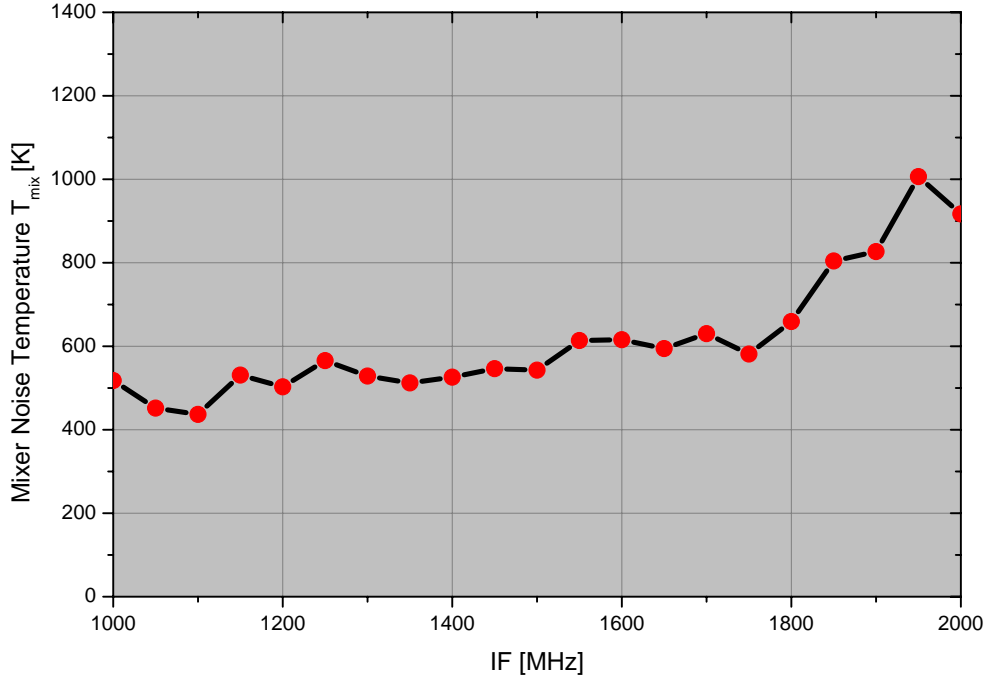
**Figure 7.14:** Mixer noise temperature $T_{mix}$ as function of the IF.

$$\begin{aligned} P_{IF,hot,in} &= k\ BT_{hot} \\ P_{IF,cold,in} &= k\ BT_{cold} \end{aligned} \qquad (7.19)$$

with $k$ the Boltzmann constant and $B$ the bandwidth. After subtracting, rewriting and using equation 7.19 the receiver gain is:

$$G_{rec} = \frac{P_{IF,hot,out} - P_{IF,hot,out}}{k\ B(T_{hot} - T_{cold})} \qquad (7.20)$$

The mixer gain $G_{mix}$ can be derived by subtracting the gain from the optics and the gain from the IF.

$$G_{mix} = G_{rec} - G_{optics} - G_{IF} \qquad (7.21)$$

An alternative way to evaluate the mixer gain $G_{mix}$ is the so called U-factor method [88]. The U-factor is the ratio between the receiver output power $P_{IF,hot}$ with a hot (293 K) load applied to the receiver input and the receiver output power at zero bias current

119

$P_{IF,sc}$. At zero bias current the IF impedance of the mixer is zero, therefore the mixer reflects back the isolator noise ($T_{bath}$) to the amplifier.

$P_{IF,hot}$ is the combination of the receiver noise and the noise signal from the load:

$$P_{IF,hot} = 2kBG_{IF}G_{mix+opt}(T_{rec} + T_{hot}) \qquad (7.22)$$

where $k$ is the Boltzmann constant, $B$ is the bandwidth, $G_{IF}$ is the gain of the IF amplifier chain and $G_{mix+opt}$ is the gain of the mixer and the optics. The factor of two is because the two port model for a DSB mixer is used, where the mixer conversion gain is treated separately for the signal and the image part.

$P_{IF,sc}$ can be written as:

$$P_{IF,sc} = kBG_{IF}(T_{bath} + T_{IF}) \qquad (7.23)$$

with $T_{bath}$ is the bath temperature (4.2 K) and $T_{IF}$ is the noise temperature of the IF amplifier chain.

Using the U-factor:

$$U = \frac{P_{IF,hot}}{P_{IF,sc}} \qquad (7.24)$$

the gain of the mixer and the optics can be calculated by:

$$G_{mix+opt} = \frac{1}{2}\frac{U(T_{bath} + T_{IF})}{T_{rec} + T_{hot}} \qquad (7.25)$$

The main advantage of the U-factor method is that the gain of the IF chain $G_{IF}$ is not needed.

Assuming an optical attenuation of -3.44 dB (see section 7.5.2) the mixer gain can be calculated.

Figure 7.15 shows the mixer gain $G_{mix}$ calculated using the standard and the U-factor method, as function of the intermediate frequency. The mixer gain of about -13 dB (at 1.4 GHz IF) can be expected from a good mixer at 0.8 THz. The mixer gain decreases for higher intermediate frequencies. The mixer gain values for an intermediate frequency higher than 1.8 GHz are not reliable because the used isolator has a narrow bandwidth of 1.1 - 1.8 GHz.

The expected IF frequency dependence is [15]:

$$\frac{G(f)}{G(0)} = \frac{1}{1 + (\frac{f}{f_{3dB}})^2} \qquad (7.26)$$
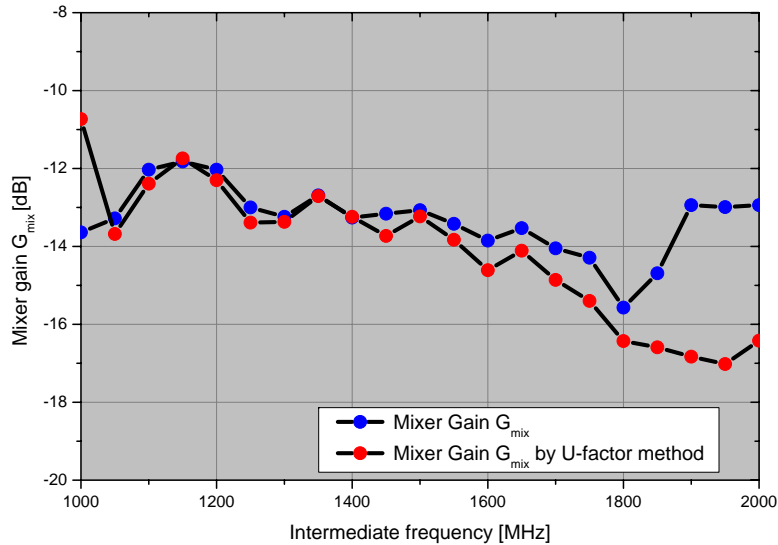
**Figure 7.15:** Mixer gain, derived by the standard method and the U-factor method as function of the intermediate frequency.

where $f_{3dB}$ is the IF frequency at which the IF output power drops by 3 dB. One can see that the mixer gain at 1.8 GHz dropped by 3 dB, but there are not enough data points to perform a fit based on equation 7.26. But figure 7.15 indicates that the IF gain bandwidth is not much higher than 1.8 GHz.

Either the IF amplifier chain including the isolator need to have a larger bandwidth (for example 1-5 GHz) or a separate IF bandwidth measurement equipment is needed.

It is remarkable that both methods used to extract the mixer gain result in similar results for the mixer gain for frequencies smaller than 1.8 GHz. It is also remarkable that the U-factor method seems to produce reasonable Mixer gain value for frequencies higher than 1.8 GHz, while the other method produces strange mixer gain values for frequencies higher than 1.8 GHz.

## 7.5.6 LO Power absorbed in the HEB

The LO power requirement for heterodyne mixers at THz frequencies is an important factor, since LO power sources are difficult to implement and do not have much more than about 1 μW at 1.4 THz

right now.

The isothermal technique can be used to deduce the LO power dissipated in the HEB device [89]. The basic assumption of the isothermal technique is that the absorption of DC or RF power has the same influence of the HEB device resistance. The absorbed LO power is derived from two I-V curves with different LO powers.

At each point of a constant resistance line the total power absorbed by the HEB device is:

$$P_{LO} + V_a \cdot I_a = \alpha P_{LO} + V_b \cdot I_b \tag{7.27}$$

where $\alpha$ is the attenuation factor for the two different LO levels. Using equation 7.27 the absorbed LO power is:

$$P_{LO} = \frac{V_b \cdot I_b - V_a \cdot I_a}{1 - \alpha} \tag{7.28}$$

The attenuation factor is $\alpha = 0$, if the I-V curves corresponds to an unpumped and an any pumped HEB device. In this case equation 7.28 is simply:

$$P_{LO} = V_b \cdot I_b - V_a \cdot I_a \tag{7.29}$$

The absorption of the DC and RF power is more uniform close to the normal state region, therefore this region should be used for the isothermal technique [90].

Figure 7.16 shows two I-V curves, one without LO power applied to the HEB device and one with the optimal LO power applied to the HEB device. The dotted line is the constant resistance line.

Using the isothermal technique equation (7.29) the estimated absorbed LO power is 55 nW. It should be mentioned that the isothermal technique is only a rough estimation of the absorbed LO power.

The estimated incident LO power on the HEB device derived from the losses shown in table 7.2 is about 4 μW for an initial LO power of about 100 μW. The absorbed LO power calculated by the isothermal technique is lower than the estimated incident LO power by 18 dB. It is known that the isothermal technique gives much lower values for the absorbed LO power than the actual power available at the mixer [91]. But usually a factor 4 (or 6 dB) between the real LO power need and the isothermal technique is found.
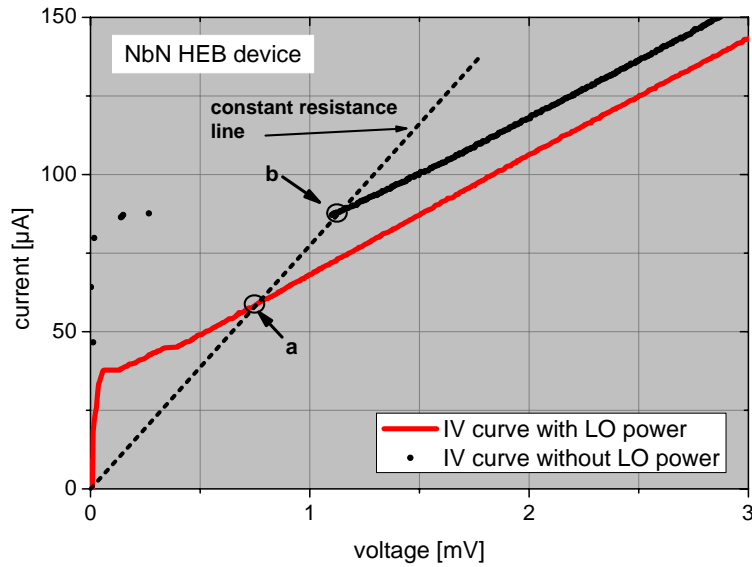
**Figure 7.16:** Two different I-V curves, one without LO power applied to the HEB device and one with the optimal LO power applied to the HEB device. The dotted line is the constant resistance line.

The initial LO power was taken from the data sheet of the solid state LO. This value might be right within a factor of 2.

## 7.5.7   Conclusions of the NbN HEB Performance

A detailed characterization of the NbN phonon-cooled HEB mixer was performed. It was possible to pump the device at a LO frequency of 0.8 THz. The LO power absorbed by the HEB device is 55 nW. This is lower than expected for a NbN device with this volume.

The receiver noise temperature $T_{rec}$ is 1344 K at 1.2 GHz IF. This receiver noise temperature is higher than the state-of-the-art receiver noise temperature at this frequency. This is due to the losses in the optics. After the correction for the optics and the IF amplifier loss, the estimated mixer noise temperature $T_{mix}$ is 420 K.

It was not possible to determine the noise bandwidth of this device. The noise temperature did not increase by the factor of two in the bandwidth of the isolator. So the noise bandwidth is believed to be larger than 1.8 GHz.

The mixer gain $G_{mix}$ is -13 dB at 1.4 GHz IF. This value is similar to that reported by other groups.

It was not possible to determine the gain bandwidth of the NbN HEB device by fitting the data to the expected IF frequency dependence. More data points are needed for this. But the mixer gain at 1.8 GHz dropped by 3 dB which indicates that the IF gain bandwidth is not much higher than 1.8 GHz.

# 7.6 Performance of the NbTiN HEB

In this section the mixer performance of the NbTiN HEBs is presented. These NbTiN HEBs have been fabricated on bare Silicon (Si) substrates and on Si substrates with Aluminium Nitride (AlN) buffer layers. The critical temperature $T_c$ and the normal state resistivity are observed to improve in the case of using a buffer layer like MgO for NbN [92] and NbTiN [56] ultrathin films.

An increase in critical temperature $T_c$ of 1-2 K can be quite important, since the critical temperature influences the electron relaxation time of the HEB. The buffer layer is also important for the acoustic matching of the NbTiN film to the substrate material and therefore for the phonon escape time. For NbTiN films on a MgO buffer layer using a Si substrate, it has been shown that the phonon escape time is the bottleneck of the electron relaxation time for temperatures above 10 K [56].

At the very beginning of this work, substrate heating was limited (400°C) and an AlN buffer layer was the only way to obtain 5 nm thin NbTiN films with a critical temperature $T_c$ above 4 K. By introducing a new PBN/Pyrolytic Graphite (PG) resistance heating element, it was possible to deposit 5 nm thin NbTiN films on Si substrates without an AlN buffer layer, at a deposition temperature of 600-800°C.

Therefore this section covers the mixer performance of two different HEB devices based on NbTiN: One HEB batch was fabricated on a 5 nm NbTiN film using a 20 nm AlN intermediate layer on a Si substrate, and the other HEB batch was fabricated on a 5 nm NbTiN film on a Si substrate.

## 7.6.1 Receiver Noise Temperature

The experimental setup for the noise temperature measurement of the NbTiN HEBs is the same one used for the NbN HEB noise measurement and is described in section 7.3. The standard Y-factor method is used to determine the sensitivity of the HEB mixer at 0.8 THz LO-frequency. The Callen and Welton definition is used to calculate the noise temperature from the Y-factor.

Table 7.3 summarizes the dimensions, the critical temperature $T_c$ and the room temperature resistance of the NbTiN HEB devices used for the noise temperature measurement. The critical temper-

125

ature $T_c$ is quite similar for both HEB devices. The device dimensions are very different. This is due to electron beam lithography problems during the fabrication process of the HEB batch Earth 11.

| Device Name | Material | HEB size [μm × μm] | Crit. Temp. [K] | Resistance at 300K [Ω] |
|---|---|---|---|---|
| Earth26-d6 | NbTiN | 2.8 × 0.4 | 8.3 | 38 |
| Earth11-c7 | NbTiN on AlN | 1.5 × 0.7 | 8.0 | 80 |

**Table 7.3:** Properties of NbTiN HEB devices used for the receiver noise temperature measurement

Figure 7.17 shows the measured receiver noise temperature as function of the intermediate frequency. The blue curve shows the receiver noise temperature of the NbTiN HEB on the AlN buffer layer. The noise temperature of the NbTiN HEB without an AlN buffer layer is slightly lower and is indicated by the red line.

The best receiver noise temperature $T_{rec}$ is 2500 K for HEBs without AlN buffer layer and 3000 K for HEBs with AlN buffer layer. This measured noise temperature is unsatisfactory for a HEB mixer at this LO frequency. The high receiver noise temperature of these HEB mixers compared to HEB mixers of other groups is due to an unknown RF coupling loss in the quasi-optical setup.

The IF frequency at which the noise temperature is twice as high as the minimum value is about 1.5 - 1.6 GHz for both kinds of HEB devices. This is called the noise bandwidth of the device.

Since there is no difference in the noise bandwidth observed for the NbTiN HEBs with and without AlN buffer layer, the buffer layer does not seem to be the limiting factor for noise bandwidth. Referring to table 7.3, there is no direct dependence of the noise temperature or the noise bandwidth on the device dimensions, especially on the device length. Therefore the cooling mechanism for these NbTiN HEB mixers is predominantly via phonon-cooling rather than diffusion cooling. Clearly the range of the HEB dimensions does not include a large variation, so it would be necessary to measure a lot more devices with a larger device dimension variation to find a dependance of the noise performance and the device dimensions.

The IF output power in response to hot and cold loads and the
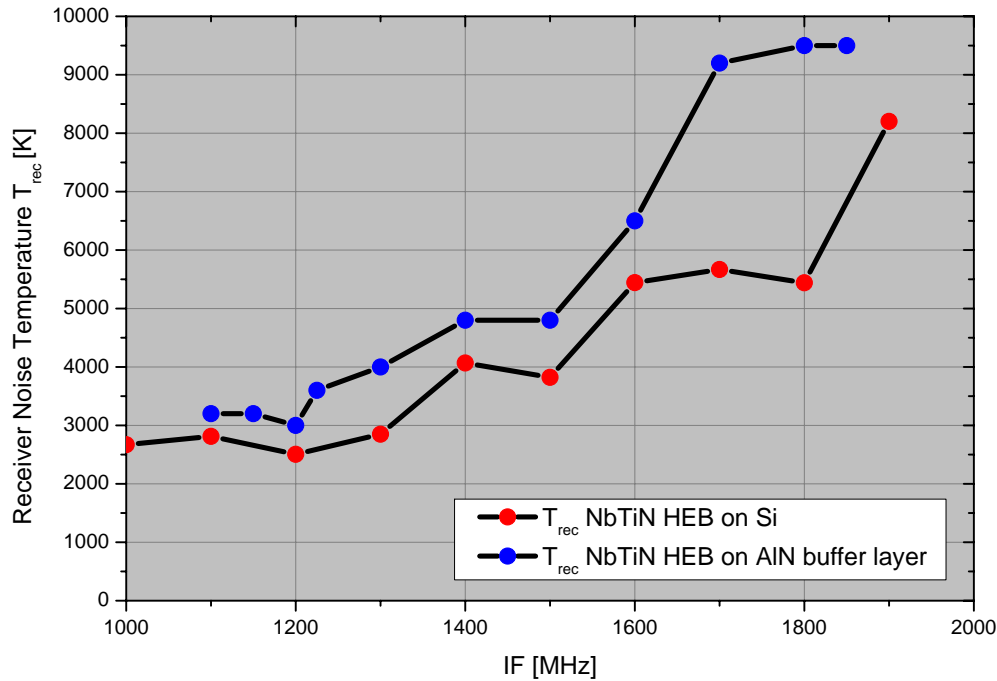
**Figure 7.17:** Uncorrected receiver noise temperature $T_{rec}$ as function of the IF of the NbTiN HEB devices on Si and on an AlN buffer layer for 0.8 THz LO-frequency.

receiver noise temperature as function of the bias voltage are presented in figure 7.18 for device Earth26-d6. The bias range is smaller compared to the previously shown NbN HEB device. A bias voltage range from 0.3 to 0.6 mV results in a receiver noise temperature $T_{rec}$ of about 3000 K. The maximum Y-factor is found at a bias point of 0.5 mV.

The IF output power curve looks different than the one of the NbN HEB device measured in section 7.5. For small voltage values, smaller than 0.4 mV, the IF output power decreases while the IF output power of the NbN HEB device increases for small voltage values increases up to the saturation of the IF amplifier chain. The reason for this behavior is not understood right now.

127
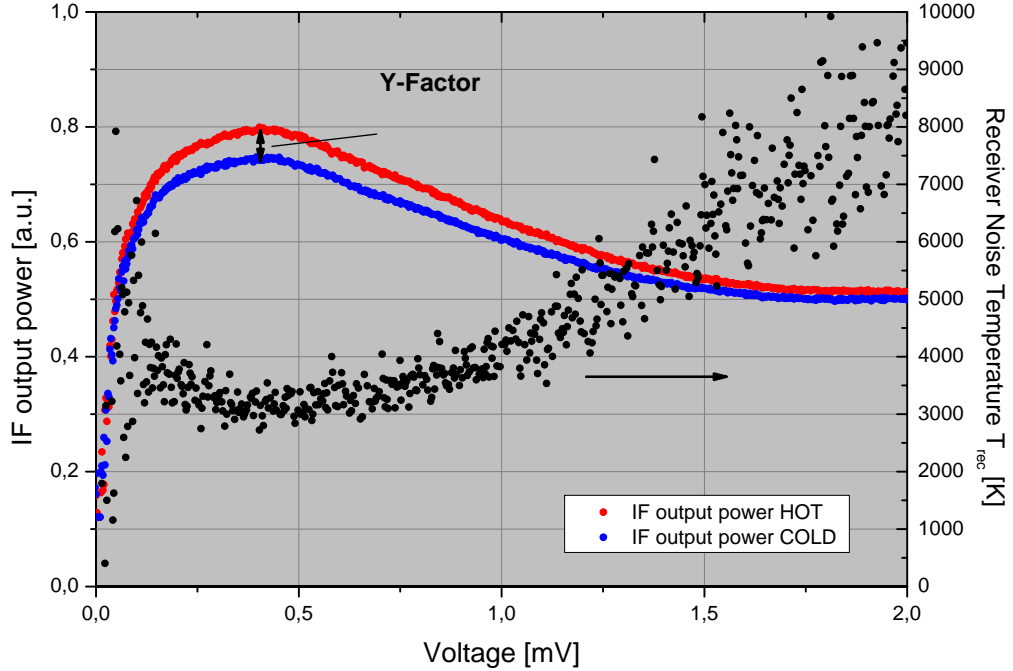
**Figure 7.18:** IF output power for a hot (300 K) and cold (77 K) load applied to the signal port of the receiver as function of the bias voltage at 1.5 GHz IF. The corresponding receiver noise temperature as function of the bias voltage is also plotted in this graph.

## 7.6.2  Loss Contribution of IF

The low noise HEMT amplifier used in this noise temperature measurement is different from the HEMT used for the NbN noise temperature measurement. It is also a 1-2 GHz HEMT amplifier, but it has different gain characteristics. Therefore the calibration of the IF amplifier chain was performed again. The HEB was heated by a resistor above its critical temperature and the IF output power was measured using a calibrated power meter.

The gain of the IF amplifier chain is about 98 dB. Figure 7.19 shows the IF gain as a function if the IF frequency. The IF gain characteristic shows some ripples across the IF band. Since an isolator is used, it is not clear why the high peaks in the gain and noise at certain IF frequencies occur.

Figure 7.20 shows the noise temperature of the IF amplifier
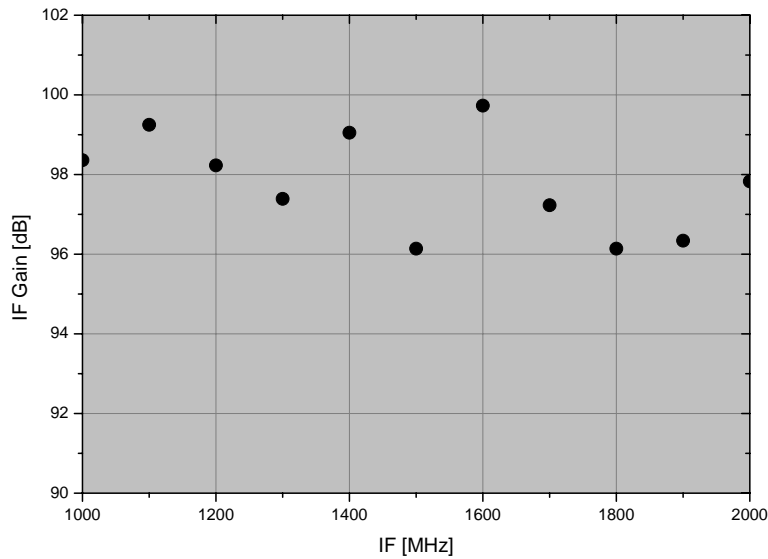
**Figure 7.19:** Gain of the IF amplifier chain as function of the IF used for the NbTiN HEB measurements.

chain as a function of the IF. The noise temperature shows some variation across the IF band. The IF amplifier chain shows a noise temperature of 15-20 K and increases for IF frequencies larger than 1.8 GHz. That means that the receiver noise temperature is dominated by the IF amplifier noise at frequencies about 1.8 GHz. By using equation 7.15, an IF noise temperature of 38 K at 1.9 GHz and a mixer gain of -20 dB at 1.8 GHz causes a noise contribution of the IF chain of about 3000 K.

## 7.6.3  Mixer Noise Temperature

Beside the 50 μm Mylar beam splitter, the loss contributions quoted in section 7.5.2 and the IF calibration was used to determine the mixer noise temperature $T_{mix}$ of the NbTiN HEB mixers. The mixer noise temperature $T_{mix}$ as function of the IF frequency is shown in figure 7.21. The lowest mixer noise temperature $T_{mix}$ was found 500 K for both kind of NbTiN HEBs. The noise bandwidth is found to be 1.5-1.6 GHz. In the case of the NbTiN HEBs the noise bandwidth lies within the bandwidth of the IF chain.

Both the receiver noise temperature $T_{rec}$ and the mixer noise temperature $T_{mix}$ showed a bandwidth of 1.5-1.6 GHz. This con-

129
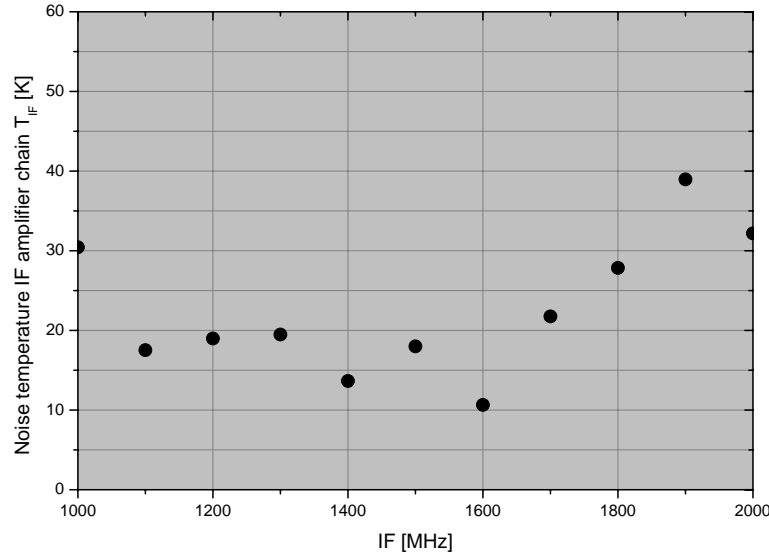
**Figure 7.20:** Noise temperature of the IF amplifier chain as function of the IF frequency used for the NbTiN HEB measurements.

firms that the NbTiN HEBs have a limited noise bandwidth compared the NbN HEB devices.

It was also shown that a bandwidth of 1.2 GHz is obtained for a wide variety of NbTiN HEB device dimensions and bath temperatures [93]. Tong et. al found the -3dB gain bandwidth of a NbTiN HEB on crystalline quartz to be about 2.5 GHz at 600 GHz [57]

## 7.6.4 IF Bandwidth

Figure 7.22 shows the mixer gain $G_{mix}$ of the NbTiN HEB without the AlN buffer layer deduced by the standard and the U-factor method, as function of the intermediate frequency. A mixer gain of about -16 dB (at 1.2 GHz IF) is determined. The mixer gain decreases for higher intermediate frequencies dramatically. A drop by 3 dB if the mixer gain is observed at about 1.5 GHz. Like for the NbN HEB gain it is not possible to perform a fit of the frequency dependence of the mixer gain (equation 7.26 to the measured data point due to the amount of measured data points a IF frequencies larger than 2 GHz.
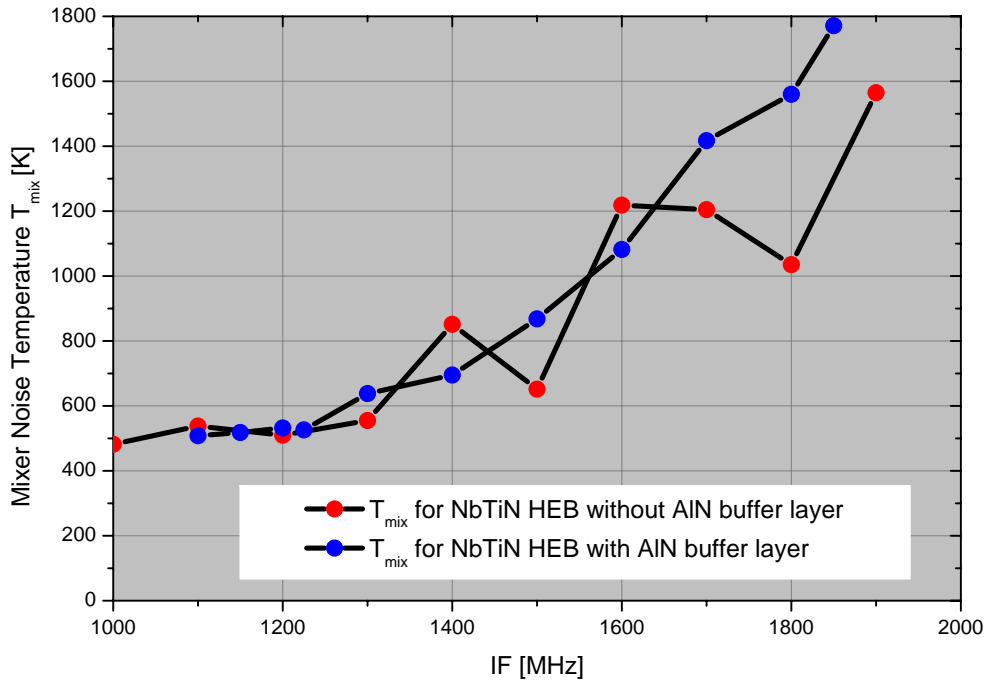
**Figure 7.21:** Mixer noise temperature $T_{mix}$ as function of the IF at 0.8 THz LO-frequency.

### 7.6.5  LO Power Requirement

The LO power requirement was estimated by using the isothermal method described in section 7.16. Figure 7.23 shows the unpumped I-V curve and the optimal pumped I-V curve. The absorbed LO power is found to be about 270 nW. This is 5 times the amount of LO power dissipated in the NbN HEB device, although the volume of the NbN device is 140% larger than the NbTiN device.

Due to the lack of measured data, the LO power requirement of the NbTiN HEB devices using an AlN buffer layer was not performed.

### 7.6.6  NbTiN HEBs at 1.6 THz

The noise temperature measurement presented in this section was performed at the Department of Microtechnology & Nanoscience, Microwave Electronics Laboratory, Chalmers University of Technology, Sweden. The HEB device used in this study was fabricated
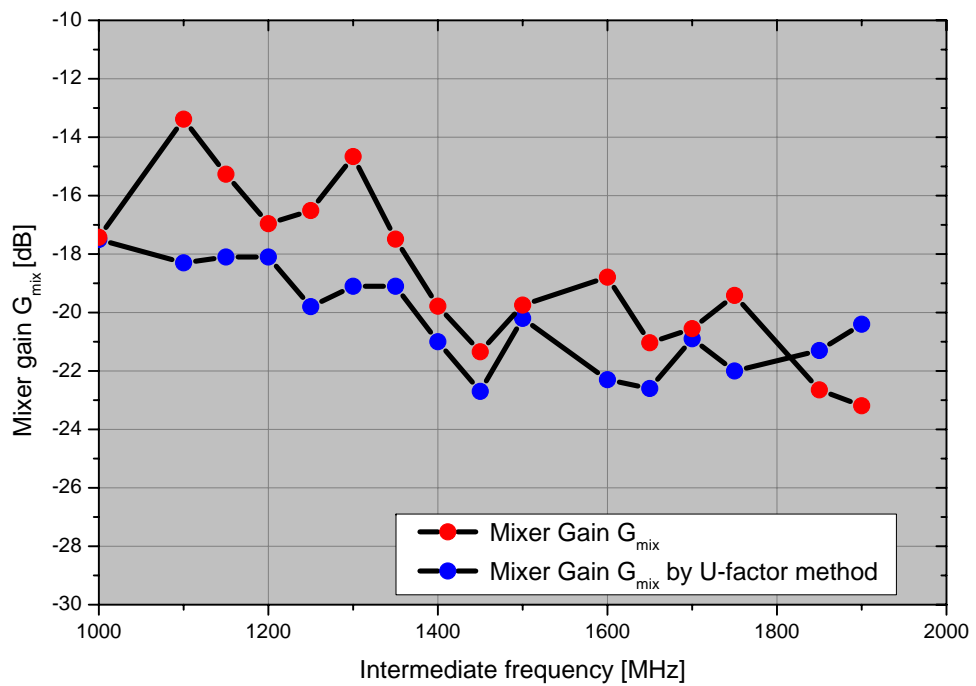
**Figure 7.22:** Mixer gain, derived by the standard method and the U-factor method as function of the intermediate frequency.
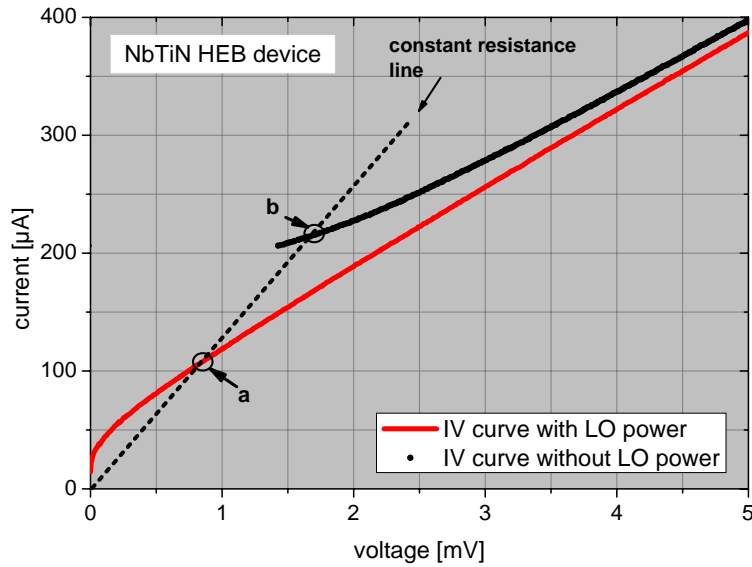
**Figure 7.23:** Two different I-V curves, one without LO power applied to the HEB device and one with the optimal LO power applied to the HEB device. The dotted line is the constant resistance line.

at KOSMA and was than integrated into the quasi-optical mixer of the Chalmers University [94].

This HEB is based on a 5-6 nm thick NbTiN film on a AlN buffer layer on a Si substrate and integrated with a broadband spiral antenna. The device CCN8-1e, having a bridge size of $0.6 \times 4$ µm, has a critical temperature $T_c$ of 8.7 K and a resistivity $\rho$ of 180 µΩcm. The critical current $I_c$ is 430 µm at 4.2 K and the normal-state resistance is 260 Ω.

For the heterodyne measurements the standard receiver configuration of the Chalmers University was used, which is quite similar to the one used in section 7.3. One major difference is the use of an elliptical silicon lens with 28 µm Parylene, which acts as anti-reflection coating. The local oscillator (LO) source for 1.6 THz is a far infrared (FIR) laser. A rotating wire grid served for attenuation of the LO power.

The LO and the RF radiation is combined by a 12 µm Mylar beam splitter. The signal passes through a 1.2 mm thick high-density polyethylene cryostat window and a 0.25 mm Zitex G-108 infrared blocking filter, mounted on the 4 K shield of the cryostat.

The measurement setup is discussed in detail in [94].

The IF amplifier chain consists of an isolator and a 1.4-5 GHz low noise HEMT amplifier. The IF signal is further amplified using two Miteq[TM] amplifiers at ambient temperature and measured through a YIG-filter (30 MHz bandwidth) and a calibrated power meter.

The optimal bias point for this device was fount to be $U_{bias}$ = 0.7 mV and $I_{bias}$ = 30.8 $\mu$A. Figure 7.24 shows the receiver noise temperature at 1.6 THz LO frequency as function if the intermediate frequency.
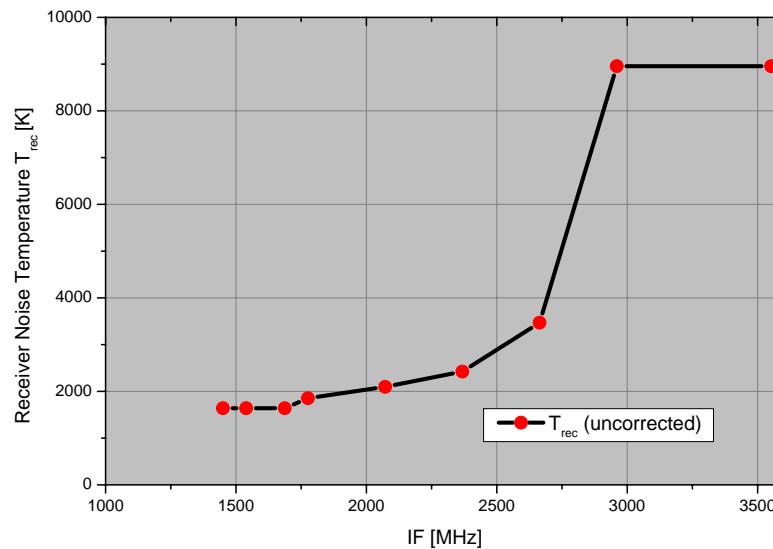


**Figure 7.24:** Receiver noise temperature $T_{rec}$ at 1.6 THz LO-frequency as function of the intermediate frequency

The minimum receiver noise temperature $T_{rec}$ is found to be 1640 K at 1.4 GHz IF. A device made from KOSMA films at Chalmers showed a noise temperature of 1200 K at 1.6 THz. Details can be found in [94]. The receiver noise temperature $T_{rec}$ at 1.6 THz LO frequency is much lower than the receiver noise temperature $T_{rec}$ at 0.8 GHz LO frequency measured at KOSMA. This is possible due to a coupling loss contributed to the measurement setup at KOSMA and the use of the Parylene antireflection coating on the lens surface.

The measured noise bandwidth at 1.6 THz LO frequency is about 2.6 GHz. This is in conflict to the noise bandwidth measured

at 0.8 THz, where the noise bandwidth is found to be about 1.5 GHz for NbTiN HEB devices on Si with and without an AlN buffer layer. The difference in noise bandwidth can not be explained. One reason could be the thickness of the NbTiN film, which is probably thinner than the NbTiN film used for the 0.8 THz devices.

The IF gain bandwidth measurements are taken from the same measurements with operating conditions (LO power and dc bias) giving the lowest receiver noise temperature. The necessary IF chain calibration was performed using the device in the superconducting state as a calibration load, see section 7.5.3. The mixer gain vs. intermediate frequency (IF) is plotted for the spiral-antenna device CCN8-1e in figure 7.25
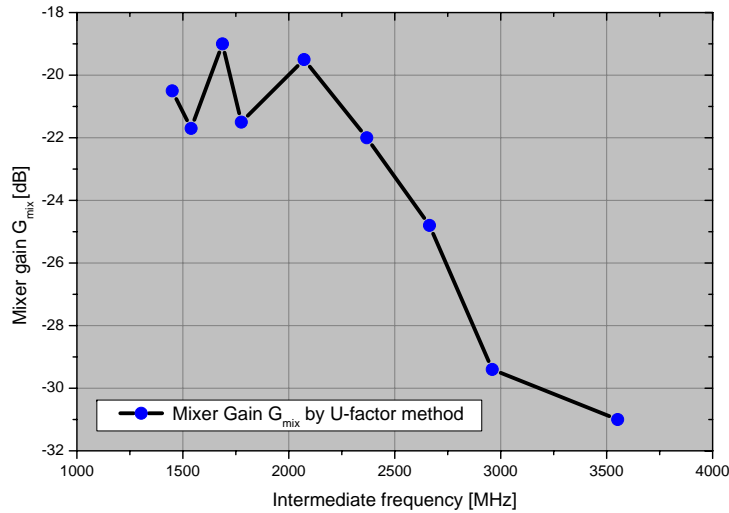


**Figure 7.25:** Mixer gain $G_{mix}$ as function of the intermediate frequency at 1.6 THz LO frequency.

### 7.6.7 Conclusions of the NbTiN HEB Performance

NbTiN HEB devices have been fabricated based on 5-6 nm thick NbTiN film deposited on 20 nm AlN buffer layer on heated high resistivity Si substrates. The receiver noise temperature $T_{rec}$ was measured at 0.8 and 1.6 THz. At 0.8 THz the receiver noise temperature was found to be 2500 K for HEBs without AlN buffer layer and 3000 K for HEBs with AlN buffer layer at 1.2 GHz IF. The measured noise bandwidth was about 1.5 GHz.

The AlN buffer layer does not seem to be the limiting factor for the noise bandwidth, since there is no difference in the noise bandwidth observed for the NbTiN HEBs with and without AlN buffer layer.

The noise temperature at 1.6 THz LO frequency measured at Chalmers is 1600 K at 1.5 GHz IF. This result shows that the noise of these NbTiN HEB devices is comparable with the NbN HEB mixers fabricated at the Chalmers University.

The receiver noise temperature is found to be much lower for the 1.6 THz noise temperature measurement than 0.8 THz measurement. On the one hand this is due to the antireflection coating used at the 1.6 THz measurement and is also due to a coupling loss inside the quasi-optical setup at KOSMA.

The measured noise bandwidth is 1.5 GHz and 2.6 GHz at 0.8 THz and 1.6 THz LO frequency respectively. One possible reason for this possible difference is the thickness of the NbTiN film.

## 7.7 Future Work

Although the noise temperature measurements show a much higher noise temperature for NbTiN HEB devices than for NbN HEB device there should not be any difference in sensitivity for NbTiN and NbN HEB devices [94]. The difference observed in the noise temperature measurements at KOSMA is probably due to the different lens used for the measurements. The lens used for the measurements of the NbTiN HEB devices was a contribution of the Chalmers University. This lens had a slightly smaller extension length. The quality of silicon used for the lens fabrication is unknown. Silicon lenses with a bad quality and a low resistivity cause strong RF losses inside the lens and therefore a lower sensitivity of the mixer.

The IF gain bandwidth determined from the noise temperature measurement by measuring the gain and the noise of the IF amplifier chain seems to be much smaller (1.5-1.6 GHz) for NbTiN HEB devices than for NbN HEB devices. For the future it is very important to perform a IF gain bandwidth measurement up to 6 GHz IF to measure the IF gain bandwidth exactly. This makes it possible to compare NbTiN and NbN HEB devices more accurately.

Concerning the IF gain bandwidth NbN HEB devices seem to be superior to NbTiN HEB devices. NbN HEB mixers are to be used

for the HIFI instrument on the Herschel Space Observatory. The degradation of the mixer chips due to natural aging cause a great concern because the mixer unit will be stored for years before the launch. Ultrathin NbTiN have not been investigated for natural aging, but maybe NbTiN does not show such a strong natural aging process.

# Bibliography

[1] Graf U U, Heyminck S, Rabanus D, Jacobs K, Schieder R T, Stutzki J, "STAR: SOFIA terahertz array receiver", *Proceedings of the SPIE*, vol. 4857, pp. 97–104, 2003.

[2] Baselmans J J A, Hajenius M, Gao J R, Klapwijk T M, de Korte P A J, Voronov B, Gol'tsman G, "Doubling of sensitivity and bandwidth in phonon cooled hot electron bolometer mixers", *J. Appl. Phys.*, vol. 84, no. 11, pp. 1958–1961, March 2004.

[3] Langley S P, "The Bolometer", *Nature*, vol. 25, pp. 14–16, 1881.

[4] Boyle W S, Rogers K F, "Performance Characteristics of a new low-temperature bolometer", *J.Opt.Soc.Am.*, vol. 49, pp. 66–69, 1959.

[5] Lesurf L, *Millimetre-wave Optics, Devices and Systems*, Adam Hilger, New York (USA), 1990.

[6] Richards P L, "Bolometers for infrared and millimeter-wave", *J. Appl. Phys.*, vol. 76, pp. 1–24, 1994.

[7] Conwell E M, *High Field Transport in Semiconductors*, Academic Press, New York, June 1967.

[8] Luryi S, *Hot Electrons in Semiconductors: Physics and Devices*, chapter 17. Hot Electrons in Semiconductor, Clarendon Pr, February 1998.

[9] Semenov A D, Gol'tsman G N and Sobolewski R, "Hot-electron effect in superconductors and its applications for radiation sensors", *Supercond. Sci. Technol*, vol. 15, pp. R1–R16, 2002.

[10] Zmuidzinas J, *Progress in Coherent Detection Methods*, GCA-Verlag Herdecke, 1999.

[11] Caves C M, "Quantum limits on noise in linear amplifiers", *Phys.Rev. D*, vol. 26, no. 8, pp. 1817–1839, 1982.

[12] Prober D E, "Superconducting terahertz mixer using a transition-edge microbolometer", *Appl. Phys. Lett.*, vol. 62, pp. 2219–2121, April 1993.

[13] Gershenzon E M, Gol'sman G N, Gogidze I G, Gusev Y P, Elant'ev A I, Karasik B S and Semenov A D, "", *Phys. Chem. Technol.*, vol. 3, 1990.

[14] Skalare A, McGrath W R, Bumble B, LeDuc H G, "A heterodyne receiver at 533 GHz using a diffusion-cooled superconducting hot-electron bolometer mixer", *IEEE Trans. Appl. Supercond.*, vol. 5, pp. 2236–2239, 1995.

[15] Burke P J, Schoelkopf R J,Prober D E, Skalare A, McGrath W R, Bumble B and LeDuc H G, "Length scaling of bandwidth and noise in hot-electron superconducting mixers", *Appl. Phys. Lett.*, vol. 68, pp. 3343–3346, 1996.

[16] Stodolka J, Jacobs K, "Fabrication and receiver measurements of a diffusion-cooled hot-electron bolometer at 800 Ghz", in *12th Int'l. Symp. on Space Terahertz Technology*, 2001.

[17] Yngvesson K S, Musante C F, Ji M, Rodriguez F, Zhuang Y, Gerecht E, "A low-noise receiver user instrument for AST/RO at the south pole", in *12th Intern. Symp. Space THz Technology*, San Diego, 2001.

[18] Cherednichenko S, Yagoubov P, Il'in K, Gol'tsmann G N and Gershenzon E, "Large bandwidth of NbN phonon-cooled hot-electron bolometer mixers on sapphire substrates", in *8th Intern. Symp. Space THz Technology*, 1997.

[19] Cherednichenko S, Kroug M, Yagoubov P, Merkel H, Kollberg E, Yngvesson K S, Voronov B and Gol'tsman G, "IF Bandwidth of Phonon Cooled HEB Mixers made from NbN Films on MgO Substrates", in *11th Intern. Symp. Space THz Technology*, 2000, pp. 219–227.

140

[20] Tong C E, Kawamura J, Hunter T R, Papa C, Blundell R, Smith M, Patt F, Gol'tsman G N, Gershenzon E, "Successful operation of a 1 THz NbN Hot-Electron Bolometer receiver", in *11th Intern. Symp. Space THz Technology*, 2000.

[21] Karasik B S, Elantiev A I, "Noise temperature limit of a superconducting hot-electron bolometer mixer", *Appl. Phys. Lett.*, vol. 68, pp. 853–855, 1996.

[22] Karasik B S, Elantev A I, "Analysis of the noise performance of a hot-electron superconducting bolometer mixer", in *Proceedings of the 6th Int. Symp. on Space Terahertz Technology*, 1995.

[23] Skocpol W J, Beasley M R, Tinkham M, "Self-heating hotspots in superconducting thin-film microbridges", *J. Appl. Phys.*, vol. 45, no. 9, pp. 4054–4066, 1974.

[24] Floet D W, Miedema E, Klapwijk T M, Gao J R, "Hotspot mixing: A framework for heterodyne mixing in superconducting hot-electron bolometers", *Appl. Phys. Lett.*, vol. 74, no. 3, pp. 433–435, 1999.

[25] Chapman B, *Glow discharge Processes: Sputtering and plasma etching*, Wiley-Interscience, 1 edition, September 1980.

[26] Broussard Phillip R, *Superconducting Film Devices*, vol. 3 of *Handbook of Thin Film Devices*, Academic Press, 2000.

[27] Kadlec S, Musil J, Vyskocil H, "Hysteresis effect in reactive sputtering: a problem of system stability", *J. Phys. D: Appl. Phys.*, vol. 19, pp. 187–190, 1986.

[28] Schiller S, Beister G, Sieber W, "Reactive high rate d.c. sputtering: deposition rate, stoichiometry and features of $TiO_x$ and $TiN_x$ films with respect to the target mode", *Thin Solid Films*, vol. 111, pp. 259–268, 1984.

[29] Scholl R A, "Power Systems for Reactive Sputtering of Insulating Films", *Advanced Energy Industries Inc.*

[30] Koski K, Holsa J and Juliet P, "Voltage controlled reactive sputtering process for aluminium oxide films", *Thin Solid Films*, vol. 326, pp. 189–193, 1998.

[31] Golans A, *Thin-film Thermo-mechanical sensors embedded in metallic structures*, PhD thesis, Standford University, December 1999.

[32] Zinsmeister G, "Theory of thin film condensation.", *Thin Solid Films*, vol. 2, pp. 497–507, 1968.

[33] Lewis B, Anderson J C, *Nucleation and Growth of Thin Films*, Academic Press, 1978.

[34] Ratsch C, Venables J A, "Nucleation Theory and the Early Stages of Thin Film Growth", *Review article, to be published for the 50th anniversary of the American Vacuum Society*, 2003.

[35] Lewis K L, Muirhead I T, Pitt A M, Cullis A G, Williams, G M, Wyatt-Davies T J, "Thin-Film Deposition in Ultra-Clean Environments", *J. Vac. Sci. Technol. A*, vol. 7, no. 3, 1989.

[36] Mattox D M, *Handbook of physical vapor deposition (PVD) processing*, Noyes Publications, New Jersey, USA, 1998.

[37] Futamoto M, Honds Y, Kakibayashi Y, Shimotsu T, Uesaka Y, "Microstructure of CoCr Thin Films Prepared by Sputtering", *Jpn. J. Appl. Phys*, vol. 24, 1985.

[38] Iosad N N, Jackson B, Klapwijk T M, Polyakov S N, Dmitirev P N, Gao J R, "Optimization of RF- and DC-sputtered NbTiN films for integration with Nb-based SIS junctions", *IEEE Trans. Appl. Supercond.*, vol. 9, no. 2, pp. 1716–1719, June 1999.

[39] Yagoubov P, Gol'tsman G N, Voronov B, Seidman L, Siomash V, Cherednichenko S and Gershenzon E, "The bandwidth of HEB Mixers employing ultrathin NbN films on sapphire substrate", in *7th Intern. Symp. Space THz Technology*, 1996.

[40] Xiao J Q, Chien C L, "Proximity Effects in Superconductor/Insulating-Ferromagnet NbN/GdN Multilayers", *Phys. Rev. Lett.*, vol. 76, no. 10, 1996.

[41] Yu L, Newman N, Rowell J M, "Measurement of the Coherence Length of Sputtered $Nb_{0.62}Ti_{0.38}N$ Thin Films", *IEEE Trans. Appl. Supercond.*, vol. 12, no. 2, pp. 1795–1978, 2002.

[42] Stern J A, Bumble B, "Fabrication and DC-characterization of NbTiN based SIS Mixers for use between 600 and 1200 GHz", in *10th Intern. Symp. Space THz Technology*, 1998, pp. 305–313.

[43] Kroug M, Cherednichenko S, Merkel H, Kollberg E, Voronov B, Gol'tsman G N, Huebers H W and Richter H, "NbN Hot Electron Bolometric Mixers for Terahertz Receivers", *IEEE Trans. Appl. Superconductivity*, vol. 11, 2001.

[44] Brandt M, *Superconducting Hot Electron Bolometers on Silicon Nitride Membrandes for Terahertz Waveguide Mixers*, PhD thesis, Universität zu Köln, 2004.

[45] van der Pauw L J, "A method of measuring the resistivty and hall coefficient on lamellae of arbitrary shape", *Philips Technical Review*, vol. 26, no. 8, pp. 220–224, 1958.

[46] Westra K L, Brett M J, Vaneldik J F, "Properties of reactively sputtered NbN films", *J.Vac.Sci.Technol. A*, vol. 8, no. 3, pp. 1288–1293, 1990.

[47] Alessandrini E I, Sadagopan V, Laibowitz R B, "Relationship between Structure and Sputtering Parameters in NbN Films", *J.Vac.Sci.Technol.*, vol. 8, no. 1, pp. 188–191, January 1971.

[48] GE Advanced Materials, "Boralectric PBN Heaters", http://www.advceramics.com/.

[49] Bhushan M, "Analysis of reactive sputering mechanisms for NbN film depostion", *J.Vac.Sci.Technol. A*, vol. 5, pp. 2829–2835, 1987.

[50] Higashi G S, Chabal Y J, *Handbook of Semiconductor Wafer Cleaning Technology*, Noyes Publications, New Jersey, 1993.

[51] Glenz S H, *Fabrication and Characterization of Nb-Al/$Al_2O_3$-Nb Superconductor-Insulator-Superconductor Devices with NbTiN Based Tuning Circuits for the HIFI Instrument on the Herschel Space Observatory*, PhD thesis, Universität zu Köln, 2004.

[52] Matsunaga T, Maezawa H, Noguchi T, "Characterization of NbTiN Thin Films Prepared by Reactive DC-Magnetron Sputtering", *IEEE Trans. Appl. Supercond.*, vol. 13, no. 2, pp. 3284–3287, June 2003.

[53] Iosad N N, Mijiritskii A V, Roddatis V V, van der Pers N M, Jackson D B, Gao J R, Polyakov S N, Dmitriev P N, Klapwijk T M, "Properties of $(Nb_{0.35}, Ti_{0.15})_x Ni_{1-x}$ thin films deposited on silicon wafers at ambient substrate temperature", *J. Appl. Phys.*, vol. 88, no. 10, pp. 5756–5759, 2000.

[54] Myoren H, Shimizu T, Iizuka T, Takada S, "Properties of NbTiN Thin Films Prepared by Reactive DC Magnetron Sputtering", *IEEE Trans. Appl. Supercond.*, vol. 11, no. 1, pp. 3828–3831, 2001.

[55] Kerber G L, Cooper J E, Morris R S, Spargo J W, Toth AG, "NbN/MgO/NbN Josephson tunnel junctions fabricated on thin underlayers of MgO", *IEEE Trans. on Magnet.*, vol. 25, no. 2, 1989.

[56] Finkel M, Vachtomin Y, Antipov S, Drakinski V, Kaurova N, Voronov B, Gol'tsman G, "Gain bandwidth and noise temperature of NbTiN HEB mixer", in *Proceedings of 14th International Symposium on Space Treahertz Technology*, University of Arizona, Tuscon, USA, 2003, pp. 276–285.

[57] Tong C E, Stern J, Megerian K., Leduc H, Sridharan T K, Blundell R G, "A Low-noise NbTiN Hot Electron Bolometer Mixer", in *12th International Symposium on Space Terahertz Technology*, Dec. 2001, pp. 253–261.

[58] Scherer T A, Schicke M, Blundell R, Schuster K F, "Investigation of ultra-thin NbN films for phonon-cooled Hot-Electron Boloemters (HEB)", in *15th International Symposium on Space Treahertz Technology, in press*, Chalmers University, Göteborg, Sweden, 2005.

[59] Microchemicals GmbH, 89077 Ulm, *Lithographie Prozess ... und wie man sie reproduzierbarer machen kann*, AZ Electronics Materials (Deutschland) GmbH, 2005.

[60] Howard R E, Hu E L, Jackel L D, "Multilevel resist for lithography below 100nm", *IEEE Trans. Electron Dev.*, vol. 28, no. 11, 1981.

[61] Bedorf S, Munoz P, Tils T, Honingh C E, Jacobs K, "Development of Phonon-cooled NbTiN HEB Heterodyne Mixers for

GREAT", in *15th International Symposium on Space Treahertz Technology, in press*, Chalmers University, Göteborg, Sweden, 2005.

[62] Filipovic D F, Gearhardt S S, Rebeiz G M, "Double-Slot antennas on Extended Hemispherical and Elliptical Silicon Dielectric Lenses", *IEEE Trans. Microwave Theroy Tech.*, vol. 41, no. 10, pp. 1738–1749, 1993.

[63] Neikirk D P, Rutledge D B, Muha M S, Park H, Yu C X, "Progress in millimeter-wave integrated circuit imaging arrays", *Proc. Soc. Photo-Opt. Instr. Eng.*, vol. 317, 1981.

[64] Rebeiz G M, "Millimeter-Wave and Terahertz Integrated Circuit Antennas", in *Proceedings of the IEEE*, 1992, vol. 80 of *11*.

[65] Filipovic D F, Aliahmad W Y, Rebeiz G M, "Millimeter-wave double-dipole antennas for high gain integrated reflector illumination", *IEEE Trans. Microwave Theory Tech.*, vol. 40, no. 5, 1992.

[66] Lamb J W, "Miscellaneous Data on Materials for Millimetre and submillimetre Optics", *International Journal of Infrared and Millimeter Waves*, vol. 17, no. 12, pp. 1997–2034, 1996.

[67] Huebers H W, Schubert J, Krabbe A, Birk M, Wagner G, Semenov A, Gol'tsman G, Voronov B, Gershenzon E, "Parylene Anti-Reflection Coating of a Quasi-Optical Hot-Electron-Bolometric Mixer at Terahertz Frquencies", *Infrared Physics and Technology*, July 2000.

[68] Advanced Coating, 10723 Edison Court, Rancho Cucamonga, CA 91730, "Refractive index of Parylene C", personal comunication, June 2004.

[69] Ji M, Musante C, Yngvesson S, Gatesman A J, Waldmann J, "Study of parylene as anti-reflection coating for silicon optics at THz frequencies", in *11th Intern. Symp. Space THz Technology*, 2000.

[70] DiMer Beschichtungen, Robert-Bosch-Str. 6, 72654 Neckartenzlingen, "Deutschland".

[71] Dyson J D, "The equiangular spiral antenna", *IRE Trans. Antennas Propagat.*, vol. AP-7, pp. 181–187, 1959.

[72] Khosropanah P, *NbN and NbTiN Hot Electron Bolometer THz Mixers*, PhD Thesis, Chalmers University of Technology, Göteborg, Sweden, 2003.

[73] Grossman E N, Sauvageau J E, McDonald D G, "Lithographic sprial antennas at short wavelengths", *Appl. Phys. Lett.*, vol. 59, no. 25, pp. 3225–3227, 191.

[74] Hübers H W, Semenov A, Richter H, Birk M, Krocka M, Mair U, Smirnov K, Gol'tsman G, Voronov B, "Terahertz Heterodyne Receiver with a Hot-Electron Bolometer mixer", in *Proceedings of the Far-IR, Sub-MM, and MM detector Technology Workshop*, J. Wold and J.Davidson, Ed., 2002.

[75] Filipovic D F, Gauthier G P, Raman S, Rebeiz G M, "Off-Axis Properties of Silicon and Quartz Dielectric Lens Antennas", *IEEE Trans. Antennas Propagat.*, vol. 45, no. 5, pp. 760–766, 1997.

[76] Jackson B, *NbTiN-Based THz SIS Mixers for the Herschel Space Observatory*, PhD thesis, Technische Universiteit Delft, 2005.

[77] Karasik B S, Gaidis M C, McGrath W R, Bumble B, LeDuc H G, "Low noise in a diffusion-cooled hot-electron mixer at 2.5 THz", *Appl. Phys. Lett.*, vol. 71, no. 11, pp. 1567–1569, 1997.

[78] Hajenius M, Baselmans J J A, Gao J R, Klapwijk T M, de Korte P A J, Voronov B, Gol'tsman, "Low noise NbN superconducting hot electron bolometer mixers at 1.9 and 2.5 THz", *Supercond. Sci. Technol.*, vol. 17, pp. 224–228, 2004.

[79] Tinkham M, *Introduction to superconductivity*, McGraw Hill, second edition, 1996.

[80] Roshchin I V, Abeyta A C, Greene L H, Tanzer T A, Dorsten J F, Bohn P W, Han S W, Miceli P F, Klem J F, "Oberservation of the superconducting proximity effect in Nb/InAs and NbN$_{x}$/InAs by Raman scattering", *Phys. Rev. B*, vol. 66, no. 13, pp. 134530, 2002.

[81] Callen H B, Welton T A, "Irreversibility and Generalized Noise", *Phys. Rev.*, vol. 83, no. 1, pp. 34–40, July 1951.

[82] Zitex G 108, Saint-Gobain Performance Plastics, "http://www.labpure.com/nzitexmembranes.html", 2004.

[83] Benford D J, Gaidis M C, Kooi J W, "Optical Properties of Zitex in the Infrared to Submillimeter", *Apllied Optics*, vol. 42, no. 25, pp. 5118–5122, September 2003.

[84] Kroug M, Cherednichenko S, Choumas M, Merkel H, Kollberg E, Huebers H W, Richter H, Loudkov D, Voronov B, Gol'tsman G, "HEB Quasi-optical Heterodyne Receiver for THz Frequencies", in *Proceedings of the 12th Int. Symp. on Space Terahertz Technology*, 2001.

[85] Teipen R, *PhD Thesis in preparation*, PhD thesis, University of Cologne, I. Physikalisches Institut, 2005.

[86] Buettgenbach T H, "An Improved Solution for Integrated Array Optics in Quasi-Optical mm and Submm Receivers: the Hybrid Antenna", *IEEE Trans. Microwave Theroy Tech.*, vol. 41, no. 10, pp. 1750–1761, October 1993.

[87] Focardi P F, McGrath W R, Neto A, "Design Guidelines for Terahertz Mixers and Detectors", *IEEE Trans. Microwave Theroy Tech.*, vol. 53, no. 5, pp. 1653–1660, May 2005.

[88] Cherednichenko S, Kroug M, Merkel H, Khosropanah P, Adam A, Kollberg E, Loudkov D, Gol'tsman G, Voronov B, Richter H, Hübers H W, "1.6 THz heterodyne receiver for the far infraed space telescope", *Physica C*, , no. 372-376, pp. 427–431, 2002.

[89] Ekström H, Karasik B, Kollberg E, Yngvesson, "Conversion Gain and Noise of Niobium Superconducting Hot-Electron-Mixers", *IEEE Trans. Microwave Theroy Tech.*, vol. 43, no. 4, pp. 938–947, April 1995.

[90] Yagoubov P, Kroug M, Merkel H, Kollberg E, Gol'tsman G, Svechnikov S., Gershenon E, "Noise temperature and local oscillator power requirement of NbN phonon-cooled hot electron bolometric mixers at terahertz frequencies", *Appl. Phys. Lett.*, vol. 73, no. 19, pp. 2814–2816, November 1998.

147

[91] Baselmans J J A, Hajenius M, Gao J R, Baryshev A, Kooi J, Klapwijk T M, de Korte P A J, Voronov B, Gol'tsman G, "Hot Electron Bolometer mixers with improved interfaces: Sensitivity, LO power and Stability", in *Proceedings of the 15th Int. Symp. on Space Terahertz Technology*, 2004.

[92] Vachtomin Y B, Finkel M I, Antipov S V, Voronov B M, Smirnov K V, Kaurova N S, Drakinski V N, Gol'tsman G, "Gain bandwidth of phonon-cooled HEB mixer made of NbN thin film with MgO buffer layer on Si", in *Proceedings of the 13th International Symposium on Space Terahertz Technology*, Harvard University, Cambridge, Massachusetts, USA, 2002, pp. 259–270.

[93] Loudkov D, Khosropanah P, Cherednichenko S, Adam A, Merkel H, Kollberg E, Gol'tsman G, "Broadband Fourier Transform Spectrometer (FTS) measurements of spiral and double slot antennas at THz frequencies", in *Proceedings of teh 13th International Symposium on Space Terahertz Technology*, 2002.

[94] Khosropanah P, Bedorf S, Cherednichenko S, Drakinskiy V, Jacobs K, Merkel H and Kollberg E, "Fabrication and noise measurement of NbTiN hot electron bolometer heterodyne mixers at THz frequencies", in *Proceedings of 14th International Symposium on Space Treahertz Technology*, University of Arizona, Tuscon, USA, 2003, pp. 20–30.

# Appendix A

# Fabrication Recipe

## A.1 Fabrication Parameters for Phonon-Cooled HEBs

**Wafer Preparation**

1. Rinse wafer in $H_2O$ with ultrasound for 90s

2. Rinse wafer in acetone with ultrasound for 90s

3. Rinse wafer in isopropanol with ultrasound for 90s

4. Bake on hotplate at 120 °C for 3 min.

5. Rinse wafer in boiling isopropanol for 15 min.

**Ultrathin NbN/NbTiN Film Deposition**

**ultrathin NbN films**

1. Heating the substrate holder to 600°C in progressive stages of 200°C

2. Pre-Sputtering Nb cathode:

| Cathode: | Current: | Voltage | Pressure: | Flow: | Time: |
|----------|----------|---------|-----------|-------|-------|
| Nb | 0.34 A | 256 V | 0.502 Pa | 60 (Ar) | 1020 s. |
| Nb | 0.34 A | 281 V | 0.508 Pa | 60:1.7 (Ar:$N_2$) | 780 s |

3. Sputtering Nb cathode: (3-4 nm ultrathin NbN film)

| Cathode: | Current: | Voltage | Pressure: | Flow: | Time: |
|----------|----------|---------|-----------|-------|-------|
| Nb | 0.34 A | 282 V | 0.508 Pa | 60:1.7 (Ar:$N_2$) | 20 s |

**ultrathin NbTiN films**

1. Heating the substrate holder to 600°C in progressive stages of 200°C

2. Pre-Sputtering NbTi cathode:

| Cathode: | Current: | Voltage | Pressure: | Flow: | Time: |
|----------|----------|---------|-----------|-------|-------|
| NbTi | 1.01 A | 296 V | 0.625 Pa | 80 (Ar) | 600 s |
| NbTi | 1.01 A | 336 V | 0.632 Pa | 80:6 (Ar:$N_2$) | 540 s |

3. Sputtering NbTi cathode: (4 nm ultrathin NbTiN film)

| Cathode: | Current: | Voltage | Pressure: | Flow: | Time: |
|----------|----------|---------|-----------|-------|-------|
| NbTi | 1.01 A | 340 V | 0.632 Pa | 80:6 (Ar:$N_2$) | 6 s |

## Au Antenna Structure

1. Wafer cleaning with acetone and isopropanol

2. Spin coating AZ 5214

| Softbake | 45 s (90°C) |
|----------|-------------|
| Exposure | 17 s (6 mW/cm$^2$, UV-300) hard pressure contact |
| Reversal Bake | 90 s (120°C) |
| Flood Exposure | 90 s (6 mW/cm$^2$, UV-300) without mask |
| Develop | 60 s (AZ 726) |

3. Au antenna structure deposition

NbTi contact layer for Au (~ 2-3 nm)

| Cathode: | Current: | Voltage | Pressure: | Flow: | Time: |
|----------|----------|---------|-----------|-------|-------|
| NbTi | 0.95 A | 305 V | 0.644 Pa | 80 (Ar) | 480 s |
| NbTi | 0.95 A | 310 V | 0.641 Pa | 80 (Ar) | 4 s |

Au layer (200 nm)

| Cathode: | Current: | Voltage | Pressure: | Flow: | Time: |
|----------|----------|---------|-----------|-------|-------|
| Au | 0.26 A | 405 V | 2.02 Pa | 140 (Ar) | 90 s |
| Au | 0.26 A | 405 V | 2.02 Pa | 140 (Ar) | 160 s |

4. Lift-off: Boiling acetone (30 s) - Ultrasonic (30 s) - Boiling acetone (45 s)

## Contact Pads Definition by EBL

1. Copolymer (10% Ethyllaktat), 90 s 3000 rpm, 300 s bake 130°C

2. PMMA (2% Anisol), 90 s 3000 rpm, 300s bake 130°C

3. Al layer deposition

   | Cathode: | Power | Pressure: | Flow: | Time: |
   |----------|-------|-----------|----------|-------|
   | Al | 81 W | 3.02 Pa | 100 (Ar) | 300 s |
   | Al | 81 W | 3.02 Pa | 100 (Ar) | 23 s |

4. EBL lithography

5. Development

   | Al Dissolver (1:3) | 60 s |
   |--------------------|------|
   | $H_2O$ | 20 s. + rinse |
   | PMMA Developer | 80 s |
   | PMMA Stopper | 20 s |
   | rinse with $H_2O$ | |

6. Cleaning of the Interface Area

   | Gas: | Flow: | Pressure: | Power: | Time: |
   |------|-------|-----------|-----------|-------|
   | $O_2$ | 10 sccm | 10 Pa | 3 W (143 V) | 6 s |
   | Ar | 20 sccm | 3 Pa | 6 W (240 V) | 5 s |

7. Sputtering of NbTiN and Au

   | Cathode: | Power | Pressure: | Flow: | Time: |
   |----------|-------|-----------|----------------------|-------|
   | NbTi | 325 W | 0.75 Pa | 91 (Ar) | 300 s |
   | NbTi | 325 W | 0.74 Pa | 91+8 (Ar:$N_2$) | 300 s |
   | NbTi | 325 W | 0.78 Pa | 91+8 (Ar:$N_2$) | 17 s |
   | Au | 80 W | 3.5 Pa | 250 (Ar) | 60 s |
   | Au | 80 W | 3.5 Pa | 250 (Ar) | 26 s |

8. Lift-off with boiling acetone

151

## Microbridge Definition by EBL

1. ma-N2403, 40 s 4000 rpm, 60 s bake 90°C

2. EBL lithography

3. Development

   | | |
   |---|---|
   | Al Dissolver (1:3) | 60 s |
   | $H_2O$ | 20 s. + rinse |
   | AZ 726 Developer | 60 s |
   | $H_2O$ | 20 s |
   | rinse with $H_2O$ | |

## RIE-NbN/NbTiN removal

1. ICP System

   | | |
   |---|---|
   | Gas | $SF_6$ + Ar |
   | Pressure | 100 μbar |
   | Flow | 8 sccm |
   | Time | 1 min. |

2. Rinse water

# Danksagung

An erster Stelle möchte ich Herrn Professor Dr. Jürgen Stutzki danken, der mir die Gelegenheit gab, diese Arbeit am I. Physikalischen Institut der Universität zu Köln durchzuführen.

Herr Professor Dr. Peter Reiter erklärte sich freundlicherweise bereit, das Zweitgutachten zu erstellen. Außerdem bedanke ich mich bei Herrn Professor Dr. Michael Kerschgens für die Übernahme des Prüfungsvorsitzes.

Dr. Karl Jacobs danke ich für seine Hilfe und seine vielen technischen Hinweise, die erheblich beim Zustandekommen der "ultrathin films" geholfen haben. Ferner danke ich ihm für die Unterstützung bei der Endfassung und Korrektur dieser Arbeit.

Weiterer Dank geht an:

Dr. Netty Honingh für die Geduld und die Bereitschaft, meine Fragen wirklich jederzeit zu beantworten, sowie für manche Diskussion über Themen außerhalb der Physik,

Stephan Wulff für die tatkräftige Unterstützung bei der Behandlung einiger Vakuumanlagen sowie für das "Vorhalten des Spiegels" in allen Lebenslagen und die damit verbundenen Diskussionen über alle möglichen soziologischen und politischen Themen dieser Zeit,

Michael Schultz für die Unterstützung mit Autodesk Inventor und dafür, mir einige Eigenheiten eines Betriebsystems aus Redmond (für das man 3 Tasten mehr braucht) näher gebracht zu haben,

Thomas Tils für die Versorgung mit einigen seiner digitalen Sammlerstücke und für eine gute Rundenzeit bei der Rallye Göteborg-Köln,

Gundolf Schmidt für die Bereitstellung einer monochromatischen THz-Quelle in 301 und die Herausarbeitung persönlicher Stärken bei Selbstdarstellungen,

Frank Schlöder für die LaTex-Unterstützung sowie für die Korrektur einiger (fast aller) Konfigurationsscripte auf den zentralen Servern des Instituts und für die gemeinsamen Nebenschauplätze zur drahtlosen Informationsübertragung,

Rafael Teipen für die Begeisterungsfähigkeit für bestimmte Nahrungsmittel der Fast-Food-Industrie und die Verbreitung von WLAN- und VoIP-Software

sowie allen anderen Kollegen der SIS & HEB-Gruppe und allen Mitarbeitern des I. Physikalischen Instituts, die mich in meiner Zeit

hier begleitet haben.

Außerhalb des Instituts möchte ich mich besonders bei Sergrey Cherednichenko und Pourya Khosropanah bedanken, durch die ich die Möglichkeit hatte, gerade am Anfang meiner Arbeit, sehr viel Grundsätzliches im Bereich Hot-Electron-Bolometer zu lernen, und für die Möglichkeit, in Chalmers Heterodyne Messungen durchzuführen.

Ivan Camara Mayorga danke ich für die Bereitstellung der Antennen-Designs für 2.7 THz,

Thomas Koethe von der Konkurrenz für die Diskussionen, dass Physik doch alles sein kann, und für die Hilfe bei der Korrektur eines Teils dieser Arbeit.

Ganz besonderer Dank gilt natürlich meinem Vater, ohne dessen selbstlose Unterstützung dieses Studium nicht möglich gewesen wäre.

# Erklärung:

Ich versichere, dass ich die von mir vorgelegte Dissertation selbständig angefertigt, die benutzten Quellen und Hilfsmittel vollständig angegeben und die Stellen der Arbeit - einschließlich Tabellen, Karten und Abbildungen -, die anderen Werken im Wortlaut oder dem Sinn nach entnommen sind, in jedem Einzelfall als Entlehnung kenntlich gemacht habe; dass diese Dissertation noch keiner anderen Fakultät oder Universität zur Prüfung vorgelegen hat; dass sie - abgesehen von unten angegebenen Teilpublikationen - noch nicht veröffentlicht worden ist sowie, dass ich eine solche Veröffentlichung vor Abschluss des Promotionsverfahrens nicht vornehmen werde. Die Bestimmungen dieser Promotionsordnung sind mir bekannt. Die von mir vorgelegte Dissertation ist von Prof. Dr. Stutzki betreut worden.

Kön, 16. Dezember 2005

# Teilpublikationen:

Khosropanah P, Bedorf S, Cherednichenko S, Drakinskiy V, Jacobs K, Merkel H, Kollberg E, **Fabrication and Noise Measurement of NbTiN Hot Electron Bolometer Heterodyne Mixers at THz Frequencies**, Proc. 14th Int. Symp. on Space Terahertz Technology, pp. 22-24, April 2003, Tucson Arizona

Bedorf S, Muñoz P, Brandt M, Pütz P, Honingh C E, Jacobs K, **Development of phonon-cooled NbTiN HEB heterodyne mixers for THz applications**, 29th Int.Conf.IR & Millimeter Waves/IEEE 12th Int.Conf.on THz Electronics Proceedings, pp. 455-456, Karlsruhe 2004

Muñoz P, Bedorf S, Brandt M, Tils T, Honingh C E, Jacobs K, **Fabrication and characterization of phonon-cooled hot-electron bolometers on freestanding 2-$\mu$m silicon nitride membranes for THz applications**, In Stafford Withington, Jonas Zmuidzinas, Wayne S. Holland, editor, Proc. SPIE, Vol. 5498, pp. 509-516, SPIE, The International Society for Optical Engineering, 2004

Muñoz P, Bedorf S, Brandt M, Tils T, Honingh C E, Jacobs K, **Phonon-cooled hot electron bolometers on freestanding 2 $\mu$m Si$_3$N$_4$ membranes for THz applications**, Proc. of the 15th International Symposium on Space Terahertz Technology, Northampton Massachusetts, USA, April 27-29, 2004

Bedorf S, Muñoz P, Honingh C E, Jacobs K, **Development of phonon-cooled NbTiN HEB heterodyne mixers for GREAT**, Proc. of the 16th International Symposium on Space Terahertz Technology, Göteborg, Sweden, May, 2005